

Analysis of the Cardiovascular Control System
Using Broad-Band Stimulation

by

Ronald David Berger

Bachelor of Science
Electrical Engineering and Computer Science
Massachusetts Institute of Technology (1981)

Master of Science
Electrical Engineering and Computer Science
Massachusetts Institute of Technology (1983)

Submitted to the M.I.T. Department of
Electrical Engineering and Computer Science
in partial fulfillment of the requirements
for the degree of

Doctor of Philosophy

at the

Massachusetts Institute of Technology

June, 1987

Copyright (c) 1987 Ronald David Berger

The author hereby grants to M.I.T. permission to reproduce and to
distribute copies of this thesis document in whole or in part.

Signature of Author _____
Dept. of Electrical Engineering and Computer Science
June 10, 1987

Certified by _____
Richard J. Cohen
Thesis Supervisor

Accepted by _____
Chairman, Departmental Graduate Committee

MASSACHUSETTS INSTITUTE
OF TECHNOLOGY

MAR 22 1988

LIBRARIES

Analysis of the Cardiovascular Control System
Using Broad-Band Stimulation

by

Ronald David Berger

Submitted to the Department of Electrical Engineering
and Computer Science on June 10, 1987 in partial fulfillment
of the requirements for the Degree of Doctor of Philosophy

ABSTRACT

The research discussed in this thesis is an investigation of the regulatory mechanisms that govern the cardiovascular system. These mechanisms comprise the autonomic nervous system (ANS) and are modeled as part of a feedback network in which systemic arterial pressure is the controlled variable. In order to improve our understanding of the physiology and potential pathology of autonomic regulation, we have attempted to characterize the various functional and anatomic blocks implicated in cardiovascular control using transfer function analysis. Transfer functions represent the frequency response of the system or subsystem under study, and are derived from measurements of the system's input and output signals using spectral estimation techniques. Reliable estimation of the transfer function requires that the input signal contain significant power density over the entire frequency band of interest. Consequently, we have had to devise methods for the introduction of broad-band perturbations at various points in the cardiovascular system.

Our first set of experiments was designed for study of the response of the sino-atrial (SA) node to fluctuations in vagal and sympathetic tone, and was performed on anesthetized dogs. While the animal's atrial electrogram was continuously recorded, a train of current pulses was applied to the right vagus or cardiac stellate nerve. The frequency of these pulses was modulated by a band-limited Gaussian white noise signal whose mean level could be adjusted from one experimental run to the next. Transfer functions computed between the instantaneous neural stimulation frequency and the resulting heart rate show that the SA node responds to fluctuations in autonomic tone as a low-pass filter whose parameters vary as a function of the mean level of neural activity. This dependence on the operating point in the behavior of the SA node had not previously been appreciated.

In a second study, we developed a technique to allow investigation of the heart rate response to broad-band fluctuations in autonomic tone in human volunteer subjects. These fluctuations were elicited by having the subject breathe on cue to a sequence of beeps spaced erratically in time. Instantaneous lung volume and surface ECG were recorded and served as the system's input and output signals, respectively. Transfer functions were then computed for each subject in both supine and standing positions, and reveal a significant alteration in morphology associ-

ated with postural change. These results most likely reflect a shift in autonomic activity that accompanies postural change, and demonstrate the sensitivity of our approach in detecting subtle variations in autonomic balance.

A final set of experiments was designed, and a single pilot study performed on an anesthetized dog, to investigate the response of the ANS to fluctuations in blood pressure in terms of changes in heart rate and peripheral resistance. Broad-band oscillations in systemic arterial pressure were induced by electrically pacing the ventricles with a white noise frequency-modulated pulse train. The SA nodal rate response of the ANS was measured via epicardial atrial electrodes, and was decoupled from the ventricular activity by ablation of the atrioventricular junction (AVJ). Systemic vascular resistance was computed as the quotient between time-averaged arterial pressure and aortic flow signals. Transfer functions were then computed between arterial pressure and SA nodal rate and between pressure and vascular resistance. Results from the pilot study show that the determination of autonomic response characteristics using this approach is quite feasible. We intend to perform a series of experiments on dogs chronically instrumented as described, but using aseptic technique. Once recuperated from surgery, these dogs can then be studied in a fully conscious state, enabling us to explore the effects of interventions such as acute hemorrhage and selective autonomic blockade on cardiovascular regulation.

We believe these studies will improve our understanding of cardiovascular physiology and assist in our interpretation of spontaneous fluctuations commonly observed in the heart rate and arterial pressure. Furthermore, it is our hope that with additional research, our efforts will lead to the development of non-invasive clinical tools to assess the integrity of a patient's autonomic nervous system that will be applicable in a wide spectrum of pathologic conditions.

Thesis Supervisor: Prof. Richard J. Cohen

Title: Associate Professor,
Harvard - M.I.T. Division of Health Sciences and Technology

Acknowledgements

It is a pleasure to thank my thesis supervisor, Prof. Richard J. Cohen, for seven years of thoughtful guidance, advice, and friendship. I am particularly grateful for his encouragement and confidence in my abilities, especially at times when my own doubts might otherwise have led me away from a career in research. At the same time, he has continually challenged me to rethink and defend my ideas and techniques, thereby forcing me to strengthen my approach. Most importantly, however, he has developed a laboratory environment where I could freely explore my own research interests. I look forward to many years of further fruitful collaboration, and many more rousing sets of tennis.

I would like to thank my thesis readers, Professors Roger Mark and William Siebert, for their invaluable suggestions in the development and presentation of my thesis research. Prof. Mark was particularly helpful in critically reviewing the design of and data from my animal experiments. Prof. Siebert carefully examined my data analysis approach and offered many insightful recommendations regarding modeling techniques.

My alter ego, Joe Smith, has been a wonderful friend and a strong influence on my life during the last four years. His sharp wit and acerbic tongue have kept me always on my guard. The stimulating discussions we have had on both moral and scientific issues have added an important dimension to my graduate experience and sharpened my debating skills. Brainstorming together, Joe and I have found a synergism of thought that has led to many a wild scheme. Our friendship will surely continue to flourish as we enter our medical residency together.

Phil Saul has been a most valuable collaborator and friend. His enthusiasm and boundless energy were largely responsible for the success and completion of the respiratory arrhythmia studies, and his many clever suggestions were tremendously helpful in my experiments on the sino-atrial node. His ideas for future research have been the catalyst for many of my own, and I will enjoy continuing to work closely with him in the coming years.

I am very grateful for the contributions Paul Albrecht has made to my thesis work. He has helped me think through many of the signal processing issues involved in the data analysis, and he carefully reviewed the text of this thesis. Most importantly, however, Paul has provided our laboratory with an indispensable, though often taken for granted, array of software utilities of which I have made extensive use.

Bo Saxberg deserves my thanks for the many hours he spent teaching me the complex mathematics I needed to understand in order to prepare for my area exam. I appreciate the patience, selflessness, and clarity with which he explained to me this very difficult material. I wish him luck in choosing his post-graduate career path and congratulate him on his upcoming marriage.

I thank Mike Broide for the many hours of pleasurable conversation he has given me. Often sprinkled with tidbits of linguistics or physics

for the non-physicist, these discussions have provided rich food for thought. I particularly appreciate his explanation of why the sky is blue. I wish Mike luck as he approaches married life.

I owe much of my knowledge of animal experimentation techniques to the tutelage of Mike Bailin. Although we worked together for only a year, in that time, Mike managed to provide me with a solid foundation in anatomy, physiology, pharmacology, and pathology that seemed to encapsulate many of the important points I went on to learn in medical school.

I would like to take this opportunity to thank a number of other labmates for their help and friendship over the last several years. I only apologize for the brevity with which I recognize their contributions, and wish not to imply that their significance is any less than the aforementioned. I thank Robert Kenet for having introduced our lab, and me in particular, to transfer function analysis. I also appreciate all the laughs I had with Rob and his brother, Barney. Jeff Madwed's thorough investigation of Mayer waves sparked my interest in this area, and I thank him for his collaboration in performing the random-interval ventricular-pacing experiments with me. I thank Ming Hui Chen for her hard work and interest in carrying out and analyzing the respiratory arrhythmia experiments. Danny Kaplan has provided many interesting insights regarding both physics and politics, and I thank him for his careful proofreading of my thesis. I am grateful to Solange Akselrod for taking such good care of me for six weeks, while I worked in her lab at the University of Tel Aviv.

I would like to extend a special thanks to Keiko Oh, my "friend in high places." She has been extremely helpful in managing the administrative issues behind my research assistantships and fellowships, and has gone well beyond the call of duty in making my biggest headaches magically disappear.

The M.I.T. Division of Comparative Medicine is to be thanked for their excellent care of our laboratory animals. I am particularly indebted to Chris Newcomer and Terri Sylvina for their knowledge and assistance in handling animals.

At this point, I come to those for whom acknowledgement is most overdue. I would like to express my deep gratitude and love for my mother, Beverly, and father, Joseph, who have instilled in me a desire to learn and a drive to excel. Although they never pressured me academically, I fully attribute my achievements to the self-motivation and self-confidence that their upbringing fostered.

The last individual I wish to thank is the one to whom I dedicate this thesis, my wife, Linda. She has shared with me the successes and failures of my research, the fun and frustrations of my medical education, and the happiness and challenges of three years of marriage. Having uprooted herself from New York, she has made enormous sacrifices to make our marriage work. Always selflessly offering me her support, she has my love and my adoration.

Finally, I would like to thank the various agencies that provided financial support for this thesis research. These include NASA (grants NAG2-327 and NAGW-988), the Office of Naval Research (grant N00014-79-C-0168) and the Naval Blood Research Laboratory of the Boston University School of Medicine. I am grateful for fellowship support provided by the Whitaker Health Sciences Fund for my final year of graduate study.

To Linda with love.

Table of Contents

Abstract.....	2
Acknowledgements.....	4
Table of Contents.....	8
List of Figures.....	10
1. Introduction.....	12
2. Cardiovascular Physiology.....	16
2.1 Function of the cardiovascular system.....	16
2.2 Need for cardiovascular regulation.....	23
2.3 Autonomic control - a block model.....	26
2.4 Cardiovascular system responses.....	32
2.4.1 Physiologic influences.....	33
2.4.2 Pathologic states.....	36
3. Approaches toward studying autonomic regulation.....	42
3.1 System components and signals of interest.....	42
3.2 Mean levels of hemodynamic variables.....	44
3.3 Spontaneous hemodynamic fluctuations.....	45
3.4 Autoregressive models and techniques.....	48
3.5 Analyses using exogenous input excitation.....	57
3.6 Nonlinear analysis.....	60
3.7 Transfer function analysis.....	64
4. Signal processing techniques.....	69
4.1 Recording of physiologic signals.....	69
4.2 Sampling, filtering, and decimating.....	71
4.3 Derivation of the heart rate signal.....	76
4.3.1 Difficulties in defining heart rate.....	76
4.3.2 Previous algorithms for heart rate.....	76
4.3.3 Description of new heart rate algorithm.....	80
4.3.4 Performance comparison among algorithms.....	87
4.4 Spectral estimation.....	92
4.4.1 Autospectrum.....	92
4.4.2 Cross-spectrum.....	105
4.5 Transfer function estimation.....	107
4.5.1 Transfer and coherence functions.....	107
4.5.2 Confidence limits of transfer function.....	109
4.5.3 Pooling of transfer function data.....	112
5. Study of the response of the sino-atrial node.....	120
5.1 Introduction.....	120
5.2 Methods.....	122
5.3 Results.....	129
5.3.1 Vagal stimulation.....	129
5.3.2 Sympathetic stimulation.....	137
5.4 Discussion.....	146
5.4.1 Experimental response characteristics.....	146
5.4.2 Warner and Cox model of the sino-atrial node.....	149

5.5 Comments.....	153
6. Study of autonomic response to respiratory activity.....	157
6.1 Introduction.....	157
6.2 Methods.....	161
6.3 Results.....	170
6.4 Discussion.....	175
6.5 Follow-up studies.....	178
7. Animal model for analysis of autonomic response.....	181
7.1 Introduction.....	181
7.2 Methods.....	188
7.3 Results of pilot study.....	190
7.4 Discussion and proposal for conscious animal model.....	202
8. Conclusion.....	209
References.....	213
Biographical Sketch.....	225

List of Figures

2.1:	Schematic of the circulation.....	18
2.2:	Windkessel model of the circulation.....	20
2.3:	Waveforms resulting from Windkessel model.....	22
2.4:	Modified Windkessel model.....	24
2.5:	Block diagram of short-term CV control.....	27
2.6:	Example of Mayer waves.....	39
3.1:	Spontaneous fluctuations in HR and ABP.....	47
3.2:	Model of a linear system.....	48
4.1:	Digital anti-aliasing filter.....	74
4.2:	Explanation of tachometer algorithm.....	81
4.3:	Spectral window resulting from tachometer algorithm.....	84
4.4:	Comparison of HR spectra showing aliasing effects.....	86
4.5:	Comparison of four tachometer algorithms - I.....	88
4.6:	Comparison of four tachometer algorithms - II.....	90
4.7:	Gaussian window used in spectral estimation.....	101
4.8:	Flow chart of spectral estimation algorithm.....	104
4.9:	Measurement error in transfer function estimate.....	111
4.10:	Total error in transfer function estimate.....	115
4.11:	Flow chart of group-average transfer function estimation.....	118
5.1:	Apparatus used in experiments on the SA node.....	123
5.2:	Gaussian white noise frequency modulation.....	126
5.3:	Schematic of voltage-to-current converter circuit.....	127
5.4:	Mean SA nodal rate vs vagal stimulation frequency.....	130
5.5:	Example of signals during GWNFM vagal stimulation.....	131
5.6:	Example vagal rate-to-HR transfer and coherence functions.....	132
5.7:	Group-average vagal rate-to-HR transfer magnitude plots.....	134
5.8:	Group-average vagal rate-to-HR transfer phase plots.....	135
5.9:	Vagal rate-to-HR system gain plots.....	138
5.10:	Mean SA nodal rate vs sympathetic stimulation frequency.....	139
5.11:	Example of signals during GWNFM sympathetic stimulation.....	140
5.12:	Example symp. rate-to-HR transfer and coherence functions.....	142
5.13:	Group-average symp. rate-to-HR transfer function plots.....	143
5.14:	Sympathetic rate-to-HR system gain plots.....	145
5.15:	Reproduction of Warner and Cox model of SA nodal control.....	150
5.16:	Vagal rate-to-HR TF plots for Warner and Cox model.....	152
5.17:	Symp. rate-to-HR TF plots for Warner and Cox model.....	154
6.1:	Apparatus used in random-interval breathing experiments.....	162
6.2:	Distribution of inter-breath intervals.....	165
6.3:	Spectrum of impulses with interval distribution of Fig. 6.2... ..	169
6.4:	Example of signals during random-interval breathing.....	171
6.5:	Example of lung volume-to-HR TF and coherence.....	172
6.6:	Group-average lung volume-to-HR transfer function plots.....	173
7.1:	Model of baroreflex control of vascular resistance.....	185
7.2:	Multichannel recording from GWNFM pacing experiment.....	191
7.3:	6-minute record of derived signals during GWNFM pacing.....	193

7.4:	Power spectra of signals in Fig. 7.3.....	195
7.5:	Vent. rate-to-ABP TF and coherence - mean rate of 90 bpm.....	196
7.6:	Vent. rate-to-ABP TF and coherence - mean rate of 180 bpm.....	198
7.7:	ABP-to-atrial rate TF and coherence.....	199
7.8:	ABP-to-vascular resistance TF and coherence.....	200

Chapter 1: Introduction

The physiologic mechanisms that regulate the cardiovascular system have long intrigued investigators in a variety of disciplines. While medical researchers have quite naturally been interested in the performance of the cardiovascular control system as a critical determinant of patient health, engineers have found that this regulatory system constitutes a fascinating paradigm of nature's solution to a common engineering problem: feedback and control. If we attempt to model the cardiovascular control system as a feedback network, we need to identify (1) the central processor organ, (2) the variables that are being monitored and controlled, (3) the feedback paths and effector organs, (4) the set-points and operating regimes of the system, and (5) the transfer functions of the individual elements of the system and of the integrated system. Additional relevant points to consider regarding this system include interaction between the several feedback loops that comprise the network, stability of the overall system, nonlinearities of operation, and the appearance of failure modes.

A thorough understanding of this last point, namely the failure modes of the cardiovascular control system, is a large part of the motivation for the study of this system. Only with such an understanding can we fully appreciate the mechanisms that underlie the hemodynamic abnormalities seen in essential hypertension, sudden infant death syndrome, diabetes, and congestive heart failure, as well as in conditions that stress the cardiovascular system such as hemorrhagic shock. Furthermore, in order to provide proper therapeutic management in each of these pathological conditions, we must understand not only the etiology

and effects of the disease processes, but the effects of the interventions as well. In particular, many of the pharmacologic agents used in treating cardiovascular disorders selectively block one control path or another, leaving the rest of the system intact. Since the various control limbs that comprise this system have different characteristic time constants, selective blockade of any single pathway can affect the dynamics, and even the stability, of the system profoundly. Similarly, prosthetic devices such as pacemakers and artificial hearts can dramatically alter not only the set-point, but the dynamic response of the cardiovascular system to natural perturbations as well.

In the last century, great strides have been made toward understanding cardiovascular physiology. As I will discuss in greater detail later, a number of investigators have employed a systems engineering approach to study many aspects of the cardiovascular control system. A difficulty encountered in this area of research, as in the investigation of any biological system, is that one must significantly perturb the very system he wishes to study in order to obtain the most informative measurements. Conversely, the information obtainable from a study designed specifically to be minimally perturbing will inevitably be limited. Consequently, many questions remain unanswered regarding the dynamic response of the cardiovascular control system to disturbances of the nature that it normally experiences from one moment to the next.

In this thesis, I report on the application of broad-band stimulation techniques to probe the dynamics of several components of the cardiovascular control system. The data I present is derived from three different experimental setups: two groups of invasive studies in acute

anesthetized dog preparations and a non-invasive study in human volunteers. As mentioned above, the most invasive of these experiments provides the most easily interpreted measurements, while those in the least invasive studies were somewhat more perplexing. Nonetheless, significant, new, and interesting results were obtained in all studies, and add to our current understanding of cardiovascular regulatory dynamics. Furthermore, some of the techniques developed in the course of this thesis research show promise as potential diagnostic tools in clinical medicine.

To provide an appropriate perspective through which to view the experiments presented herein, I include a discussion (Chapter 2) of the relevant cardiovascular physiology and of a block-type model of the regulatory mechanisms that govern cardiovascular function. In Chapter 3, I review the various techniques to probe these control mechanisms that have been employed in the past, and discuss some of the results that have been obtained with these approaches. The data analysis techniques that I have utilized are presented in Chapter 4. Here, the signal processing algorithms, as well as the hardware and software developed for their implementation, are described. In Chapter 5, I discuss the animal preparation, results, and implications thereof for two sets of experiments performed on anesthetized dogs, designed to probe the dynamic behavior of the heart's normal pacemaker, the sino-atrial node. In Chapter 6, I present a study of the effects of respiratory activity on cardiovascular function in humans. A final group of experiments, designed to investigate neural regulation of heart rate and peripheral resistance, is discussed in Chapter 7. This latter study is part

of an ambitious on-going project, and the results presented are derived from pilot experiments performed on anesthetized dogs. Ultimately, these experiments will involve fully conscious animals who will have been previously instrumented with the necessary probes and catheters. Finally, in Chapter 8, the significant implications of all the studies are summarized, and future directions for this research are discussed.

Chapter 2: Cardiovascular Physiology

2.1 Function of the Cardiovascular System

The heart and blood vessels comprise a transport system that enables exchange of fluid, gases, electrolytes, nutrients, and waste products between the organs of the body. Of primary importance in the operation of this transport system is its ability to deliver sufficient oxygen to meet the collective metabolic needs of the various tissues. Nutrients such as carbohydrates and fats are transported between the digestive tract, liver, adipose tissue, and other organs for energy storage, and then back through the blood stream to the brain and musculature for energy utilization. Metabolic waste products including carbon dioxide and urea are carried by the cardiovascular system for elimination by the lungs and kidneys. The cardiovascular system also provides a route of transport for hormones produced by the endocrine system, and for the cells and products of the immune and clotting systems.

Fluid compartmentalization and osmolarity are maintained by the membranes of cells that line the vasculature. Since each cell's electrical and metabolic activities are strongly influenced by intra- and extracellular pH and electrolyte concentrations, the transport of these ions throughout the body constitutes a vital function of the cardiovascular system. Also, since the blood volume that fills the vasculature carries heat released as a byproduct of metabolism, the redistribution of the blood between parts of the body provides a mechanism for thermal regulation, as well. In particular, heat is conserved by selective constriction of vessels that serve the skin, and can be emitted through

perfusion of such peripheral tissue. When more rapid heat loss is required, as during muscular exercise, fluid originating in the vasculature is exuded through the skin via sweat glands, thereby allowing for evaporative cooling.

In its crudest form, the cardiovascular system may be thought of as a network of plumbing. The heart serves as a pump and the blood vessels are the pipes. The system is, in fact, more complicated than that: the heart is a dual pump with four chambers, and each half of the heart supplies a separate vascular circuit from the other. This structure is outlined in Figure 2.1. As shown in this schematic, blood returning from all organs except the lungs enters the right atrium, the antechamber of the right half of the heart. During the ventricular filling, or diastolic phase of the cardiac pumping cycle, the tricuspid valve opens, allowing blood to pass from the right atrium to the right ventricle. The blood is then ejected through the pulmonic valve to the pulmonary arterial vasculature during the systolic phase of the cardiac cycle. The pulmonary arteries arborize and perfuse the parenchyma of the lungs, where gas exchange between the alveolar sacs and the blood occurs. In particular, carbon dioxide is released from the blood and exhaled, while inspired oxygen diffuses into the blood. This oxygenated blood enters the left-side antechamber, the left atrium. Left atrial blood passes through the mitral valve into the left ventricle during diastole, and is then ejected through the aortic valve during systole. Branches of the aorta supply blood to the heart muscle itself, to the brain, kidneys, skeletal muscle, and skin, and to all other organs of the body.

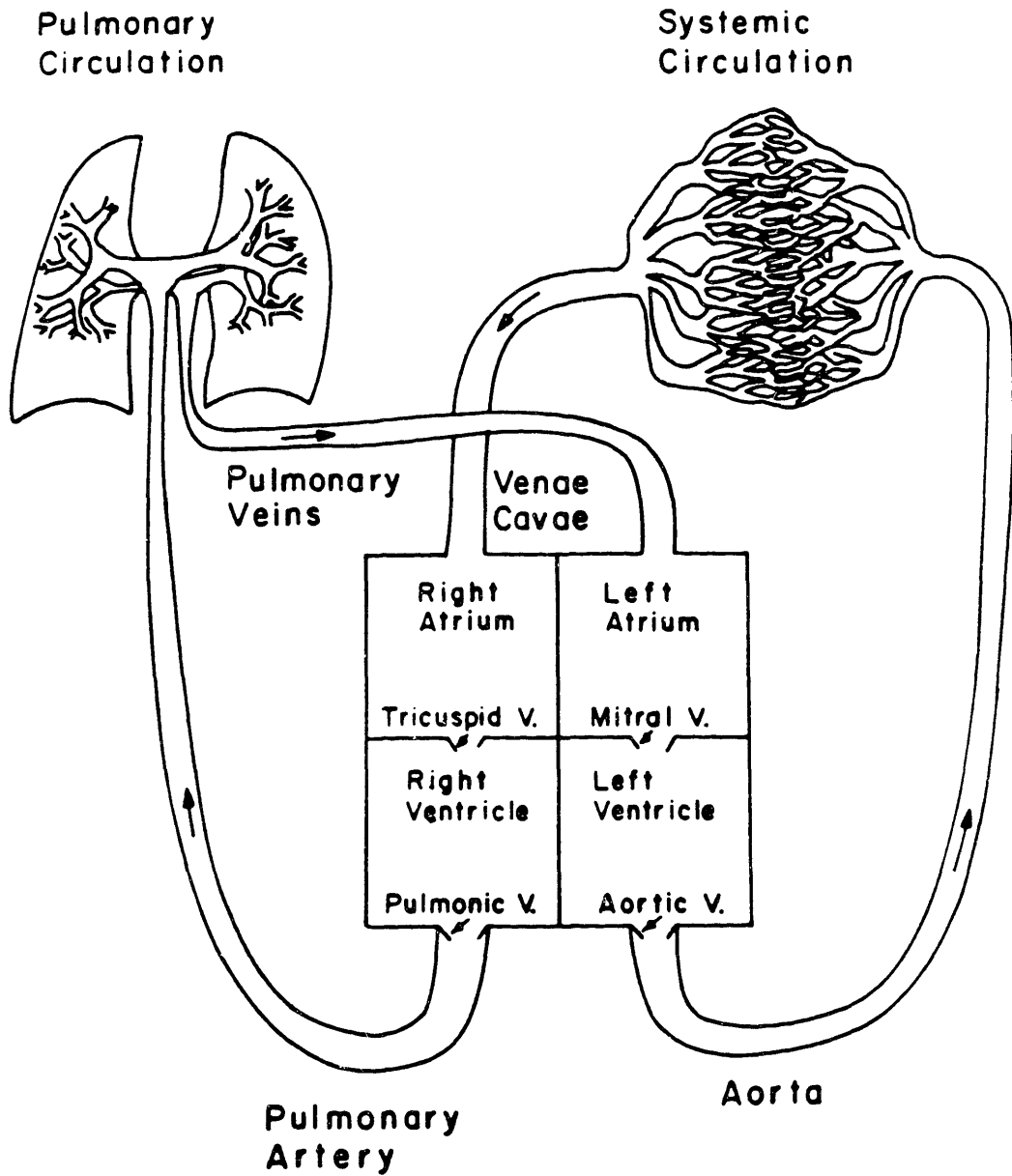


Figure 2.1. Schematic drawing of the circulation, showing the four chambers of the heart and the pulmonary and systemic vascular circuits.

The structure of the blood vessels themselves contributes importantly to the function of the cardiovascular system. Arteries, which carry blood at high pressure away from the heart, are muscular vessels capable of significant modulation of caliber and substantial stretching. They ramify into smaller and smaller arterioles, ultimately giving off capillaries whose walls are so thin as to allow gas exchange by diffusion. The capillaries merge into venules which in turn collect into larger and larger veins to return blood to the heart under low pressure. The venous system is composed of vessels with much thinner, less muscular, walls than in the arteries and arterioles. The veins thus possess a greater capacity for pooling of blood but present less resistance to flow than the arterial vessels.

The mechanical properties of the vasculature may thus be modeled by an electrical circuit with a resistance and capacitance as in Figure 2.2. In this representation, termed the Windkessel model, electric current is analogous to blood flow and voltage represents pressure. The heart is modeled here as a current source, although the cardiac output - and thus current level - are by no means assumed constant. A single current source, resistor, and capacitor, as here, model either the pulmonary or systemic circuit; two such networks may be coupled in series to represent the combined cardiovascular system. The resistance R is the net effective resistance of all the parallel branches of the vascular tree. Similarly, the capacitance C is the sum of the individual capacitances of the various vessels. This obviously represents a tremendous simplification of the true vasculature, where the resistance and capacitance are distributed along the length of the circuit, as in a

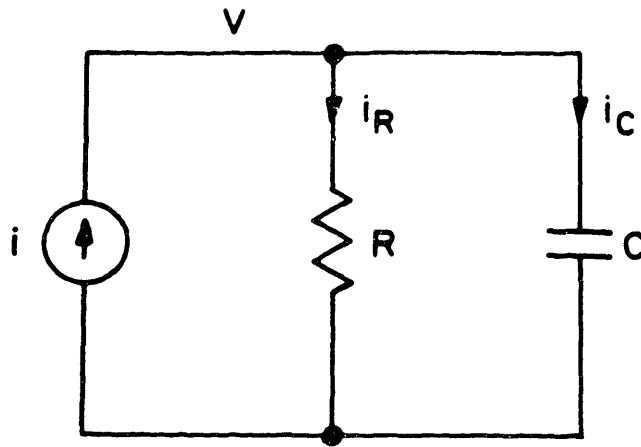


Figure 2.2. Windkessel model of the circulation.

waveguide.

The equations that describe the circuit behavior are:

$$i_C = C \frac{dV}{dt} \quad (2.1a)$$

$$i_R = \frac{V}{R} \quad (2.1b)$$

$$i_C + i_R = i \quad (2.1c)$$

Thus,

$$\frac{dV}{dt} + \frac{V}{RC} = \frac{i}{C}. \quad (2.2)$$

If the cardiac cycle is modeled by a square wave current signal of magnitude I_0 , then during systole,

$$V = V_a + I_0 R (1 - e^{-t/\tau}) \quad (2.3)$$

where V_a is the voltage just prior to the upstroke of the current wave, and the time constant τ equals RC . During diastole,

$$V = V_b e^{-t/\tau} \quad (2.4)$$

where V_b is the voltage just prior to the fall in supply current.

Examples of the current and corresponding voltage waveforms are shown in Figures 2.3a and 2.3b respectively. A stylized arterial pressure waveform is shown in Figure 2.3c for comparison with the circuit voltage signal. Note that the voltage waveform models the pressure quite well. In fact, much of the differences between these signals can be reconciled by taking into account the variable capacitance of the ventricle itself during systole and the rebound effect of valve closure at the termination of systole.

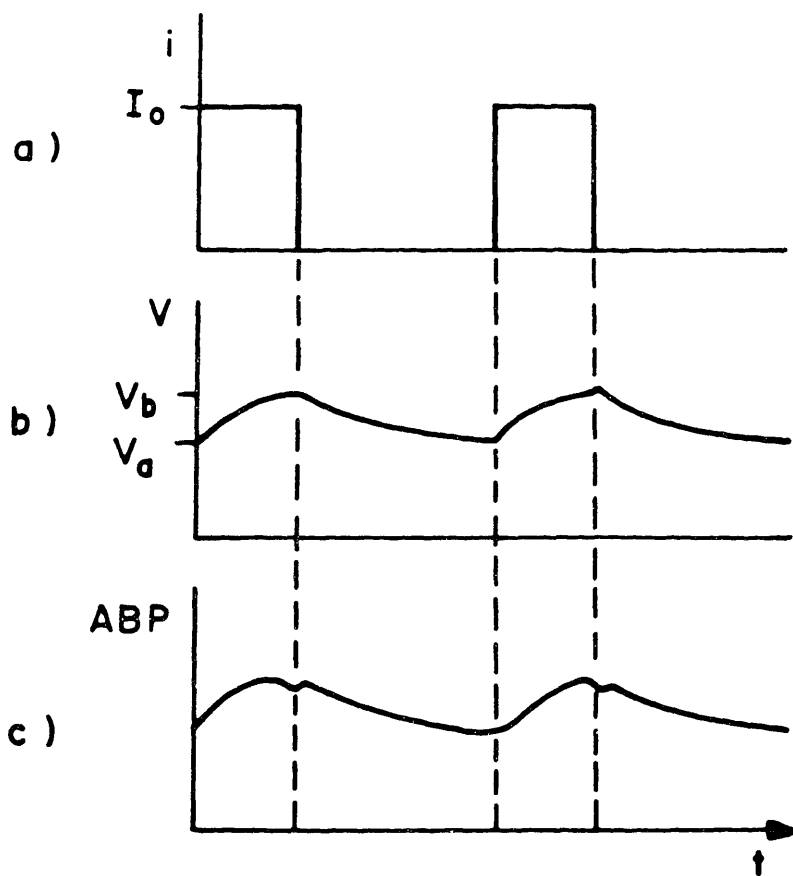


Figure 2.3. Current and voltage waveforms for the Windkessel model. When the square wave current signal (a) is applied to the model, the resulting voltage (b) rises and falls with time constant equal to RC . A stylized arterial blood pressure trace (c) is shown for comparison.

2.2 Need for Cardiovascular Regulation

The rate of metabolism in many tissues varies considerably depending on the rate of cellular growth, temperature, enzymatic activity, and work performed. If the blood flow to each organ were always sufficient to sustain its maximal metabolic needs regardless of the actual instantaneous requirements, the cardiac output would have to be maintained orders of magnitude greater than the normal resting level, placing inordinate demands on myocardial (heart muscle) performance. To avoid this state of affairs, the circulation functions parsimoniously; the blood flow to each organ of the body is maintained so as to exactly meet the instantaneous functional requirements of that tissue. This is accomplished through three basic mechanisms: 1) regulation of blood flow through the vasodilatory effects of insufficient nutrient concentration (e.g., oxygen) or of excess metabolites (e.g., carbon dioxide, lactic acid, hydrogen ions, etc.) within the local milieu, 2) neural control of cardiac output and vascular resistance, and 3) humoral (blood-borne chemical) regulation of either local or general vascular tone by substances such as hormones, ions, or toxins. These mechanisms allow for 25-fold increases in blood flow through tissues such as skeletal muscle, while at the same time preserve almost constant flow through the brain, whose functional requirements hardly vary.

The regulation of regional blood flow may be represented by a modified version of the circuit shown in Figure 2.2. The new circuit, shown in Figure 2.4, includes separate resistors for each section of the systemic circulation. Each of these resistors is composed of two components: one under local regulation via the first mechanism described

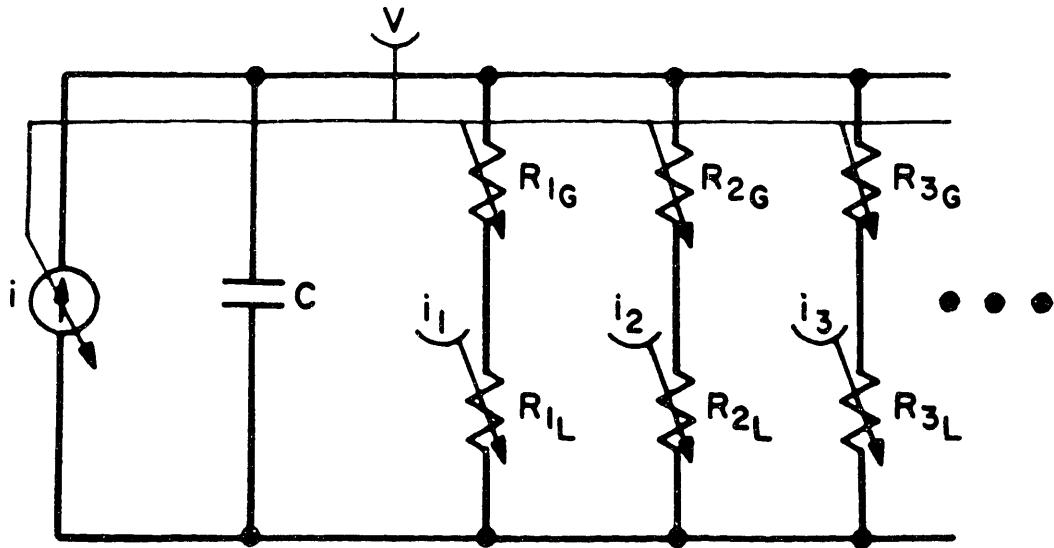


Figure 2.4. Modified Windkessel model, with separate resistors for each region of tissue in the body. Also indicated are local regulatory mechanisms that control a component of the resistance so as to maintain local perfusion, and global mechanisms that affect all the resistances and cardiac output so as to regulate arterial pressure.

above, and the other governed by the generalized effects included in mechanisms 2 and 3. Note that the current source is also regulated, representing the neural control of cardiac output.

A key question concerning the regulation of the circulation is: what governs central neural control of cardiac function and peripheral resistance? Local control mechanisms can respond to changes in dissolved ion and gas concentrations within the very neighborhood of the regulated blood vessels. But the central nervous system (CNS) can not sense regional changes throughout the body; rather, it responds to changes in global hemodynamic variables. As I will discuss in greater detail in Section 2.3, empirically, the CNS serves chiefly (although not exclusively) to regulate systemic arterial blood pressure. Referring to Figure 2.4, we see that a regulated arterial pressure, or voltage level V , enables local control mechanisms to adjust regional blood flow predictably and in proportion to the total local vascular resistance.

Cardiac output and systemic peripheral resistance are thus regulated as part of a feedback loop. The anatomic and functional elements that comprise this feedback loop will be discussed in the following section. The overall effect of these central control mechanisms can be summarized in terms of the circuit model: the current source and effective resistance are modulated to make the source behave as a well-regulated voltage supply. Superimposed on this regulated voltage or pressure level, however, appear phasic variations related to the cardiac cycle. The story is further complicated by the fact that the setpoint for mean arterial pressure may vary depending on the state of consciousness and activity level of the organism. In fact, the influence of

emotion, mentation, and other higher cerebral functions on hemodynamic control is an area of active research. It is a goal of this thesis work to explore the fundamental dynamics of the lower neural pathways implicated in cardiovascular regulation, as a foundation for investigatory endeavors concerning higher cortical pathways.

2.3 Autonomic Control - A Block Model

A block diagram model of the control network that regulates the cardiovascular system is shown in Figure 2.5. Each of the subsystems (blocks) within the complete network represents a distinct anatomical and functional component of the cardiovascular system, and the connecting lines represent either neural or vascular communication paths. Guyton et al [54] presented a similar but more complete model of the various cardiovascular control mechanisms. They separated these mechanisms into two categories: those that govern the hour-to-hour or even day-to-day state of fluid balance and those that mediate rapid responses (on the order of seconds to minutes) to perturbations in systemic blood pressure. The first category is comprised of the capillary filtration system which controls the distribution of fluid volume between the blood and the interstitial spaces, and renal mechanisms. These include the control of urine output through modulation of the glomerular filtration rate and the secretion of antidiuretic hormone and atrial natriuretic factor (ANF). The renin-angiotensin system (RAS), well reviewed recently by Reid [111], is considered by many to be another slowly reacting regulator of intravascular fluid volume, although Akselrod et al [4] have shown the RAS may play an important role in short-term hemo-

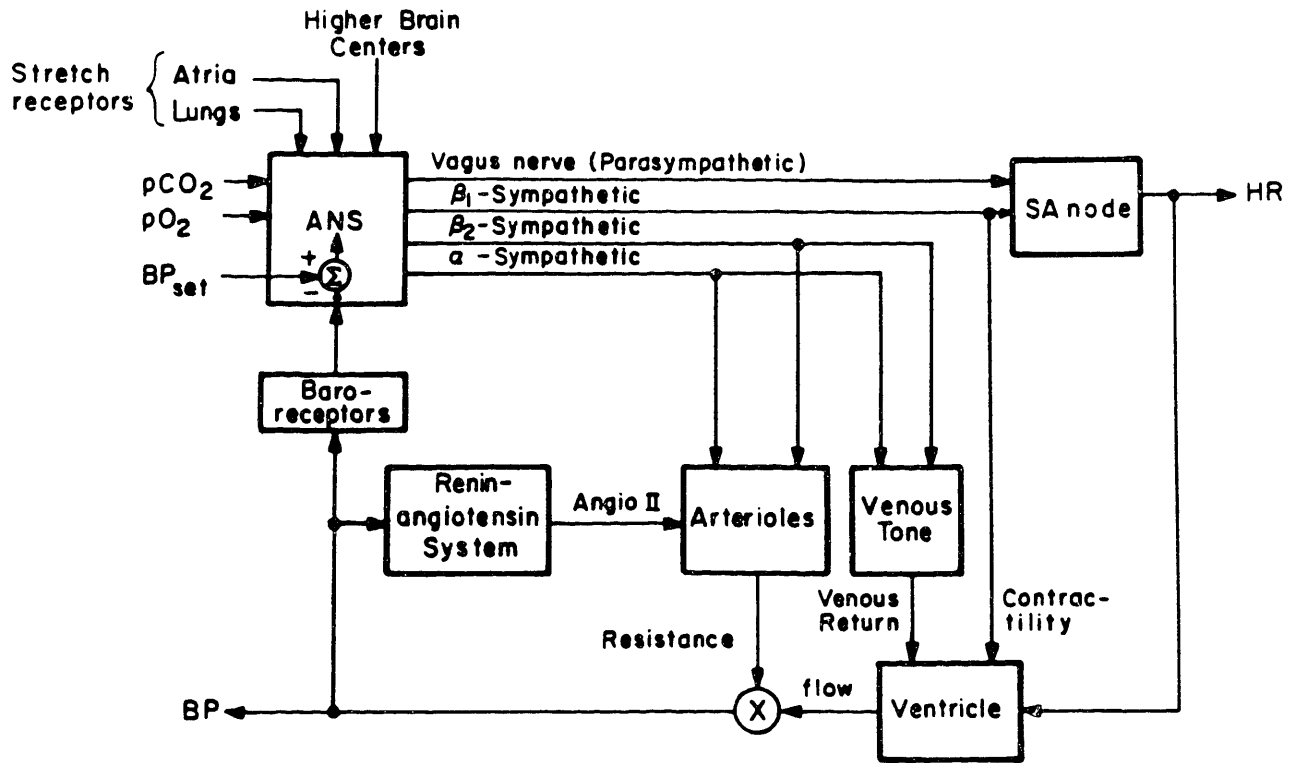


Figure 2.5. Block diagram of short-term cardiovascular control. Each block represents a separate functional entity, and the connecting lines denote paths of neural conduction or blood flow.

dynamic regulation, as well. The second category of cardiovascular control loops, however, consists of neurally mediated mechanisms, which by definition comprise the autonomic nervous system (ANS).

While the study of renal function and the effects of shifts in fluid balance on the cardiovascular system is an area of active investigation, the scope of this thesis is restricted to the mechanisms that regulate short-term control on hemodynamics (i.e., those with time constants less than 10 minutes). For this reason, I have omitted renal influences and capillary filtration in the model shown in Figure 2.5. (The renin-angiotensin system will not be considered further in this thesis, although it is included in this figure to show where its effects would enter the model.) For sure, there exist other physiologic mechanisms, not included in this model, whose response to hemodynamic perturbations may appear within minutes. The release of epinephrine from the adrenal medulla in situations of stress is one example, and there may well exist other similar mechanisms yet to be identified. Any such effector pathways will be considered in this model to be just sufficiently slow in their responses as to remain at constant levels of activity throughout any one ten minute period, although it is understood that these levels may differ from one operating regime to another. Since these influences may well be important or even dominate in certain physiologic regimes, one must obviously be cautious in attempting to extrapolate results whose significance assumes validity of this simplified model to situations in which the model does not well apply.

The autonomic nervous system receives numerous input signals both from afferent nerve fibers and from higher brain centers. The

information received from other parts of the brain includes many of the required set-point signals. One may alternatively define the autonomic nervous system to include any such brain centers, so that all set-points are controlled within the central processor block. The afferent nerves carry to the brainstem information regarding many physiologic variables. These include arterial blood gas partial pressures ($p\text{CO}_2$ and $p\text{O}_2$), body temperature, degree of lung expansion (chest wall stretch, actually), and blood pressure measured at several points in the vasculature. While all of these signals are undoubtedly of importance in some aspect of physiologic regulation, there is substantial evidence [58,100] suggesting systemic arterial blood pressure is the variable most carefully regulated by those feedback mechanisms that impinge on cardiovascular function. For simplicity in this model, arterial blood pressure will be the only variable considered to be both monitored and regulated by the cardiovascular control system. Hemodynamic variables such as heart rate and instantaneous cardiac output are, of course, governed by the ANS, but their modulation is assumed here to be a means for regulating the controlled variable, arterial pressure. Some other physiologic variables, such as body core temperature and $p\text{CO}_2$, are indeed both monitored and regulated by the ANS. An important assumption in this simplified model, however, is that these variables remain sufficiently static from moment to moment that their fluctuations do not significantly influence short-term cardiovascular control. (Note that $p\text{CO}_2$ is the key regulated variable in models of respiratory control [21], but does not substantially affect cardiovascular regulation unless its level rises or falls well above the normal range.)

The physiologic subsystem responsible for measuring arterial blood pressure is not simple. The transducers are several, located at different anatomical sites, and may respond somewhat differently from each other to fluctuations in pressure [5,39,66,67,121]. The most important of these transducers, or baroreceptors, are situated in the aortic arch and bilaterally in the bifurcations of the carotid arteries. The baroreceptors consist of stretch sensors within the walls of the vessels in which they are located. Afferent nerve fibers originating in the carotid baroreceptors communicate with the brainstem by way of the glossopharyngeal nerves, while aortic baroreceptor activity is carried by the left aortic nerve which runs to the brainstem within the vagosympathetic nerve trunk.

The autonomic nervous system apparently effects its function of cardiovascular control through multiple, seemingly redundant, pathways. Since mean arterial blood pressure is the product of cardiac output and arterial vascular resistance, it is not surprising that mechanisms exist to modulate both of these variables. Cardiac output is, in turn, the product of heart rate and stroke volume, each of which is also regulated by the autonomic nervous system. Further redundancy is present in the system in that two major efferent neural pathways exist for the communication of information from the brainstem to the cardiovascular effector organs. Signals carried along one of these neural networks, the sympathetic nervous system, generally effect an increase in arterial blood pressure and cardiac output, while the other pathway, the vagus nerve (a part of the parasympathetic nervous system) carries signals that mediate opposing effects. The sympathetic nervous system can be further subdivided

vided according to the particular chemical receptor on the cell surfaces of the tissues receiving the neural message. Although the neurotransmitter released by all sympathetic nerve terminals is norepinephrine, the receptor types differ somewhat in structure as well as in sensitivity to norepinephrine analogs, and are classified as α , β_1 , and β_2 . The neurotransmitter for the parasympathetic nervous system is acetyl choline, and the corresponding receptors on cells of the cardiovascular system's effector organs all appear to be of the same type, termed muscarinic receptors.

The effector organs of the cardiovascular control system are the sino-atrial (SA) node which functions as the heart's pacemaker, the cardiac ventricles whose contractility and degree of diastolic filling determine stroke volume, and the systemic vasculature which presents an impedance load to the ventricular pump. The SA node is innervated by both the vagus nerve and the sympathetic nervous system. The receptor type for the latter is β_1 . While either an increase in sympathetic activity or a decrease in vagal signals can initiate an increase in heart rate, the physiologic situations in which the first of these mechanisms is actually invoked may be quite different from those in which the second one predominates [37,52,108,122,125]. Thus the apparent redundancy of this dual innervation of the SA node may actually be an advantageous evolutionary development, allowing for the appropriate response to a transient fall in arterial blood pressure in a variety of settings. Similarly, the muscular walls of the arteriolar vessels, which are innervated by sympathetic fibers, possess receptors that elicit competing effects. α receptors predominate and when stimulated,

cause vasoconstriction and thus an increase in vascular resistance. However, β_2 receptors are also present in arterioles that supply skeletal muscle and mediate a vasodilatory response, especially during exercise. Diastolic filling depends most critically on the state of fluid balance, which varies slowly and is controlled predominantly by renal mechanisms, as described earlier, but can be modulated in the short term by changes in venous tone which is influenced by α and β_2 sympathetic activity [53]. Finally, the contractility of the ventricles appears to be controlled by the sympathetic nervous system (via β_1 receptors), although some evidence suggests a small degree of participation by the parasympathetic nervous system [100].

Clearly, the cardiovascular control system is substantially more complicated than a simple feedback and control system such as a furnace with a thermostat. The multiplicity of feedback and effector pathways may provide a system fail-safe against failure of an individual pathway, or it may be a crucial attribute of the system for optimal stable operation. This questions is largely unanswered at present.

2.4 General Cardiovascular System Behavior

Some of the basic principles of cardiovascular regulation are well illustrated by the system response to several common physiologic and pathologic perturbations. The availability of multiple feedback mechanisms, mentioned above, allows for the appearance of different types of response in different situations. Vagal, or parasympathetic, modulation is largely responsible for heart rate fluctuations in response to many physiologic influences, while the sympathetic nervous system mediates

most of the changes in cardiovascular function that take place in either physiologic or pathologic stress. Even when increased sympathetic drive is called upon, the specific reaction invoked may be quite selective; the diverse cardiovascular effects of generalized sympathetic discharge need not appear simultaneously.

2.4.1 Physiologic Influences

One of the most common physiologic perturbations to the circulation is a change in posture from a recumbent position to standing. The direct and immediate effect of such a postural change is a shift in local blood volumes and pressures due to the weight of the intravascular column of blood. Since the veins of the lower leg lie about 100 cm below the level of the heart in the average erect adult, the pressure in these veins should theoretically rise from less than 10 mm Hg when supine to over 80 mm Hg when standing. The actual elevation in leg venous pressure is not nearly this severe because valves within the veins interrupt the column of blood. Similarly, the hydrostatic pressure in the cerebral vasculature would be reduced by roughly 30 mm Hg on standing, were it not for compensatory mechanisms invoked.

Despite a modest rise in venous pressure in the lower extremities upon standing, the veins distend only minimally. Increased tone in sympathetic fibers innervating the veins stimulate α receptors in the vessel walls, thereby eliciting smooth muscle contraction and a reduction in venous capacity. α stimulation also causes an increase in systemic arterial resistance which helps to maintain arterial blood pressure in the cerebral circulation. Finally, the mean heart rate also

increases on transition from supine to erect position. This is, in part, a further manifestation of heightened sympathetic activity, as β_1 receptors in the SA node are stimulated. In most normal healthy individuals, however, most of the rise in heart rate on standing is due to withdrawal of vagal activity, as will be discussed in detail in Chapter 6. The elevated heart rate, coupled with reduced lower body venous capacity, helps mitigate the reduction in cardiac output that would otherwise occur if a substantial volume of blood pooled in the dependent vasculature. Note that all of these neurally mediated responses to standing are presumably triggered by the initial fall in arterial pressure at the level of the baroreceptors, although a decrease in right atrial stretch may also play an important role.

A physiologic stress requiring substantially greater adjustments in cardiovascular function is muscular exercise. During maximal exertion, the rate of total oxygen consumption can rise 15-fold over the basal state. This enormous demand for oxygen can be met in part by a 5-fold increase in cardiac output and thus oxygen delivery. Almost all of this amplification in cardiac output is accomplished by sympathetically mediated elevation in heart rate; the stroke volume rarely increases more than 50% above the basal level. The remainder of the excess oxygen demand is met by up to 3-fold increases in the fractional extraction of oxygen from the blood, which becomes manifest in a commensurately increased arteriovenous oxygen difference. The greatest part of the augmented cardiac output goes to the working skeletal muscle, which in fact steals blood from temporarily less essential organs, thereby reducing flow to those tissues. Organs that are exceptions to this rule

include the heart itself whose perfusion increases in proportion to the work it performs, the skin which is perfused according to heat loss requirements, and the brain whose blood flow is constant.

An important distinction between the effects of postural change and of exercise lies in the systemic vascular resistance. As mentioned above, on standing, arterioles throughout the body constrict to maintain cerebral blood pressure. During exercise, however, vessels that supply the working skeletal muscle dilate under the control of both local regulatory mechanisms and systemic β_1 sympathetic activation. As a result, systemic vascular resistance falls, often substantially. In this way, cardiac output can rise dramatically with only modest increases in arterial pressure.

A third physiologic perturbation of cardiovascular function is respiration. Both the pulmonary and systemic vascular circuits are influenced by the phasic intrathoracic pressure fluctuations that accompany the inspiratory/expiratory cycle. Not only does the intrathoracic pressure have an additive effect on the blood pressure in vessels emanating from the chest, but it also influences ventricular filling by enhancing venous return to the heart during inspiration and causing the opposite effect during expiration. Fluctuations in ventricular filling modulate cardiac output, which in turn perturbs arterial pressure.

A particularly interesting effect of respiration on the cardiovascular system, however, is its influence on heart rate. The phasic variations in heart rate that follow the inspiratory/expiratory cycle have long been recognized and are referred to as the respiratory sinus

arrhythmia (RSA). Three different mechanisms have been suggested as being at least partly responsible for this phenomenon. The first derives from the mechanical effects of respiration described above. The autonomic nervous system senses fluctuations in systemic arterial pressure (and perhaps in atrial stretch, as well) and responds through modulation of heart rate. A second potential mechanism is an autonomic response to the changing chest circumference. Stretch receptors within the chest wall may well exist and communicate with the brainstem. The third mechanism often cited is a direct neural interaction between the respiratory drive and heart rate control centers of the brainstem. The survival value of the latter two mechanisms is unclear and the RSA remains a confusing and actively investigated phenomenon.

The ANS mediates these respiratory-induced heart rate fluctuations predominately through modulation of vagal tone. Sympathetic modulation also contributes somewhat, however, particularly at lower frequencies of respiration. Since these two limbs of the ANS mediate responses with differing amounts of delay, the precise phase relationship between respiration and heart rate is likely frequency-dependent. Furthermore, influences that shift the sympathetic/parasympathetic balance, such as postural changes, will obviously affect this phase relationship, as well. These issues will be examined in detail in Chapter 6.

2.4.2 Pathologic States

The spectrum of disease states that alter autonomic regulation of cardiovascular function is almost as wide as the set of all diseases. Three types of pathologies are discussed here to illustrate the kinds of

failure modes that exist in the cardiovascular control system, and how the system tries to compensate for the effects of these maladies.

Hypertension, or high blood pressure, is a collection of disease states in which the operation of the feedback loop of Figure 2.5 has gone awry. This may occur as the result of three different etiologies. First, the natural pressure sensor, or baroreceptor, may malfunction, as in renal hypertension [100]. In this case, the ANS is no longer able to detect properly the effect of its own actions. In particular, if the baroreceptors send fewer impulses to the brainstem than they should for a given pressure level, then the ANS will elicit an increase in cardiac output or vascular resistance until the pressure rises such that the baroreceptor signals appear normal. At that point, of course, the arterial pressure is higher than desired.

Another scenario leading to hypertension is an inappropriate overactivity of the cardiovascular effector organs despite proper baroreceptor performance. This state of affairs implies that the ANS has lost the ability to effect a diminution in cardiac output or peripheral resistance. Vascular smooth muscle hyperactivity is one such condition where this loss of end-organ control occurs. Unregulated secretion of a sympathetic agonist into the blood stream, for example by an epinephrine producing pheochromocytoma, will similarly result in hypertension that is out of the hands of the ANS.

The vast majority of cases of hypertension, however, can not be linked to these aforementioned etiologies. The most likely explanation for these cases appears to be an idiopathic resetting of the central

setpoint for blood pressure control. Referring to Figure 2.5, this can be represented by an elevation in BP_{set} .

A second type of pathologic state where cardiovascular regulation is altered is hemorrhage. The autonomic responses to acute blood loss are in many ways similar to those mentioned for postural changes, but are generally of greater magnitude. Increased sympathetic discharge elicits venous and arteriolar constriction, thereby reducing venous capacitance and increasing vascular resistance. These effects, along with an elevated heart rate and force of ventricular contraction, serve to maintain mean arterial blood pressure even in the face of a 10% loss of the blood volume. In more extensive hemorrhage, adrenal secretion of epinephrine further augments sympathetic tone, and an accelerated respiration and widened arteriovenous oxygen difference help compensate for the reduced oxygen carrying capacity of the circulation.

However, a curious phenomenon is frequently observed in both humans and laboratory animals that have lost a significant fraction of the blood volume. Large amplitude low frequency (roughly .05 Hz) oscillations in heart rate and arterial blood pressure, as shown in Figure 2.6, often spontaneously appear. These 20-second rhythms have been termed Mayer waves [97], although their origin remains somewhat mysterious. The heart rate oscillations have been shown to be secondary to those in arterial pressure (presumably through the baroreflex) [95], and several theories have been proposed [106] to explain the pressure waves: 1) the triggering of a neural oscillator within the ANS, 2) the appearance of rhythmic smooth muscle contractions in arterial vessel walls, independent of the ANS, or 3) the development of a system resonance or

ARTERIAL BLOOD PRESSURE. HEART RATE AND RESPIRATION

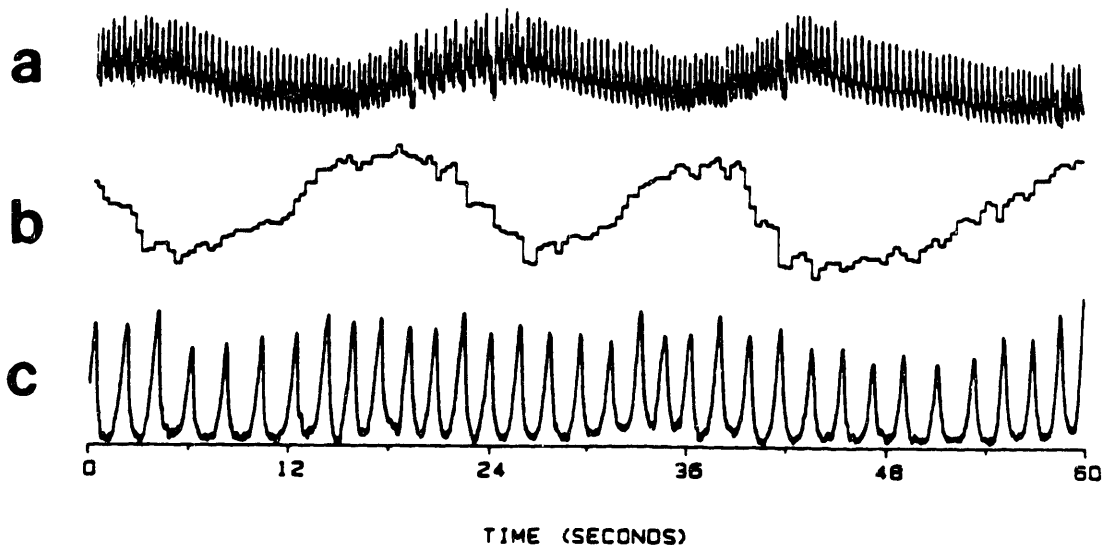


Figure 2.6. Example of Mayer waves in a conscious dog, elicited by 30 cc/kg hemorrhage. Note that oscillations in arterial blood pressure (a) and heart rate (b) have a period of roughly 20 seconds, which is much longer than the period of respiratory activity (c). Reproduced from Madwed, 1986.

instability due to some change in the operational parameters of the blood pressure control feedback loop. None of these tantalizing possibilities has yet been either well demonstrated or ruled out, despite active research in this area. One phase of this thesis research addresses these issues and is discussed in Chapter 7.

A final class of disease states that affect cardiovascular regulation, considered here, is the neuropathies. A neuropathic disorder could theoretically interfere with either afferent or efferent nerve conduction. The symptomatology associated with most neuropathies in which the ANS is involved, however, suggest sympathetic efferent nerve activity is most easily disrupted. The most common cardiovascular-related complaint in these disorders is postural hypotension leading to syncopal (fainting) attacks upon standing, reflecting a loss of the sympathetically mediated compensatory mechanisms normally invoked in postural changes.

Neuropathies are diseases that affect either the central nervous system or peripheral nerves. The first category includes spinal trauma and tabes dorsalis (tertiary syphilis) in which preganglionic sympathetic fibers are injured before they emerge from the spinal cord, pontine hemorrhage which disrupts the autonomic nuclei in the brainstem, and a rare degenerative disorder of unknown cause called idiopathic autonomic insufficiency or Shy-Drager syndrome. A prototypical peripheral neuropathy is that associated with diabetes mellitus. In this disease state, multiple peripheral sensory and motor nerves are often affected, leading to parasthesias and pareses. But the appearance of postural hypotension in affected individuals suggests sympathetic

efferents, presumably postganglionic, may be disrupted by this disease as well. The analysis techniques developed in this thesis research may have utility in the early noninvasive detection of neuropathy in many disease states. This is discussed further in Chapter 6.

Chapter 3: Approaches Toward Studying Autonomic Regulation

3.1 System Components and Signals of Interest

The control network that regulates the cardiovascular system may be studied as a whole or piece by piece. Both of these approaches have been employed in the numerous past investigations of this system. In taking the latter approach, one must decide how to split the control system into its component parts and then identify which components are to be studied. The splitting operation is somewhat arbitrary; for instance, it is artificial to consider the left ventricle functionally separate from the aorta and yet lump the aorta together with the rest of the systemic vasculature in our analysis. On the other hand, if this sort of division is done intelligently, we may be able to express the complicated behavior of the integrated system as the interaction of several more readily analyzed and understood functional blocks.

An important criterion in demarcating the functional blocks that comprise the control system is that the signals considered to pass from one block to the next be well defined. If these signals can be measured, then analysis of the behavior of the blocks becomes feasible. Furthermore, if the communication of these signals between blocks can be interrupted, then the behavior of the blocks may also be studied in an "open-loop" configuration of the control network. It is important, however, to reiterate the caution mentioned in Chapter 1: the procedure of opening the control loop may dramatically alter the operation of the very system we wish to study.

A traditional and convenient delineation of system components that

satisfies the above criterion is portrayed in Figure 2.5. Again, briefly, the cardiovascular control system is divided into a pacemaker (the sino-atrial node), a ventricle, resistance vessels, capacitance vessels, a pressure sensor (or baroreceptor), and a central control element (taken to be the combined nuclei of the brainstem). The relevant signals that pass between these functional blocks include the pacemaker rate, ventricular output or flow, vascular impedance, systemic arterial blood pressure, and the various neural signals sent from the baroreceptor to the central controller and from central controller to all effector organs.

Arterial pressure is readily measured in humans or animals with a strain gauge either inserted into or placed in fluid contact with an arterial lumen. Cardiac output can be obtained on an instant to instant basis with either electromagnetic or ultrasonic flow probes implanted around the aortic root, or on a time-averaged basis less invasively using either Fick or indicator-dilution methods [100]. The real part of the vascular impedance, namely the resistance, can be estimated for each cardiac cycle by dividing the mean pressure by the mean flow rate for that beat. The pacemaker rate or heart rate is derived from the electrocardiogram as the instantaneous frequency of cardiac activations. Since the activations occur at discrete points in time, there are some subtleties in defining the heart rate between these events. This is discussed in detail in section 4.3. Neural signals are, however, technically the most difficult to measure. In general, the nerves are accessible only through fairly invasive procedures, and even then carry a signal that is often difficult to discern from noise. The vast majority

of previous analyses of cardiovascular control, not surprisingly, have thus been based on the two most readily obtained system signals, heart rate and arterial blood pressure. A number of more invasive studies have also examined aortic flow and peripheral resistance, and a few have involved analyses of neural signals, particularly in the carotid sinus nerve.

3.2 Mean Levels of Hemodynamic Variables

Undoubtedly the simplest analysis of hemodynamic regulation is a determination of mean values for the system variables. A set of such values for heart rate, arterial pressure, and cardiac output remains the standard form for characterizing an individual's hemodynamic status in a critical care setting. Indeed, mean arterial pressure is likely the key indicator of vital organ perfusion, mean cardiac output is a good metric of cardiac function, and mean heart rate provides a measure of net sympathetic/parasympathetic balance. Furthermore, treatment regimens for essential hypertension are based almost entirely on steady state values of arterial pressure. (Actually, the most important measure for following antihypertensive therapy is the average diastolic pressure, which is not the same as the mean arterial pressure. Like mean pressure, however, the diastolic pressure measurement alone provides no information regarding the nature of fluctuations in blood pressure.)

The mean signal values, in effect, indicate the bias points at which the system components operate. Some additional understanding of the behavior of a few system elements is afforded by examining a component's output level when its input signal is experimentally clamped

at various constant values, after the control loop has been opened. For instance, in 1934, Rosenblueth and Simeone [117] applied constant frequency stimulation to the sympathetic and parasympathetic nerves and measured the change in heart rate. These workers, as well as others who conducted similar studies [92,119], presented input-output curves relating the change in heart rate to the stimulus frequency. Their data demonstrates how different levels of sympathetic or vagal tone influence the operating or bias point of the sino-atrial node, but does not address the issue of fluctuations in autonomic tone around the operating point or of the heart rate response to such fluctuations.

Similarly, a number of studies have been conducted to investigate the effects of mean arterial blood pressure on the operating point of the baroreceptor reflex [5,41,48,76]. In these studies, the arterial baroreceptors were isolated and perfused at various mean pressures while the heart rate and systemic arterial blood pressure were recorded. Although the importance of the pulsatile nature of blood pressure was addressed by several investigators [5,41,67,126,131] (and a pulsatile component was therefore added to the applied mean perfusion pressure), the critical issue of frequency-dependent responses to pressure fluctuations was ignored.

3.3 Spontaneous Hemodynamic Fluctuations

An analysis of spontaneous fluctuations in the signals generated by a control system often provides far more insight into the operation of the system than does knowledge of the signal means. This is well exemplified by the furnace-thermostat analogy. The mean temperature in a

house tells something about the thriftiness of the home owner with regard to his use of heating oil, but nothing about the ability of the heating system to respond to perturbations such as changes in outside air temperature. On the other hand, the frequency of the characteristic oscillations in temperature seen with such a heating system reflects the amount of delay and hysteresis, or memory, inherent in the system, as well as the periodicity of the perturbations (i.e., variations in external air temperature).

A number of studies have been conducted in which a description of autonomic nervous system function was deduced from observations of spontaneous fluctuations in hemodynamic variables in a variety of physiologic states [3,4,25,32-34,62,63,84,94,107,108,120,142]. Examples of such fluctuations in heart rate and arterial blood pressure are shown in Figures 3.1a and b. Since many of the arguments made by these investigators are based on frequency-domain representations of such signals, Figures 3.1c and d are included to show corresponding power spectra of the signals of parts a and b. Note that the estimation of these spectra from finite length time-domain records is a nontrivial problem and is discussed in Section 4.4.

The underlying assumption in any attempt to infer system component behavior from observations of spontaneous fluctuations is that knowledge of the output signal alone is adequate to deduce the input-output characteristics of a system. Analysis of such fluctuations affords some ability to compare the effects of different physiologic states on cardiovascular function, but in fact, it allows for only a crude description of a system transfer function in any one state. The greatest

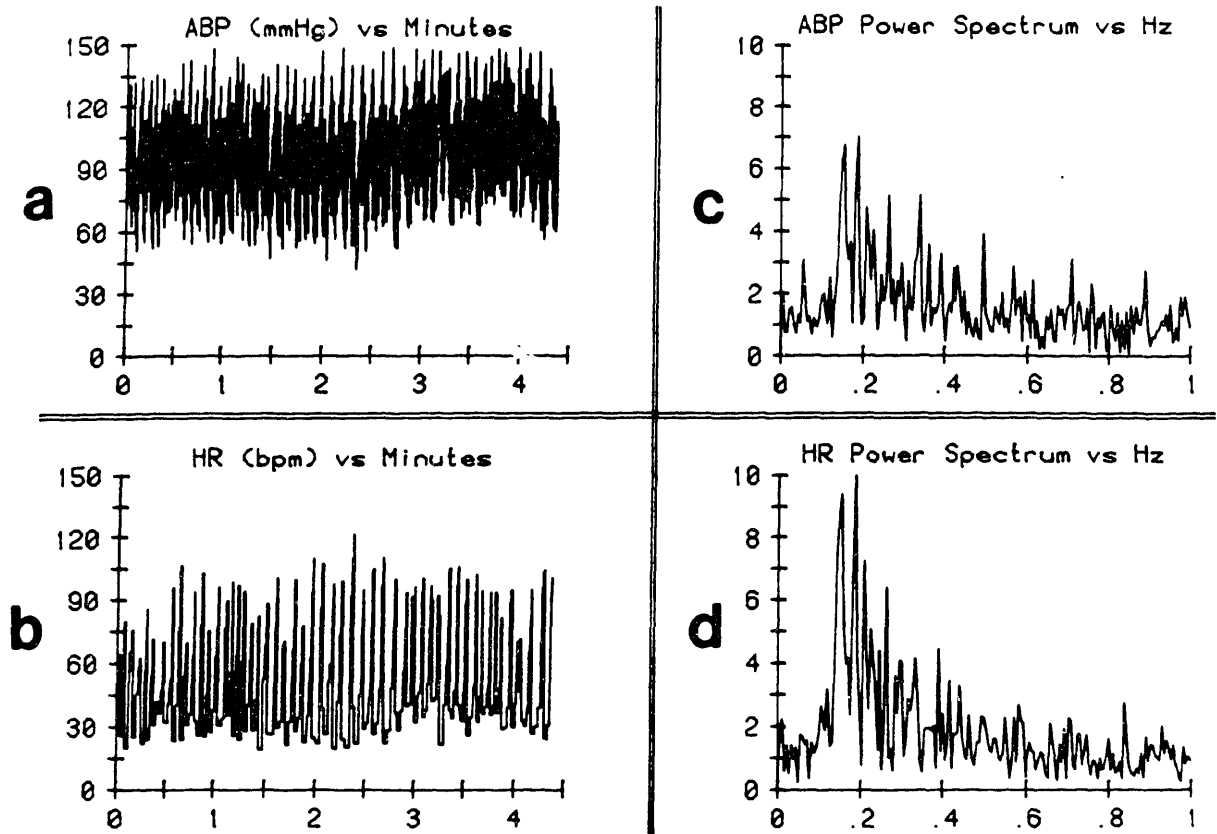


Figure 3.1. Time series of normal spontaneous fluctuations in blood pressure (a) and heart rate (b), and their corresponding power spectral density functions, (c) and (d) respectively. Reproduced from Madwed, 1986.

difficulty with this method is that one might interpret a lack of power density in a particular frequency band of the measured signal as a diminished system response in that band, when in fact it may result simply from the lack of any input excitation at those frequencies.

3.4 Autoregressive Models and Techniques

Despite the dangers associated with trying to interpret spontaneous hemodynamic fluctuations, a number of techniques have been developed to identify sensible models of cardiovascular function that could produce the observed signal waveforms. In general, these incorporate linear components assumed to be excited by an unmeasurable noise source. A simple example is the model of a system component as a filter excited by perfectly white noise (constant power density as a function of frequency), as shown in Figure 3.2.

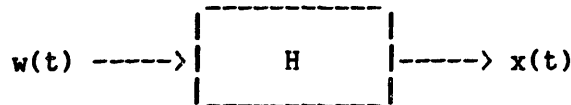


Figure 3.2. Linear system excited by noise.

The output power spectrum $P_{xx}(f)$ is then related to the noise spectrum $P_{ww}(f)$ by

$$P_{xx}(f) = |H(f)|^2 \cdot P_{ww}(f) = k|H(f)|^2 \quad (3.1)$$

where $H(f)$ is the transfer function of the modelled system component,

and k is the power density level of the noise $w(t)$. Thus,

$$|H(f)| = \left[\frac{1}{k} P_{xx}(f) \right]^{1/2} \quad (3.2)$$

suggesting that the transfer function magnitude may be determined to within a proportionality constant from knowledge of the output power spectrum alone. In this fashion, one could, for example, model the sino-atrial node as a filter stimulated by white noise, whose transfer characteristics are proportional to the square root of the heart rate power spectrum.

This technique poses two difficulties. The first relates to the aforementioned lack of knowledge about the actual system excitation that is assumed to be perfectly white. Even if the excitation were an ideal white noise source, any finite duration realization of such a signal would not contain exactly identical amounts of power in each bin of the power spectrum. (This is actually a problem in spectral estimation from finite duration records and will be discussed further in Section 4.4.) As a result of this phenomenon, it is fallacious to interpret hills and valleys in the transfer function magnitude as real, just because such features are present in the power spectrum of the output signal. Obviously, the problem becomes even worse if the theoretical noise spectrum is not white.

The other difficulty with this approach is that it provides no insight into the transfer phase characteristics of the system component under study. Phase behavior can be inferred only with better knowledge of the input signal or with the imposition of additional assumptions in formulating the model of the subsystem at hand.

A broad class of models that carry certain assumptions and provide for a description of phase characteristics are the autoregressive moving-average (ARMA) models. These relate the current level of a spontaneously varying signal to its past history and the current and past values of an excitatory noise source. By virtue of the nature of these models, the investigator may select, a priori, the level of complexity, or number of free parameters, of the chosen model. In its most general form, an ARMA process $x(t)$ (i.e., a signal produced by an ARMA model) is characterized by the differential equation,

$$\begin{aligned} \alpha_p \frac{d^p x(t)}{dt^p} + \alpha_{p-1} \frac{d^{p-1} x(t)}{dt^{p-1}} + \dots + \alpha_0 x(t) \\ = \beta_q \frac{d^q w(t)}{dt^q} + \beta_{q-1} \frac{d^{q-1} w(t)}{dt^{q-1}} + \dots + \beta_0 w(t) \end{aligned} \quad (3.3)$$

where $w(t)$ is the input noise*. Model identification involves finding values of $\alpha_0 \dots \alpha_p$ and $\beta_0 \dots \beta_q$ that best fit the observed $x(t)$ given an assumed form for $w(t)$. The choice of appropriate truncation levels p and q for the two sides of equation (3.3) determine the order and complexity of the model. Because these models are completely described by a finite (and generally small) set of constants, they are referred to as parametric models. By contrast, note that in the approach mentioned above, in which the transfer function is computed directly from the process power spectrum, the system description requires an entire curve or equivalently, a large set of parameters. Such models are thus termed

* Note that both $w(t)$ and $x(t)$ are assumed zero-mean in equation (3.3). If $x(t)$ is not a zero-mean process, such as heart rate or blood pressure, its mean value should be removed and the remaining fluctuations then analyzed as described.

infinite-parameter or, more commonly, non-parametric models.

Identification algorithms for ARMA models have been developed for implementation on digital computers, thus requiring digitization of observed signal $x(t)$. The i^{th} sample of $x(t)$ is denoted $x(i)$ and the differential equation above may be written in the linear difference equation form,

$$x(n) + \sum_{k=1}^p a(k)x(n-k) = \sum_{l=0}^q b(l)w(n-l). \quad (3.4)$$

Note that there is no need for an extra parameter $a(0)$ as a multiplier of $x(n)$, since it may be factored out of the equation without loss of generality. Taking the z-transform [102] of equation (3.4) yields

$$A(z)X(z) = B(z)W(z) \quad (3.5)$$

where

$$A(z) = 1 + \sum_{m=1}^p a(m)z^{-m} \quad (3.6a)$$

and

$$B(z) = \sum_{m=0}^q b(m)z^{-m}. \quad (3.6b)$$

The system function $H(z)$ between input $w(n)$ and output $x(n)$ is thus

$$H(z) \equiv \frac{X(z)}{W(z)} = \frac{B(z)}{A(z)}. \quad (3.7)$$

It is easily shown [79] that the output signal power spectral density $P_{xx}(f)$ is related to the noise spectral density $P_{ww}(f)$ by

$$P_{xx}(f) = \frac{|B(f)|^2}{|A(f)|^2} \cdot P_{ww}(f) \quad (3.8)$$

where $A(f)$ and $B(f)$ represent values of $A(z)$ and $B(z)$ respectively, evaluated along the unit circle, $z = \exp(2\pi jf\Delta t)$ for $-1/(2\Delta t) \leq f \leq 1/(2\Delta t)$. Since the noise source $w(t)$ is generally (although not necessarily) assumed white with spectral density $\sigma^2\Delta t$ (where Δt is the sampling interval), equation (3.8) may be rewritten

$$P_{xx}(f) = \sigma^2\Delta t \frac{|B(f)|^2}{|A(f)|^2}. \quad (3.9)$$

If the process is such that $a(k) = 0$ for $k \geq 1$, then

$$x(n) = \sum_{l=0}^q b(l)w(n-l) \quad (3.10)$$

which is termed a moving-average (MA) process of order q since the output is simply a weighted average of the recent input. The power spectrum for such a process is

$$P_{xx}(f) = \sigma^2\Delta t |B(f)|^2. \quad (3.11)$$

Because of the denominator of unity in equation (3.11), a model that gives rise to a strictly moving-average process is termed an all-zero model.

On the other hand, if $b(k) = 0$ for $k \geq 1$ and $b(0) = 1$, then

$$x(n) = - \sum_{k=1}^p a(k)x(n-k) + w(n) \quad (3.12)$$

and the process is strictly an autoregression (AR) of order p , excited by noise. The power spectrum for such a process is

$$P_{xx}(f) = \frac{\sigma^2 \Delta t}{|A(f)|^2} \quad (3.13)$$

and a model that generates such a process is termed all-pole.

Again, the model can be made arbitrarily simple or complex, depending on the choices for AR and MA orders p and q . Note that, for example, if a strictly AR model of first order is chosen, then the system is taken to be no more complicated than a one-pole filter. Indeed, if such an a priori restriction is made, then the transfer function $H(f)$ will have smooth and monotonic magnitude and phase characteristics, regardless of the observed fine structure in $P_{xx}(f)$. The cutoff frequency of the transfer magnitude and phase plots will be dictated by the best-fit location of the pole. The ability to determine a phase relationship in addition to the magnitude plot, and the more appropriate level of detail present in these transfer functions, make this modeling approach far more attractive than simply equating the transfer magnitude with the square root of the process power spectrum as suggested above.

Several algorithms exist to help select the optimal AR model order, so as to minimize the error between the observations and model predictions without introducing spurious detail. Akaike [2] proposed a formula, referred to as the Akaike information criterion (AIC), that is theoretically minimized when the correct AR model order is selected. A similar criterion has been introduced by Parzen [104]. However, it is important to note that the model order chosen may be inappropriately high if either an AR or MA model is assumed when the system in fact behaves as the other. While it would appear the safest approach is to always assume an ARMA model, the task of parameter estimation is most

formidable with such a general model. In fact, for AR models (and not ARMA or MA models), parameter estimation involves solving a set of linear equations, making this class of models the most attractive of the three.

The parameter estimation algorithms for AR models derive from equations that relate the AR parameters to the process autocorrelation function $R_{xx}(k)$, which in turn is estimated from the observed time series. (See section 4.4 for further discussion of autocorrelation function estimation.) It can be shown [79] that if the input excitation to an AR model is white noise with spectral density $\sigma^2\Delta t$, then

$$R_{xx}(k) = \begin{cases} -\sum_{l=1}^p a(l)R_{xx}(k-l), & \text{for } k > 0 \\ -\sum_{l=1}^p a(l)R_{xx}(-l) + \sigma^2, & \text{for } k = 0. \end{cases} \quad (3.14)$$

Expression (3.14) is called the Yule-Walker equation. The $p+1$ parameters $\{a(1), a(2), \dots, a(p), \sigma^2\}$ may be determined by solving $p+1$ equations from equation (3.14), as follows:

$$\begin{bmatrix} R_{xx}(0) & R_{xx}(-1) & \dots & R_{xx}(-p) \\ R_{xx}(1) & R_{xx}(0) & \dots & R_{xx}(-(p-1)) \\ \cdot & & & \cdot \\ \cdot & & & \cdot \\ R_{xx}(p) & R_{xx}(p-1) & \dots & R_{xx}(0) \end{bmatrix} \begin{bmatrix} 1 \\ a(1) \\ \cdot \\ \cdot \\ a(p) \end{bmatrix} = \begin{bmatrix} \sigma^2 \\ 0 \\ \cdot \\ \cdot \\ 0 \end{bmatrix} \quad (3.15)$$

A popular and efficient algorithm for the solution of these equations is the Levinson-Durbin algorithm [88], which recursively computes the parameters for progressively higher order AR models. The validity of

the choices for type and order of model can then be verified through tests of the whiteness of the residuals. The error samples between the observations and model predictions should be uncorrelated with each other if the input excitation $w(t)$ was assumed white noise.

Recently, AR models have been pursued actively in attempts to ascertain and characterize noninvasively the genesis of spontaneous heart rate and blood pressure fluctuations. Kenet et al [80,81] employed such an approach in an investigation of heart rate and pressure fluctuations during both normal sinus rhythm and atrial fibrillation. In remarkably similar work, Cerruti et al [11-13,20,22,103] investigated AR models of neurologically mediated heart rate and blood pressure control. The greatest difficulty that both groups encountered was a lack of whiteness of the residuals. In particular, Kenet found that during normal sinus rhythm, spontaneous heart rate and arterial pressure fluctuations are generally confined to such narrow spectral bands that little information about the system could be inferred from such measurements. For that reason, he felt atrial fibrillation provided a richer state in which to study circulatory dynamics. However, while atrial fibrillation leaves the arterial tree intact and allows for an investigation of vascular mechanical properties that may be extrapolated to the normal state, it severely alters the control of heart rate [29]. Kenet's model of heart rate control based on atrial fibrillation studies thus describes autonomic regulation of atrio-ventricular nodal conduction, and not of normal sino-atrial nodal firing.

Kalli et al [73,74] have extended the AR modelling approach to the development of multivariate autoregressive (MAR) models of heart rate

and blood pressure interaction. In these models, the current value of each system variable is related to the past values of itself and other system variables and to the present value of an excitatory noise signal. Thus,

$$x_i(n) = \sum_{j=1}^r \sum_{k=1}^p a_{ij}(k)x_j(n-k) + w_i(n) \quad (3.16)$$

where r is the number of signals, $w_i(n)$ is the noise source for the signal $x_i(n)$, and $a_{ij}(k)$ represents the set of parameters relating the i^{th} signal to past values of the others. Equation (3.16) leads to the matrix formulation,

$$\mathbf{X}(n) = \sum_{k=1}^p \mathbf{A}(k)\mathbf{X}(n-k) + \mathbf{W}(n) \quad (3.17)$$

in which $\mathbf{X}(n)$ is an $(r \times 1)$ matrix of time series, $\mathbf{A}(k)$ is an $(r \times r)$ coefficient matrix, and $\mathbf{W}(n)$ is an $(r \times 1)$ matrix for residuals. The z -transform of equation (3.17) yields

$$\mathbf{X}(z) = \mathbf{A}(z)\mathbf{X}(z) + \mathbf{W}(z). \quad (3.18)$$

Equation (3.17) may be solved recursively using the Levinson-Durbin algorithm, as in the univariate case.

A difficulty encountered with MAR models is that even if the system were known exactly, the model order p could depend on the chosen sampling rate of the signals. This troublesome state of affairs relates to the fact that the cross-correlation between two signals, unlike an autocorrelation function, does not necessarily peak at a lag time of zero. Since the model described by equation (3.16) includes terms for all k

between 1 and the model order p , the number of terms required to characterize a system delay will depend on the number of samples that span the delay period, which is obviously related to the sampling rate. As in the univariate case, after choosing the model order, the set of residuals $w_j(n)$ should be checked for whiteness as a first test of model validity.

In their implementation of MAR model analysis of heart rate and blood pressure fluctuations, Kalli et al [74] found substantial variation in the whiteness of residuals between subjects, making interpretation of their results difficult. Nonetheless, their analysis provides some insight into the degree of coupling between heart rate and arterial pressure inherent in cardiovascular regulation, and represents a promising direction for further work.

3.5 Analyses Using Exogenous Input Excitation

To avoid the limitations inherent in analyses based on spontaneous fluctuations and to characterize autonomic function with greater resolution and accuracy, many investigators have invoked methods in which a time-varying waveform is applied as a system excitation, the resulting output signal or signals are measured, and transfer relations are estimated quantitatively. Such a procedure may be employed in either closed- or open-loop preparations, and analyzed using either time- or frequency-domain techniques.

Efforts to quantify the heart rate response to changes in sympathetic and vagal activity began in 1962 when Warner and Cox [136]

presented a mathematical model that could emulate the behavior of the sino-atrial node using second-order differential equations to describe the release, reuptake, and degradation of neurotransmitter at the synapses between the autonomic nerves and the sino-atrial node. Several years later, Katona et al [78] found that the Warner and Cox model performed at least as well when simplified to a first-order linear differential equation. Considerable controversy between these two groups ensued [76], and the precise dynamics of the sino-atrial node response have never been adequately resolved.

In the 1960's researchers also began to explore the response of the autonomic nervous system to time-varying perturbations in blood pressure. Several workers examined the transient response of the baroreceptor reflex by applying step changes or impulses of pressure to the externally perfused baroreceptors and observing the resulting effect on heart rate and systemic arterial pressure in the time domain [48,65,75,76,89,123]. This pioneering work led to the approximate determination of characteristic delays in the various branches of the autonomic nervous system [78] and demonstrated the presence of nonlinearities in the system [40,48,65,75,76,124].

Shortly after researchers began the time domain analyses of the baroreceptor reflex, others started to approach the problem in the frequency domain. Scher and coworkers [123] developed methods for imposing sinusoidal pressure variations at a range of frequencies in the arterial vessels containing the baroreceptors by employing a servo mechanism. They then related the observed oscillations in heart rate and systemic arterial pressure to the input signal in terms of a transfer magnitude

and phase as a function of frequency of the input sinusoid. These investigators, as well as others who performed similar studies [49,89,93,118,122,125,129], encountered several obstacles that reduced the significance of their results. First, in all experiments in which the autonomic feedback loop was opened (by surgically isolating the baroreceptive vessels from the rest of the arterial vasculature), the animals were anesthetized and thus in a non-physiologic state, and in all the experiments in which the animals were in a normal awake state, the feedback loop was left intact. (In the latter case, the exogenous servo mechanism that is attempting to impose a desired pressure waveform must compete with the animal's intrinsic control system which is attempting to eliminate these pressure oscillations [118,122,125].) Secondly, although the intended pressure signal in these studies was a sinusoid, nonlinearities in the mechanical interface between the servo system and the arterial tree, as well as the addition of mechanical noise, distorted the input signal. Similarly, nonlinearities in the response of the system being studied produced harmonic distortion in the output signal (either heart rate or systemic pressure). This last problem was particularly troublesome when large amplitude oscillations were used as input signals. Thus, rather than deducing a transfer function to characterize the baroreceptor reflex, these workers were actually computing describing functions [49,89,93,122,123,125,129], in which only the fundamental component of the output signal is related to that of the input. In fact, in none of these studies was any attempt made to quantify the degree of corrupting noise and nonlinearities. Finally, in all of these studies, measurements were made around only a single operating point, mostly because of time constraints, since the determination of a

single describing function required driving the system many times at different frequencies.

3.6 Nonlinear Analysis

The foregoing discussion of the previous research efforts that have led to our current understanding of autonomic regulation points out the areas in which further work is required. We still lack an adequate quantitative characterization of the system's nonlinearities, its small signal response over the full normal operating regime, and its response in situations in which the cardiovascular system is stressed. The first of these issues, the nonlinearities inherent in the system function, is the most difficult to analyze and resolve.

Volterra [135] developed a mathematical formulation for the representation of a nonlinear system in terms of a sum of progressively higher order functionals in much the same way that a nonlinear function can be represented by a sum of progressively higher order polynomials in a Taylor series. He showed that for a system S that is nonlinear, time invariant, analytic, and has finite memory, the relationship between input $x(t)$ and output $y(t)$ can be written as

$$\begin{aligned}
 y(t) &= S[x(t)] \\
 &= k_0 + \int k_1(\tau)x(t-\tau)d\tau \\
 &\quad + \iint k_2(\tau_1, \tau_2)x(t-\tau_1)x(t-\tau_2)d\tau_1d\tau_2 \\
 &\quad + \iiint k_3(\tau_1, \tau_2, \tau_3)x(t-\tau_1)x(t-\tau_2)x(t-\tau_3)d\tau_1d\tau_2d\tau_3 \\
 &\quad + \dots
 \end{aligned} \tag{3.19}$$

where k_0 , $k_1(\tau)$, $k_2(\tau_1, \tau_2)$, $k_3(\tau_1, \tau_2, \tau_3)$, ... are known as the Volterra kernels of the system. These kernels are symmetric functions of their arguments (e.g., $k_2(\tau_1, \tau_2) = k_2(\tau_2, \tau_1)$), and for a causal system, $k_n(\tau_1, \dots, \tau_n) = 0$ if any of the arguments τ_1, \dots, τ_n are negative. Thus, all integrations are taken from zero to infinity. The zeroth-order kernel k_0 is a constant and is simply the response of the system to a zero input (i.e., when $x(t) = 0$). Notice that the first-order functional is exactly the convolution integral for a linear system. In fact, if $k_0 = 0$ and all kernels above the linear kernel are zero (i.e., $k_n = 0$ for $n \geq 2$), then equation (3.19) reduces to

$$y(t) = \int k_1x(t-\tau)d\tau \tag{3.20}$$

and the system is linear with impulse response $k_1(\tau)$.

In 1958, Norbert Wiener presented a tremendously useful wrinkle on the Volterra formulation. (Interestingly, he published his contributions in this field only in a book [140] transcribed from tape recordings of a lecture series he gave at M.I.T.) Wiener suggested that just

as there exists a Fourier series representation of a periodic signal comprised of a complete set of orthonormal basis functions (sinusoids), so too can a series of orthogonal functionals be created to represent a nonlinear system. The advantage of a series of orthogonal functionals over the series of Volterra functionals is that if the series of orthogonal functionals $H_n[x(t)]$ is truncated after any finite number N terms and the residual error e_N

$$e_N = \int_0^\infty \left[S[x(t)] - \sum_{n=0}^N H_n[x(t)] \right]^2 dt \quad (3.21)$$

is minimized, then those N terms will be the same as the first N terms of the series extended to M terms (for $M > N$) when e_M is minimized.

The use of a set of orthogonal functionals, however, imposes restrictions on the class of allowed input signals $x(t)$ for which the representation is valid. The most commonly used form of the Wiener representation is

$$y(t) = \sum_{n=0}^{\infty} H_n[x(t)] \quad (3.22)$$

where the first four orthogonal functionals are:

$$H_0[x(t)] = h_0 \quad (3.23a)$$

$$H_1[x(t)] = \int h_1(\tau)x(t-\tau)d\tau \quad (3.23b)$$

$$H_2[x(t)] = \iint h_2(\tau_1, \tau_2) x(t-\tau_1) x(t-\tau_2) d\tau_1 d\tau_2 - P \int h_2(\tau_1, \tau_1) d\tau_1 \quad (3.23c)$$

$$H_3[x(t)] = \iiint h_3(\tau_1, \tau_2, \tau_3) x(t-\tau_1) x(t-\tau_2) x(t-\tau_3) d\tau_1 d\tau_2 d\tau_3 - 3P \iint h_3(\tau_1, \tau_2, \tau_2) x(t-\tau_1) d\tau_1 d\tau_2. \quad (3.23d)$$

This representation requires that the input signal be Gaussian white noise, and the constant P refers to the variance of the input noise.

Lee and Schetzen [87] presented a method for experimentally evaluating the kernels $h_i(\tau_1, \dots, \tau_i)$ of the Wiener representation by utilizing crosscorrelation techniques. To use their procedure, a single experiment is performed on the system with a zero-mean Gaussian white noise input $x(t)$, and the system response $y(t)$ is recorded. The kernels are then found recursively using the relation

$$h_n(\tau_1, \dots, \tau_n) = \frac{1}{n!P^n} E \left[\left[y(t) - \sum_{m=0}^{n-1} H_m[x(t)] \right] x(t-\tau_1) \cdots x(t-\tau_n) \right]. \quad (3.24)$$

Note that the right side of equation (3.24) is found by first computing the residual of $y(t)$ after subtracting off the part of the response that is accounted for by the first $n-1$ functionals, and then computing the n^{th} order crosscorrelation function with $x(t)$.

Several investigators have applied this approach to the study of nonlinearities in neural systems such as retinal cell chains [96] and pupillary control networks [130]. While a number of researchers have noted the importance of nonlinearities in cardiovascular regulation,

particularly in the response characteristics of the baroreceptors [27,40,48,65,75,89,124], use of the Wiener or Volterra kernel analysis in studying cardiovascular control has been scant [1]. On the other hand, the Wiener series representation (and the Lee and Schetzen identification technique) has several disadvantageous attributes that are direct consequences of the very generality of the method. For one, although systems engineers have gained enough intuition to interpret the first-order Wiener kernel, few people can readily interpret the higher order kernels either from their shape or analytic form. In addition, computation of third and higher order kernels is so burdensome that few investigators have even attempted to represent a nonlinear system with more than the first and second order terms. Thus any higher order nonlinearities could not be included in such a characterization of the system.

3.7 Transfer Function Analysis

In planning the research efforts described in this thesis, I sought a systems analysis approach that would provide for an accurate and readily interpretable system description that could be obtained efficiently to allow for serial characterizations as conditions changed. Thus, I was willing to trade off the generality afforded by the nonlinear analysis described above for a computationally simpler and more easily understood representation of cardiovascular regulatory dynamics. At the same time, since I was particularly interested in characterizing the functional delays in the system that may give rise to resonances and instabilities, I felt the acquisition of phase information was crucial.

Furthermore, I felt that with the introduction of spectrally broad-band waveforms as measurable system input signals, I could obtain more detailed and accurate characterizations than those afforded by autoregressive analyses, where the system excitation is assumed unmeasurable. Broad-band stimulation also enables the determination of system response characteristics over the full range of a desired frequency band without requiring multiple test runs, as in analyses based on sinusoidal input excitations.

While I recognize nature is inherently nonlinear, for the purposes of this thesis research, I make two important assumptions regarding the nonlinearities in the operation of the cardiovascular control system. First, I assume that for sufficiently small fluctuations around the operating point, the system behaves linearly. Second, I assume that the only significant nonlinearity is a dependence of the small signal transfer function on the operating point. Given these conditions, the control system can be well described by a family of bode plots generated by varying the operating point as the parameter.

The limiting assumptions mentioned above prevent me from examining nonlinearities such as those in which the cross-correlation between the input and output signals depends not just on the delay between them, but also on the state of the system at some other point(s) in time. On the other hand, saturation and other high-order gain nonlinearities can be explored and characterized. These nonlinearities can be represented by rearranging the data from the bode plots so as to graph transfer function magnitude (and phase) against operating point with frequency as the parameter instead of the abscissa. Note that I have used the term

"operating point" loosely, as it could (and will) refer to the mean frequency at which a nerve is stimulated, the mean value around which the arterial pressure fluctuates, or the mean cardiac output.

When a spectrally broad-band signal is applied at the system input, a local transfer function $H(f)$ (i.e., determined at a specific operating point) can be determined from the input signal autospectrum $S_{xx}(f)$ and input-output cross-spectrum $S_{xy}(f)$ using the relation [70],

$$H(f) = \frac{S_{xy}(f)}{S_{xx}(f)}. \quad (3.25)$$

Statistical techniques used in the spectral estimation will be covered in detail in Chapter 4. Note that since the cross-spectrum $S_{xy}(f)$ is in general complex, the transfer function estimate $H(f)$ will also be complex. This complex value at each frequency can be decomposed into a magnitude and phase component. The basic prerequisite for implementation of this approach, aside from the restrictions on system nonlinearities discussed above, is that the input excitation must contain significant energy compared to the level of corrupting (unmeasured) noise at all frequencies for which a system characterization is desired. The input signal therefore ought to be of a broad-band nature and readily measurable. The generation of such broad-band signals for use as the input excitation will be discussed in the methods sections of Chapters 5, 6, and 7.

Transfer function analysis is a powerful approach toward studying system behavior not only because it affords both magnitude and phase characterizations, but also because it allows for the computation of a

measure of confidence in the results obtained, the coherence function. The ordinary coherence function $\gamma^2_{xy}(f)$, is found from the input autospectrum $S_{xx}(f)$, the output autospectrum $S_{yy}(f)$, and the cross-spectrum $S_{xy}(f)$ using the relation [70],

$$\gamma^2_{xy}(f) = \frac{|S_{xy}(f)|^2}{S_{xx}(f)S_{yy}(f)}. \quad (3.26)$$

A coherence value of unity at a particular frequency implies perfectly linear operation of the system under study and an absence of corrupting noise in the system. Where the coherence function falls substantially from unity either the system functions less ideally or there exists additive noise that makes the transfer function estimate at those frequencies less reliable. This is discussed in greater detail in Section 4.5.

The diffusion of transfer function analysis into the fields of cardiovascular regulation and autonomic control has been remarkably slow. (Implementation of the related but inexpedient approach of describing function analysis was discussed in Section 3.5.) Zwiener [142] computed phase and coherence functions between heart rate, blood pressure, and respiration in man, but based his analysis on measurements of spontaneous fluctuations in these signals. Since spontaneous fluctuations in hemodynamic variables are not typically of a broad-band nature, Zwiener found good coherence between the measured signals only within fairly narrow frequency bands, rendering his phase spectra difficult to interpret. In addition, the finding of good coherence between spontaneously fluctuating signals can not, in general, be extrapolated to imply a causal relationship between one signal and another [70], because both

may simply be varying in accordance with a third, unmeasured, signal. By contrast, fluctuations that appear in a signal and are coherent with an imposed input excitation can be interpreted as causally related to the input activity.

In a rare application of broad-band stimulation of the cardiovascular system, Taylor [133] applied randomly timed pacing impulses to the cardiac atria of experimental animals and characterized the transmission line properties of the arterial tree through the computation of an effective impedance function. He found that the impedance of the arterial system was depressed at very low frequencies (less than 0.03 Hz). Taylor pointed out that this behavior indirectly demonstrates the presence of compensatory mechanisms within the ANS that modulate arterial resistance. He made no attempt, however, to explicitly characterize the dynamic response of the ANS in performing this function. In Chapter 7, I describe how Taylor's approach can be modified to enable investigation of the open-loop transfer properties of the ANS.

Chapter 4: Signal Processing Techniques

The studies described in Chapters 5, 6, and 7 are designed to explore different components implicated in cardiovascular regulation. They are similar, however, in that they share a common approach, including methods of data analysis. The analysis consists of 1) recording various hemodynamic signals during broad-band system excitation, 2) analog filtering, sampling, and digital processing of the signals, 3) implementation of the transfer function analysis introduced in Chapter 3, and 4) pooling of data from the experiments within each study. In this chapter, I outline the analysis techniques employed in these studies.

4.1 Recording of Physiologic Signals

The steps involved in recording, filtering, sampling, and preprocessing the hemodynamic signals are tailored to the specific properties of these waveforms. In particular, in recording the signals, it is unnecessary to use equipment whose response bandwidth is wider than the range of frequencies present in the signals. Since the recording bandwidth is proportional to the tape speed, it is wasteful (and expensive) to run the tape recorder at speeds higher than that required for the desired bandwidth.

Another important consideration in the design of experiments and the recording of physiologic signals is the length of time required for each data segment. On the one hand, biologic systems are often non-stationary, making spectral analysis inappropriate for very long

records, especially when experimental conditions are changing or the signals are clearly drifting away from their initial values. Also, the desire to develop a practical clinical tool dictates that the analysis not require inordinately long periods of data collection. On the other hand, the frequency resolution of the analysis routine (i.e., the minimum difference in frequency between two independent points of a spectral estimate) is inversely proportional to the length of the data segment. A tradeoff thus exists between experimental convenience and frequency resolution of the analysis.

The signals analyzed in the studies that comprise this thesis research are of two types. The first category consists of signals that are measured directly, including arterial blood pressure, aortic flow, and respiration. The second type of signal is one that is derived from a measured waveform. Two such signals are the heart rate and the instantaneous rate of neural stimulation. The heart rate is derived from the electrocardiogram (ECG), and the neural stimulation rate is determined from recordings of the stimulatory spikes. The requisite bandwidth of the taping equipment used to record the signals for off-line analysis is dictated by the signal with the widest spectral content. Thus, even though the blood pressure, flow, and respiratory signals lack significant power density beyond roughly 20 Hz, a recording bandwidth of several hundred Hz is required to accurately capture the morphology of the ECG's QRS complexes and the neural stimulatory spikes. High fidelity recordings of these signals are essential to enable accurate determination of the timing of cardiac and nerve activations in order to derive the respective instantaneous rate signals.

All experiments were recorded on a Hewlett-Packard model 3968A 8-channel FM tape recorder, with a tape speed of 1 7/8 inches/sec. The bandwidth at this speed is 625 Hz. Data segments were just over 6 minutes (364 seconds) long, allowing for a maximum spectral resolution (minimum Δf) of .00275 Hz. The actual spectral resolution realized in these studies was, in fact, somewhat poorer than this due to the application of spectral smoothing, described in Section 4.4.

4.2 Sampling, Filtering, and Decimating

The off-line analysis of recorded data begins with digitization of the signals through a 12-bit analog-to-digital (A/D) converter connected to and controlled by the Motorola 68010-based computer (Masscomp MC-500) that processes the data. All signals are sampled at the same rate, and the choice of sampling frequency is governed by three considerations. First, since all samples are stored in two-byte words on limited disk space, the sampling rate should be no higher than necessary. Second, Nyquist's theorem states that the sampling rate must be at least twice the highest frequency present in the signal to avoid aliasing [102]. Third, and perhaps most constraining, the accuracy of the algorithm that determines the instantaneous rate signals is directly related to the error in event interval measurements. Since the software that determines event intervals can attain only discrete values where the quantization error is the time between consecutive samples, the sampling rate must be high enough to adequately limit this error.

For most of the experiments, the sampling rate was 360 Hz, thus limiting the interval measurement error to 2.7 msec. The instantaneous

rate r (in units of min^{-1}) is related to the event interval t (in units of seconds) by

$$r = \frac{60}{t}. \quad (4.1)$$

If the true event interval were $\Delta t = .0027$ sec larger than the measured interval t , then the true instantaneous rate r' would be

$$r' = \frac{60}{t + \Delta t}. \quad (4.2)$$

The error Δr in the instantaneous rate measurements is thus

$$\begin{aligned} \Delta r \equiv r - r' &= \frac{60}{t} - \frac{60}{t + \Delta t} \\ &= \frac{60 \Delta t}{t(t + \Delta t)} \\ &\approx \frac{60 \Delta t}{t^2}. \end{aligned} \quad (4.3)$$

For heart rates around 100 beats/min., $t \approx .6$ sec, and the rate error $\Delta r = .45$ beats/min. This was adequate in all but one series of experiments, discussed in Chapter 5, where the error was halved by sampling the signals at 720 Hz.

Since the ECG (and all other signals) contain insignificant power at frequencies beyond 180 Hz, sampling at 360 Hz would appear to satisfy Nyquist's criterion for avoidance of aliasing. However, superimposed on all signals is a substantial broad-band noise floor originating predominately in the FM magnetic tape medium. It is therefore wise to filter out high frequency components in the signals when sampling them. All signals were thus passed through 6-pole Butterworth filters en route

from the tape recorder to the A/D converter. The filter bank's band-pass edge is set to half the sampling frequency or even lower.

Although several hundred samples of each signal are acquired each second to allow for accurate temporal location of ECG and neural events, neither the instantaneous event rate signals nor the other hemodynamic signals need be represented by more than a few samples per second. This is because signal content related to autonomic regulatory dynamics is confined to frequencies below 1 Hz [4,24,86,103,108,120,125,142]. In fact, a number of researchers [86,93,133] believe the frequency band between D.C. and 0.1 Hz to be the most germane in studying cardiovascular control. The directly measured hemodynamic signals (arterial pressure, aortic flow, and respiration) may thus be decimated by a factor of 100 or more from their original sampling rates of 360 Hz or 720 Hz. We, in fact, decimate these signals down to an effective sampling rate of 2.8125 Hz. From an initial sampling rate of 360 Hz, this represents a decimation factor of 128, and from 720 Hz the decimation factor is 256. The band-pass edge of the analog anti-aliasing filters for these signals is generally set to 90 Hz, allowing for decimation from 360 Hz to 180 Hz (factor of 2) without any risk of introducing aliasing. The remaining decimation (factor of 64) down to 2.8125 Hz must be preceded by digital low-pass filtering. This operation is performed in three stages; each stage involves the application of a low-pass filter and decimation by a factor of 4. The filter program utilizes the overlap-add method [102] to convolve efficiently the data stream with a 31-point symmetric filter window. Time and frequency domain representations of this window are shown in Figure 4.1. Note that the filter passes frequencies between

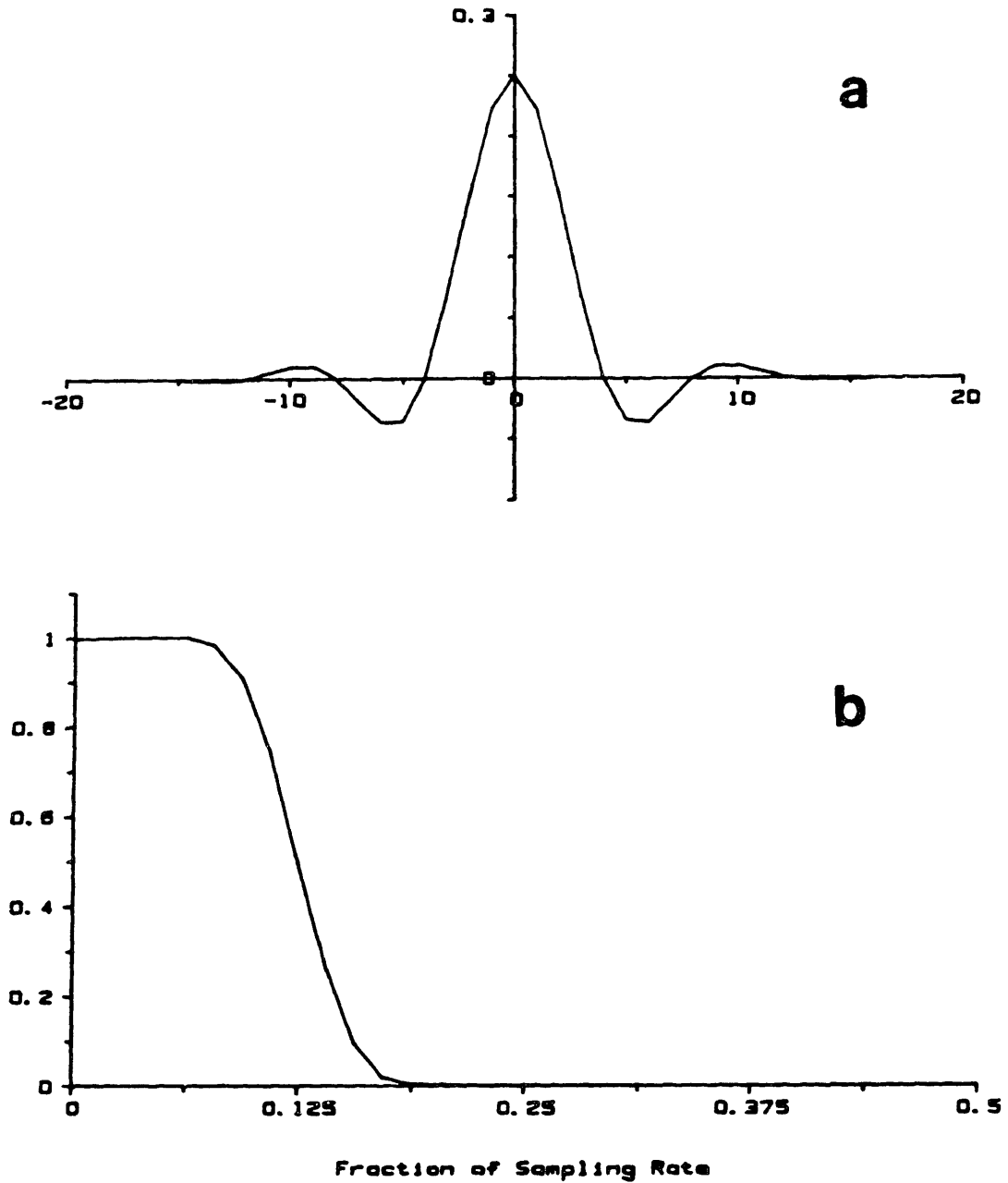


Figure 4.1. Time-domain representation of digital low-pass filter (a) and its Fourier transform (b) used to prevent aliasing when decimating data by a factor of 4. The symmetric time window is 31 points long, plotted from -15 to 15 in (a). The frequency-domain representation (b) shows that the pass-band extends from D.C. to $f_s/8$.

D.C. and $f_s/8$, where f_s is the sampling frequency. The output of this filter may then be decimated by a factor of 4 without the introduction of aliasing.

Derivation of the instantaneous heart rate and neural stimulatory rate signals does not involve any decimation procedure, per se. Once the temporal locations of the R waves in the ECG and the neural stimulatory spikes have been determined using a peak detection routine, values for the corresponding instantaneous event rate signals are simply computed at time intervals of $1/2.8125 = .3556$ seconds. Care must be taken, nonetheless, to insure that these instantaneous rate signals are free of aliasing artifacts. The algorithm developed to perform this operation is presented in the following section.

At this point, the seemingly arbitrary choice of 364 seconds as the length of data records can be explained. The data analysis involves the computation of Fourier transforms, for which we employ the Fast Fourier Transform algorithm [30]. The maximum computational efficiency of this algorithm is realized when the data stream length is a power of 2. Consequently, we analyze 1024 sample values of each signal at a time, which yields a record length T of

$$T = \frac{1024 \text{ samples}}{2.8125 \text{ samples/sec.}} = 364 \text{ seconds .} \quad (4.4)$$

4.3 Derivation of the Heart Rate Signal*

4.3.1 Difficulties in Defining Heart Rate

In Chapter 2, I pointed out that there exist some subtleties in computing a meaningful heart rate signal. This signal is derived from timing measurements of the ECG, and is poorly defined between cardiac activation events. Over the past several years, heart rate variability has been studied extensively in our laboratory [3,4,95,108] and elsewhere [28,33,35,63,84,85,94,101,103,108,113,120,142]. A considerable degree of debate has arisen concerning the definition of instantaneous heart rate and the development of algorithms to compute a heart rate signal. We have developed an approach that enables efficient derivation of an instantaneous rate signal that makes intuitive sense and is easily utilized in both autospectral and cross-spectral analyses. While the following discussion is geared toward the heart rate signal in particular, the algorithm is equally well suited to the derivation of any other instantaneous event rate signal, such as the instantaneous neural stimulatory rate.

4.3.2 Previous Algorithms for Heart Rate

In a recent paper [33], DeBoer et al compared two methods that employ spectral analysis for the study of heart rate variability. In a second paper [35], the same authors presented an evaluation of these two methods and of a third by testing each on a sequence of simulated RR

* Much of the text of this section has been published in a communication article of the IEEE Transactions on Biomedical Engineering [16].

intervals generated by an integral pulse frequency modulation (IPFM) model. An IPFM model is a device that integrates its input signal until the result of this integration reaches a preset threshold, at which point the device sends out a pulse, resets the integrator to zero, and begins the integration anew. Hyndman and Mohn [64] first suggested the IPFM model as a functional description of the sino-atrial node, and it remains a useful model for the mechanism by which the autonomic nervous system modulates heart rate. We can represent the operation of an IPFM model mathematically as

$$\bar{T} = \int_{t_k}^{t_{k+1}} (1 + m(t))dt. \quad (4.5)$$

\bar{T} is the integrator's threshold value, which equals the duration of each RR interval were there no autonomic modulation of the SA node's intrinsic firing rate. The input signal is $s(t) = 1 + m(t)$, where all autonomic influences are lumped together in this model and are represented by $m(t)$. Obviously, when $m(t)$ increases, the RR interval shortens so that the instantaneous heart rate varies in proportion to $s(t)$. t_k is the time of the k^{th} R wave.

In their evaluation of the performance of the various spectral techniques for analysis of heart rate variability, DeBoer et al compared the results of each method to the spectrum of the input signal applied to the IPFM model that generated the simulated RR intervals. They considered the latter as the "true" heart rate spectrum. These investigators demonstrated that all three of the methods they considered introduce significant artifacts that corrupt the spectra and made them differ from the "true" spectrum.

DeBoer et al labeled the three types of power spectral estimates that they discussed as (1) the spectrum of inverse intervals, (2) the spectrum of intervals, and (3) the spectrum of counts. (For a detailed description of the methods involved in the computation of these spectra, see references [33,35].) The spectrum of inverse intervals is the discrete Fourier transform (DFT) squared of the sequence of numbers corresponding to the reciprocals of the RR interval durations. Each number in the sequence corresponds to a single beat; this obviously results in uneven sampling of the process in time. Since these numbers are evenly spaced only when plotted against beat number, the units of the frequency axis of this spectrum are "cycles per beat" instead of "cycles per second." While the number of cycles per beat can be converted to an average number of cycles per second by multiplying the former by the average heart rate, it is not surprising that this spectrum would differ in appearance from that of the input signal to an IPFM model that generated these RR intervals. For example, if the IPFM model's input were a sine wave, then there would be relatively fewer beats (and thus RR intervals) around the sine wave's minima, and relatively more when the sine wave is near its maxima. Thus the spectrum of inverse intervals is the DFT squared not of a sampled sine wave, but rather of a distorted sinusoid-like signal that appears alternately stretched out and compressed. Clearly, such a spectrum will contain harmonics of the fundamental sine wave.

The spectrum of intervals is similarly the DFT squared of a sequence of numbers in which there exists one number for each beat. In this case, however, the values of the numbers that comprise the sequence

are the RR interval durations themselves. These values are inversely proportional to the input signal applied to the IPFM model. Thus the spectrum of intervals appears as the spectrum of a signal derived from the IPFM model's input signal after it has been both time-warped and inverted. Not surprisingly, the harmonics present in this spectrum are often even larger than in the spectrum of inverse intervals.

The spectrum of counts is the Fourier transform squared of a set of unit area delta functions on a true time axis spaced according to the sequence of RR intervals. This power spectral estimate, denoted $P_C(f)$, can be computed analytically as

$$P_C(f) = \frac{t_N}{N^2} \left[\left[\frac{N \sin(2\pi f t_N)}{2\pi f t_N} - \sum_{k=1}^N \cos(2\pi f t_k) \right]^2 + \left[\frac{N(\cos(2\pi f t_N) - 1)}{2\pi f t_N} + \sum_{k=1}^N \sin(2\pi f t_k) \right]^2 \right] \quad (4.6)$$

where N is the number of delta functions in the record and t_k denotes the location in time of the k^{th} impulse. (Note that equation (4.6) contains terms that compensate for the truncation effects that result from computing the Fourier transform of a finite set of delta functions.) Rompelman et al [115] have presented a modification of this technique for efficient computer implementation. Since this spectrum is that of a true time signal, it is free of harmonic artifacts like those seen in the spectrum of intervals and the spectrum of inverse intervals. On the other hand, when the intervals are generated by an IPFM model, the spacing of the delta functions (not their amplitude) is modulated by the input signal applied to the model. Thus artifacts will appear in the

spectrum of counts at sidebands of the mean repetition rate, since it is a frequency modulated process.

4.3.3 Description of New Heart Rate Algorithm

In Figure 4.2 is shown a schematic of the algorithm we use to derive a heart rate signal from the ECG. The steps involved are as follows. After sampling the ECG and determining R-wave locations to the nearest sample point, a sampling frequency f_r for the heart rate signal is chosen. This is a true frequency (i.e., the heart rate samples will be evenly spaced in time at this frequency), and may be chosen arbitrarily, without regard to the mean heart rate or the frequency at which the ECG is sampled. For synchrony with the decimated blood pressure, flow, and respiratory signals, we select $f_r = 2.8125$ Hz, as mentioned above. A "local window" is then defined at each heart rate sample point as the time interval extending from the previous sample to the next. We then count the number of RR intervals (including fractions thereof) that occur within this local window. Examples of how we compute fractional RR intervals are shown in Figure 4.2. The value r_i of the heart rate at each sample point is taken to be

$$r_i = f_r \cdot n_i / 2 \quad (4.7)$$

where n_i is the number of RR intervals that fall in the local window centered at the i^{th} sample point. Finally, we determine the heart rate power spectrum from the sequence of heart rate samples, using the estimation techniques discussed in Section 4.4*.

* In this section, to allow for comparison with the results of DeBoer et

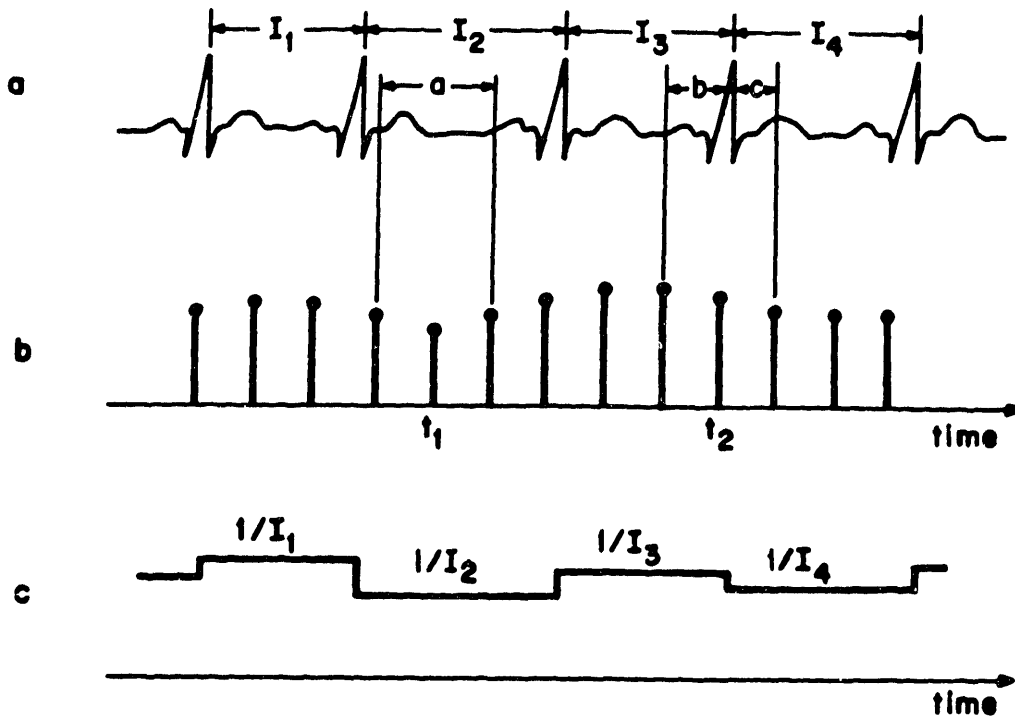


Figure 4.2. a. A segment of an ECG signal. b. The heart rate samples corresponding to the ECG signal in (a), determined using our algorithm. The number of RR intervals within the local window centered at t_1 is a/I_2 , and at t_2 is $b/I_3 + c/I_4$. The value of the heart rate at each sample point is taken to be the number of intervals that fell within the local window centered at that point divided by the width of the window, as described in the text. c. The corresponding instantaneous heart rate signal. The value held during each interval is the reciprocal of the duration of that interval.

Several observations may be made regarding this technique. Obviously, since the heart rate at each point depends on events in the ECG both in the recent past and the near future, this method can not be employed in real time analysis without incurring a delay. The heart rate signal produced by our algorithm may equivalently be viewed as samples of a step-wise continuous instantaneous heart rate signal convolved with a rectangular ("boxcar") window. This step-wise continuous instantaneous heart rate signal maintains an amplitude equal to the reciprocal of the current RR interval, for the duration of that RR interval (see Figure 4.2c). This signal differs from traditional tachometer signals (see for example Figure 1b in [33]) in that the value held during the k^{th} interval is $1 / (t_{k+1} - t_k)$, not $1 / (t_k - t_{k-1})$. As DeBoer et al have recently noted [36], the traditional tachometer signal is flawed on two counts. First, the signal lags the ECG by an entire beat, which may be inconsequential in autospectral analysis, but can introduce artifactual phase shifts in cross-spectra, for example, between heart rate and blood pressure or respiration. Secondly, the traditional tachometer signal provides a biased estimate of the heart rate since the lowest values are held for too short an amount of time, and the highest values are held for inappropriately long intervals. The mean heart rate thus appears higher than it should. The non-delayed instantaneous heart rate signal in Figure 4.2c avoids both of these complications.

al [33,35], all spectra (except those computed from analytic expressions) were estimated using the Blackman-Tukey algorithm [79], employing a Bartlett window. Also to facilitate this comparison, all power spectral estimates have been normalized by dividing by the square of the mean of the input signal. Finally, amplitude spectra (i.e., the square root of the corresponding power spectra), as opposed to the power spectra themselves, are displayed in Figures 4.4, 4.5, and 4.6 to emphasize the presence of harmonics and other artifacts.

Convolution of the heart rate signal with the rectangular window has the effect on the power spectrum of multiplication by a low-pass filter. The shape of the filter $W(f)$ is

$$W(f) = \left[\frac{\sin(2\pi f/f_r)}{2\pi f/f_r} \right]^2 \quad (4.8)$$

where, again, f_r is the sampling frequency of the heart rate signal, so that $2/f_r$ is the width of the rectangular window in the time domain. This filter, plotted in Figure 4.3, passes very little power beyond the Nyquist rate (i.e., $f_r/2$), and its effects can be compensated for in the band $0 < f < f_r/2$ by multiplying the power spectrum by $1 / W(f)$. In practice, we apply a $1 / W(f)$ correction, but consider the spectral estimate accurate only for $0 < f < f_r/4$, since the multiplication by $1 / W(f)$ significantly amplifies any aliased power in the band $f_r/4 < f < f_r/2$.

It should be noted that a power spectral estimate $P_S(f)$ for the step-wise continuous signal shown in Figure 4.2c can be computed analytically without the need to generate samples of the signal using the relation,

$$P_S(f) = \frac{t_N}{(2\pi f N)^2} \left[\left[\sum_{k=1}^N \left[\frac{1}{t_{k+1}-t_k} - \frac{N}{t_N} \right] (\cos(2\pi f t_{k+1}) - \cos(2\pi f t_k)) \right]^2 + \left[\sum_{k=1}^N \left[\frac{1}{t_{k+1}-t_k} - \frac{N}{t_N} \right] (\sin(2\pi f t_{k+1}) - \sin(2\pi f t_k)) \right]^2 \right] \quad (4.9)$$

where N is the number of steps in the period of observation and t_k is the time at the beginning of the k^{th} step. This technique generates spectral estimates whose only artifacts are the result of the small

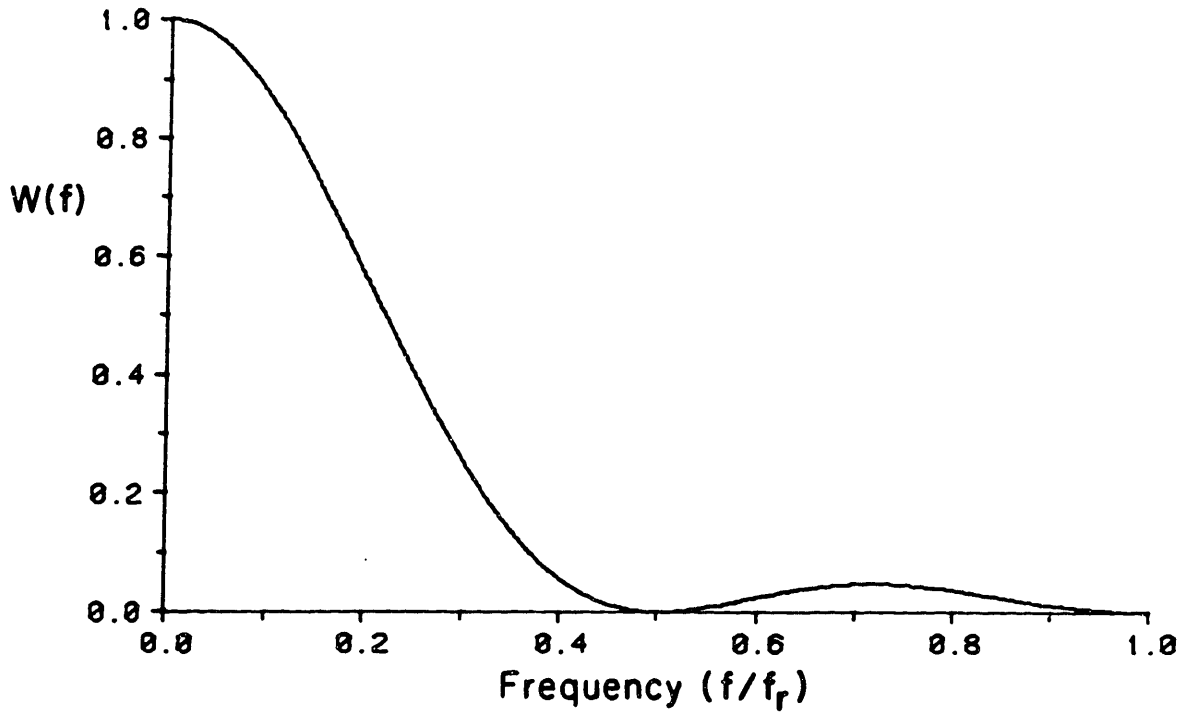


Figure 4.3. Filter shape that results from use of a rectangular window in the computation of the heart rate. The frequencies on the abscissa are multipliers of the sampling frequency f_r .

amount of generally high frequency power inevitably present in the discontinuities between adjacent steps. However, it is not a practical method because the evaluation of equation (4.9) for many different frequencies is computationally very burdensome and can not be made more efficient through the use of FFT-like algorithms.

On the other hand, mere sampling of the step-wise continuous instantaneous heart rate signal at a rate f_r without first filtering it results in aliasing artifacts in the corresponding power spectrum. To demonstrate this we first computed analytically (using equation (4.9)) the spectrum of the step-wise continuous heart rate signal corresponding to a sequence of intervals produced by an IPFM model, where the input signal $s(t)$ was

$$s(t) = 1 + m \cos(2\pi f_m t). \quad (4.10)$$

The modulation depth m was chosen as .3, the modulation frequency f_m was .16 Hz, and the IPFM threshold (also the mean interval duration) was 1.05 sec. These are the same parameters used by DeBoer et al [35] in their simulation. The amplitude spectrum $(P_S(f))^{1/2}$ for this simulation is shown in Figure 4.4a for frequencies between D.C. and 2 Hz.

Harmonics of the modulation frequency as well as a substantial peak at the mean heart rate (.952 Hz) can be clearly seen in Figure 4.4a. Next, shown in Figure 4.4b, is the amplitude spectrum of a sequence of samples taken from the unfiltered step-wise continuous heart rate signal corresponding to the same simulation, where the sampling rate f_r was 1.2 Hz. The peak at the mean heart rate has become aliased and appears as a spectral component at .248 Hz, which is well into the band of

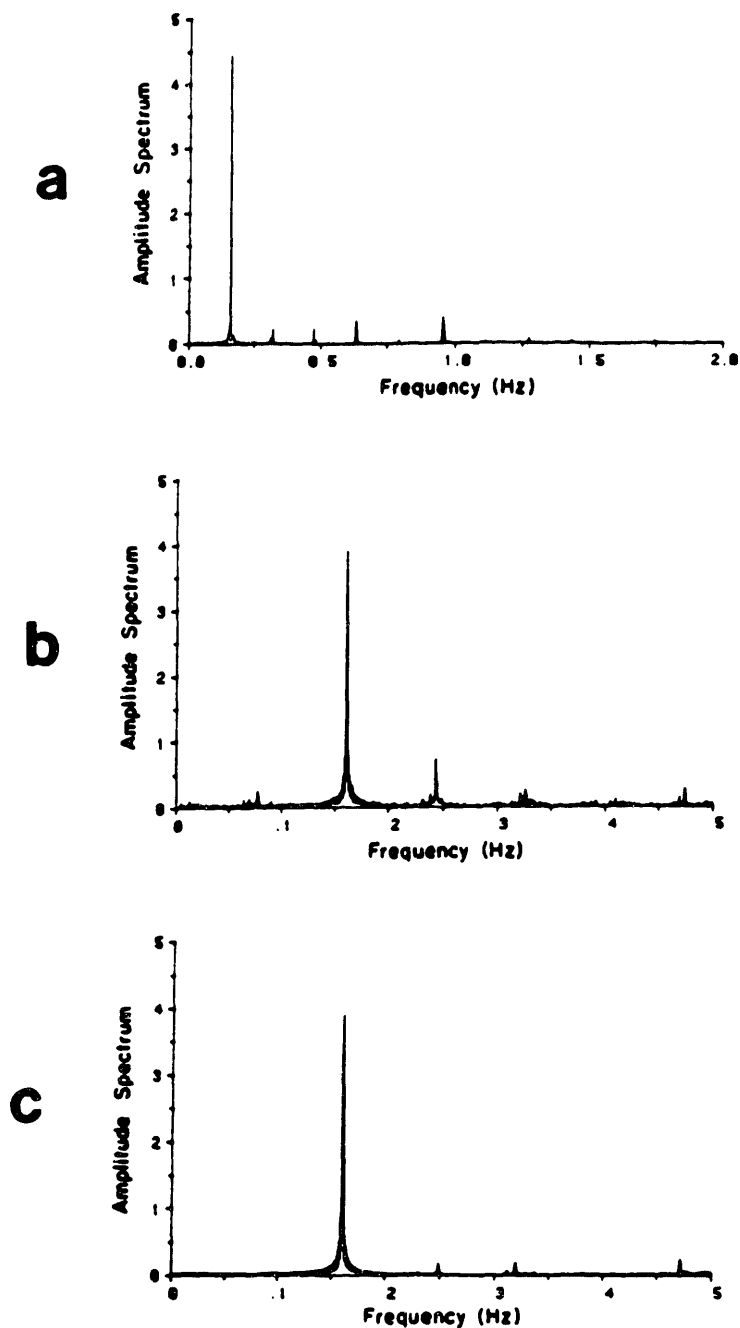


Figure 4.4. a. Heart rate amplitude spectrum computed analytically (using equation (4.9)) from data generated by an IPFM model driven by the input signal in equation (4.10). b. Amplitude spectrum of a sequences of samples taken from the instantaneous heart rate signal at 1.2 Hz, without first filtering the heart rate signal. Note the aliased peak at .248 Hz (see text). c. Amplitude spectrum of heart rate found using our algorithm. The sampling rate was the same as in (b).

physiologic interest in heart rate variability studies. The location of this aliased peak will obviously depend on the choice made for the sampling rate f_r .

The amplitude spectrum of the sequence of heart rate samples determined by our algorithm is shown in Figure 4.4c. Note the marked reduction in the aliased power at .248 Hz. For purposes of comparison, the sampling rate here was chosen to be the same as in Figure 4.4b (1.2 Hz). This choice is arbitrary, however, and again, in our studies f_r is in fact set to 2.8125 Hz. It is important to note that while our method in effect generates heart rate sample values of a piece-wise continuous signal that has undergone the necessary anti-aliasing filtering, the particular means by which we achieve the filtering operation is very efficient. Our method avoids the computational burden of actual digital convolution.

4.3.4 Performance Comparison Among Algorithms

In order to demonstrate that the spectrum of the heart rate signal constructed using our algorithm is relatively free of artifacts, we performed the same simulations as DeBoer et al [35] by implementing an IPFM model on a digital computer. We then computed heart rate spectra first using the three methods they presented and then using ours. Figure 4.5 shows the results of the simulation where the IPFM model input signal was again

$$s(t) = 1 + .3 \cos(2\pi f_m t) \quad (4.11)$$

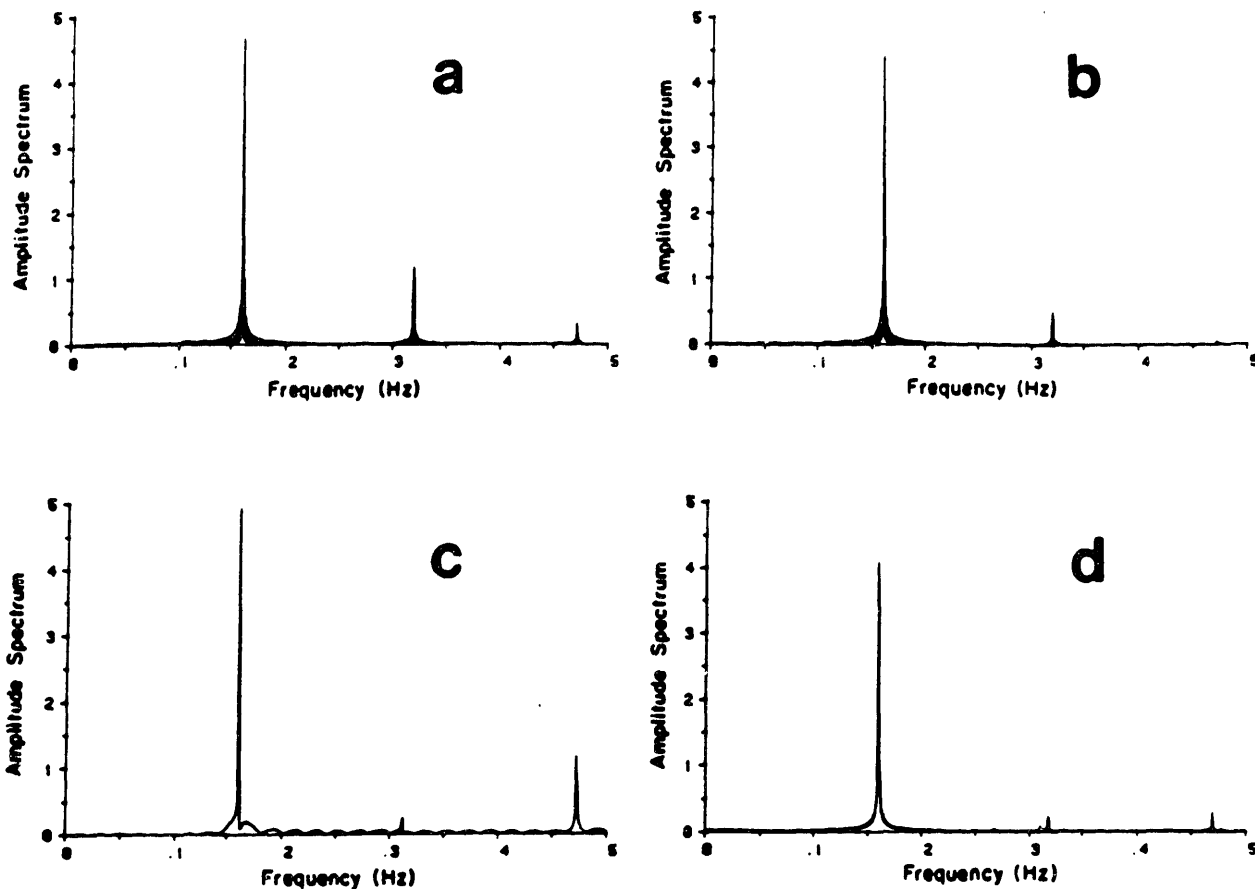


Figure 4.5. Amplitude spectra from four different methods used to analyze the RR interval sequence generated by an IPFM model, where the applied input signal was $s(t) = 1 + .3\cos(2\pi f_m t)$ with $f_m = .16$ Hz and the IPFM threshold set to 1.05 sec. a. Spectrum of intervals. b. Spectrum of inverse intervals. c. Spectrum of counts. d. Spectrum of heart rate samples found using our algorithm. All four spectra were computed using 1024 RR intervals. The frequency axis in (a) and (b) was normalized to units of cycles per second by multiplying by the mean repetition rate, as described in the text. For the heart rate spectrum computed using our algorithm (d), the sampling frequency f_s was 2.0 Hz. (Note that the sampling rate is the only difference between this and the spectrum shown in Figure 4.4c.)

with the modulation frequency $f_m = .16$ Hz and the IPFM threshold set to 1.05 sec.

All four spectra in Figure 4.5 show a large peak at the modulation frequency (.16 Hz). However, the spectrum of intervals (Figure 4.5a) and the spectrum of inverse intervals (Figure 4.5b) also contain a significant peak at the first harmonic (.32 Hz) and a smaller one at the second harmonic (.48 Hz) of the modulation frequency, that are virtually absent in the heart rate spectrum computed with our algorithm (Figure 4.5d). Similarly, there is a sideband artifact at .472 Hz (.952 - .48 Hz) in the spectrum of counts (Figure 4.5c) that is totally absent in the spectrum computed with our algorithm.

Figure 4.6 shows the results of a second simulation in which the input signal applied to the IPFM model was

$$s(t) = 1 + .3 \cos(2\pi f_1 t) + .3 \cos(2\pi f_2 t) \quad (4.12)$$

Here, again, the model's threshold was 1.05 sec. The two modulation frequencies f_1 and f_2 were .12 Hz and .16 Hz, respectively. These are the same parameters as those used by DeBoer et al in their second simulation [35]. All of the spectra for this case show large peaks at the two modulation frequencies. In addition, the spectrum of intervals (Figure 4.6a) and the spectrum of inverse intervals (Figure 4.6b) possess artifacts at harmonics of both modulation frequencies, and the spectrum of counts (Figure 4.6c) contains sideband artifacts at integer multiples of f_1 and f_2 away from the mean repetition rate of .952 Hz. Furthermore, the spectrum of inverse intervals (Figure 4.6b) contains a component at .04 Hz, the difference between the two modulation

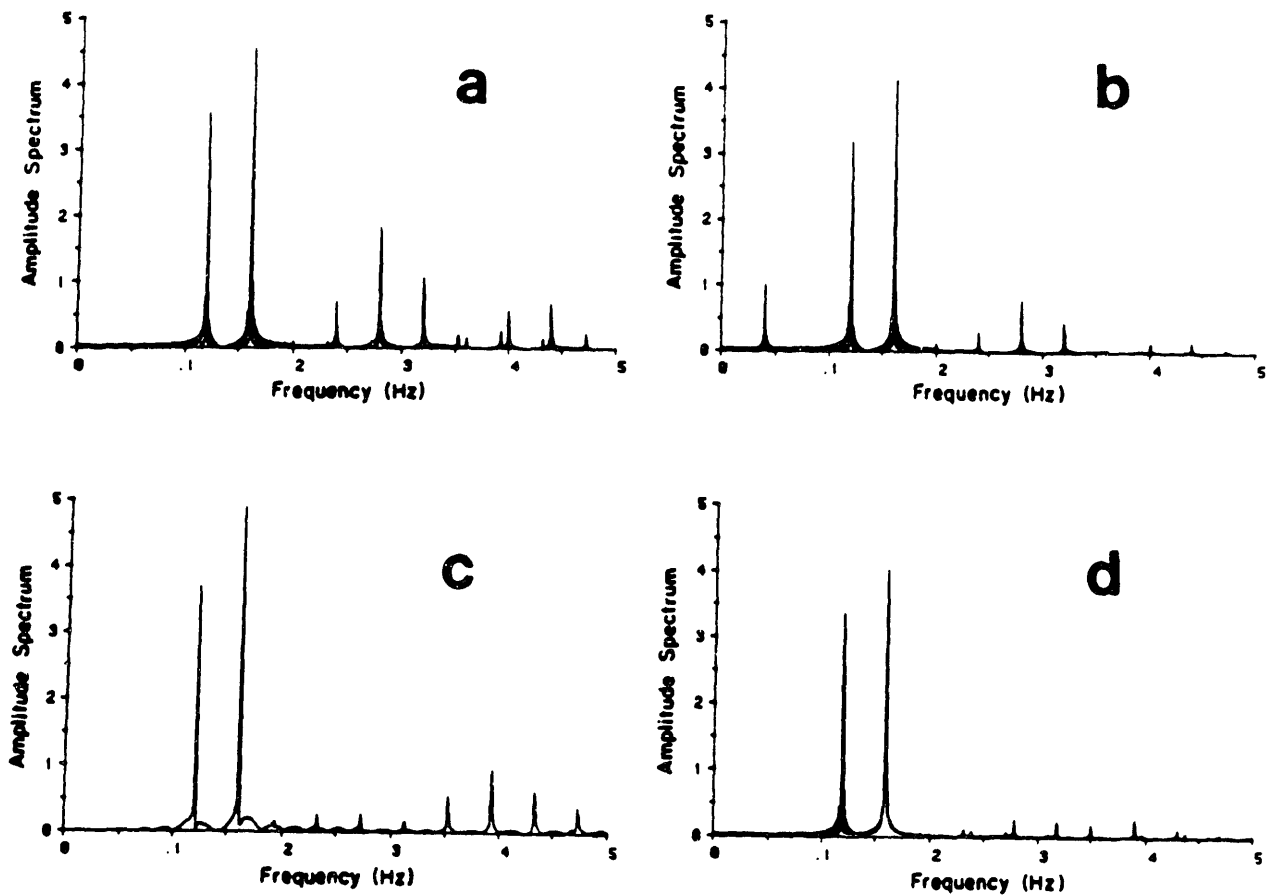


Figure 4.6. Same as Figure 4.5, but here the input signal applied to the IPFM model was $s(t) = 1 + .3\cos(2\pi f_1 t) + .3\cos(2\pi f_2 t)$, with $f_1 = .12$ Hz and $f_2 = .16$ Hz. The IPFM model threshold was again 1.05 sec.

frequencies. All of these artifacts are almost completely absent in the heart rate spectrum computed using our algorithm (Figure 4.6d).

The preponderance of influences that impinge on heart rate originate outside the heart, vary slowly compared to the heart rate, and are relatively insensitive to the actual timing of ventricular activations. For this reason, we feel that it seems more natural to characterize heart rate on a real time axis, rather than against "beat number." The IPFM model is consistent with this description since it lumps autonomic control and all other factors that affect heart rate into a single time-varying signal. Our algorithm provides a computationally simple definition of a heart rate signal, and as Figures 4.5 and 4.6 demonstrate, the spectrum of this signal very closely matches that of the IPFM model input signal. It is not surprising that the two spectra should be virtually identical, since by the very way we have defined the heart rate signal, were it applied to an IPFM model, the resulting sequence of RR intervals would be identical to that observed.

4.4 Spectral Estimation

An essential ingredient in the transfer function analysis employed in this thesis research is the estimation of power spectral densities. Both auto- and cross-spectra of and between the acquired hemodynamic signals must be found before transfer and coherence functions can be computed. There is often some confusion as to the use of the term "estimation" as opposed to "computation" of spectra. We speak of spectral estimates based on finite-length records of data. This does not mean that the energy content of the data record within a spectral bin is poorly defined or hard to determine. Rather, the uncertainty enters when we attempt to extrapolate frequency-domain information about a segment of data to the infinite-duration process from which the segment was extracted. By no means should the recipe for spectral estimation presented in this section be thought of as the only or the best technique available. Other algorithms abound and have been well reviewed [79]. The method we use, however, offers some convenient flexibility and imposes no a priori assumptions about the signals beyond stationarity, making it one of the most popular approaches employed, particularly in the analysis of stochastic data.

4.4.1 Autospectrum

We estimate the power spectral density function of a signal $x(t)$ using the Blackman-Tukey method [19]. In a nutshell, this technique involves first estimating the autocovariance function (ACVF) for the process, then applying an appropriate time-domain window, and finally taking the Fourier transform of the windowed autocovariance estimate.

The Wiener-Khinchin relation [139] states

$$S_{xx}(f) = \int_{-\infty}^{\infty} R_{xx}(\tau) e^{-j2\pi f\tau} d\tau. \quad (4.13)$$

Thus, the power spectrum $S_{xx}(f)$ of a process is the Fourier transform of the ACVF $R_{xx}(\tau)$, where, for a real-valued stationary process with mean \bar{x} ,

$$R_{xx}(\tau) = E[(x(t) - \bar{x})(x(t+\tau) - \bar{x})]. \quad (4.14)$$

If we knew $R_{xx}(\tau)$ exactly, then evaluation of the power spectrum would be trivial. The problem is we do not know $R_{xx}(\tau)$ exactly, and must estimate this function from 6-minute records of $x(t)$. In fact, our knowledge of $x(t)$ has been reduced to a mere 1024 samples, denoted $x(n)$, and the ACVF $R_{xx}(k)$ we wish to estimate is a function of the integer number of lags k , such that

$$R_{xx}(k) = E[(x(n) - \bar{x})(x(n+k) - \bar{x})]. \quad (4.15)$$

From now on, $x_o(n)$ will be used as a short hand notation for $x(n) - \bar{x}$.

If the process is ergodic, then the expectation value operator in equation (4.15) may be replaced by a time average. Thus, for $1-N \leq k \leq N-1$, the ACVF may be estimated by

$$\tilde{R}_{xx}(k) = \frac{1}{N-|k|} \sum_{n=0}^{N-|k|-1} x_o(n) x_o(n+|k|) \quad (4.16)$$

where the $N = 1024$ samples of $x(n)$ are indexed from $n = 0$ to $n = N-1$. Note that the ACVF estimate is based on progressively fewer terms as $|k|$ increases, causing the expected error, or variance, between $\tilde{R}_{xx}(k)$ and the true process ACVF $R_{xx}(k)$ to grow as $|k|$ approaches N . Jenkins and

Watts [70] have shown that for many processes, the mean square error ϵ of the ACVF estimate, where

$$\epsilon = \frac{1}{N} \sum_{k=0}^{N-1} [\tilde{R}_{XX}(k) - R_{XX}(k)]^2, \quad (4.17)$$

can be reduced by using the estimate

$$\tilde{R}'_{XX}(k) = \frac{1}{N} \sum_{n=0}^{N-|k|-1} x_o(n) x_o(n+|k|) \quad (4.18)$$

in place of $\tilde{R}_{XX}(k)$. While the variance of $\tilde{R}'_{XX}(k)$ remains small as $|k|$ increases, this estimator introduces bias error in the tails. It is easily seen that

$$\tilde{R}'_{XX}(k) = \frac{N-|k|}{N} \tilde{R}_{XX}(k). \quad (4.19)$$

The prefactor $(N-|k| / N)$ is simply the Bartlett window. As will be shown below, we apply a different window to the ACVF estimate, but like the Bartlett window, it too down-weights the tails of the ACVF, where the variance of the estimate is the greatest.

At this point, it is worthwhile to consider the computational burden involved in evaluating $\tilde{R}_{XX}(k)$. In order to compute $\tilde{R}_{XX}(k)$ for N different values of k using equation (4.16), one must perform roughly $N^2/2$ multiplications and as many additions. While this may be carried out quite rapidly on a 32-bit microprocessor-based computer when $N = 1024$, we sought a short cut in which the number of arithmetic operations would climb more slowly than a multiple of N^2 , should we be interested in analyzing longer records of data. Furthermore, since the transfer function analysis requires estimation of both input and output

autospectra as well as the cross-spectrum, it became desirable to find a method that provides intermediate results which are common to the evaluation of all three spectra.

We invoke a Fourier transform technique to evaluate $\tilde{R}_{xx}(k)$ efficiently. This must not be confused with the Fourier transform operation required to derive the spectral estimate from the ACVF. The steps taken to compute the ACVF estimate merely comprise a "trick" to avoid the computational burden of evaluating $\tilde{R}_{xx}(k)$ directly. The method is based on the relation,

$$\tilde{R}_{xx}(k) = \frac{1}{N-|k|} F_k^{-1}[X(q) \cdot X^*(q)] \quad (4.20)$$

where F is the discrete Fourier transform (DFT) operator, and $X(q)$ and $X^*(q)$ are the DFT of $x_0(n)$ and the DFT's complex conjugate, respectively. The DFT and inverse DFT definitions used here are:

$$Y(q) = F_q[y(n)] = \sum_{n=0}^{M-1} y(n) e^{-2\pi jqn/M} \quad (4.21a)$$

$$y(n) = F_n^{-1}[Y(q)] = \frac{1}{M} \sum_{q=0}^{M-1} Y(q) e^{2\pi jqn/M} \quad (4.21b)$$

where M represents the length of the DFT. I will now demonstrate that equations (4.16) and (4.20) are equivalent when the DFT length M is set equal to $2N$, and then consider the computational savings afforded by this procedure.

If $M > N$ and we set $x_0(n) = 0$ for $N \leq n \leq M-1$, then equation (4.21a) gives

$$X(q) = \sum_{n=0}^{N-1} x_o(n) e^{-2\pi jqn/M} \quad (4.22)$$

and

$$X^*(q) = \sum_{m=0}^{N-1} x_o^*(m) e^{2\pi jqm/M}. \quad (4.23)$$

Expansion of the right hand side of equation (4.20) using equations (4.21b), (4.22), and (4.23) yields

$$\begin{aligned} \frac{1}{N-|k|} F_k^{-1}[X(q) \cdot X^*(q)] &= \frac{1}{M(N-|k|)} \sum_{q=0}^{M-1} e^{2\pi jqk/M} \left[\sum_{n=0}^{N-1} x_o(n) e^{-2\pi jqn/M} \right] \\ &\quad \cdot \left[\sum_{m=0}^{N-1} x_o^*(m) e^{2\pi jqm/M} \right] \\ &= \frac{1}{M(N-|k|)} \sum_{n=0}^{N-1} \sum_{m=0}^{N-1} \sum_{q=0}^{M-1} x_o(n) x_o^*(m) e^{2\pi jq(k+m-n)/M} \end{aligned} \quad (4.24)$$

Note that

$$\sum_{q=0}^{M-1} e^{2\pi jq(k+m-n)/M} = \begin{cases} M & \text{for } |k+m-n| = 0, M, 2M, \dots \\ 0 & \text{otherwise.} \end{cases} \quad (4.25)$$

Now, if $M = 2N$, then $|k+m-n| < M$ since $1-N < k < N-1$, and m and n are bounded between 0 and $N-1$. Thus, the only non-zero terms in equation (4.24) are those for which $k+m-n = 0$, or equivalently, $n = m+k$. There will be exactly $N-|k|$ such terms, so equation (4.24) becomes

$$\frac{1}{N-|k|} F_k^{-1}[X(q) \cdot X^*(q)] = \frac{1}{N-|k|} \sum_{m=0}^{N-|k|-1} x_o^*(m) x_o(m+k). \quad (4.26)$$

For a real-valued process, $x_o^*(m) = x_o(m)$, so that the right hand sides of equations (4.16) and (4.26) are identical, thus proving equation

(4.20).

Note that if $M = N$ instead of $2N$, then non-zero terms will appear in equation (4.24) when either $k+m-n = 0$ or $|k+m-n| = N$. Equation (4.24) would then become

$$\frac{1}{N-|k|} F_k^{-1}[X(q) \cdot X^*(q)] = \frac{1}{N-|k|} \sum_{m=0}^{N-|k|-1} [x_o^*(m)x_o(m+k) + x_o^*(m)x_o(m+k-N) + x_o^*(m)x_o(m+k+N)], \quad (4.27)$$

where, again, $x_o(n) = 0$ for $n < 0$ or $n \geq N$. The additional terms in equation (4.27) not found in equation (4.26) represent shifted copies of the ACVF that are superimposed on the desired ACVF estimate. Thus, in order to correctly derive $\tilde{R}_{x_x}(k)$ for $-1023 \leq k \leq 1023$ from 1024 samples of $x_o(n)$ using this Fourier transform technique, $x_o(n)$ must first be padded with 1024 zeroes, extending its total length to 2048 samples, and then 2048-point DFTs should be employed.

The most computationally intensive steps in the implementation of equation (4.20) are 1) performing a $2N$ -point DFT on $x_o(n)$, 2) multiplying the $2N$ points of $X(q)$ by their complex conjugates, and 3) performing a $2N$ -point inverse DFT. The DFT and inverse DFT operations are made efficient through use of the Fast Fourier Transform (FFT) algorithm, which requires $M \cdot \log_2 M$ multiplications and an equal number of additions for an M point DFT. The total number of arithmetic operations required to derive the ACVF estimate is thus on the order of $2N \cdot (2 \log_2 N + 3)$ multiplications and $4N \cdot (\log_2 N + 1)$ additions. Clearly, for large N this method becomes substantially more efficient than direct computation of equation (4.16), which requires roughly N^2 arithmetic operations.

We now turn to the issue of windowing the ACVF estimate. As mentioned above, the unbiased ACVF estimate $\tilde{R}_{xx}(k)$ becomes progressively noisier in its tails. There is substantial estimator variance, however, even for $|k| \ll N$, since the evaluation of $\tilde{R}_{xx}(k)$ is based on a finite segment of data. Because the power spectral estimate $\tilde{S}_{xx}(q)$ is derived from $\tilde{R}_{xx}(k)$, estimation error present in the latter inevitably translates into a degradation of the former. In fact, even when a Bartlett window is applied to $\tilde{R}_{xx}(k)$ before taking its Fourier transform, if $x(n)$ is composed of samples of a colored noise process (i.e., filtered white noise), the anticipated error in each point of the resulting spectrum is as large as the value of the spectral estimate itself [102]. On the other hand, the frequency resolution (closest spacing between two independent points) of this spectral estimate is $3/2N$ times the sampling rate [70], or roughly .004 Hz when $N = 1024$ and the sampling rate is 2.8125 Hz. This is much finer than is necessary for even the most detailed description of autonomic response characteristics. By applying a window other than the Bartlett to the ACVF estimate, however, it is possible to trade off some of the excessive frequency resolution for a reduction in variance of the power spectral estimate.

The effect on the spectral estimate of applying a window $w(k)$ to the ACVF is easily ascertained. Since the spectral estimate $\tilde{S}_{xx}(q)$ is derived from the ACVF estimate $\tilde{R}_{xx}(k)$ using the relation

$$\tilde{S}_{xx}(q) = \Delta t F_q[\tilde{R}_{xx}(k) \cdot w(k)], \quad (4.28)$$

it is clear that

$$\tilde{S}_{xx}(q) = \tilde{S}'_{xx}(q) * W(q), \quad (4.29)$$

where $\tilde{S}'_{xx}(q) = \Delta t F_q[\tilde{R}_{xx}(k)]$, $W(q) = F_q[w(k)]$, and "*" is the convolution operator. (The factor of Δt , the sampling interval, is included so that $\tilde{S}_{xx}(q)$ has units of power density.) Equation (4.29) shows that the resulting spectral estimate may be thought of as the Fourier transform of the unwrapped ACVF estimate smeared by (or convolved with) the Fourier transform of the window function. The choice of the window shape is generally based on the degree of power leakage between spectral bins that may be tolerated. Most of the literature on this subject stresses the virtues of minimal power leakage, and the majority of the research effort in this area of signal processing has been spent in the design of windows whose frequency-domain representations include the narrowest possible main-lobe and the smallest possible side-lobes [102].

We, on the other hand, are more concerned with the degree of variance, or expected error, in the values of the spectral estimate due to the largely stochastic nature of the measured biologic processes. In order to achieve a reduction in this estimator variance, we are willing to tolerate a substantial degradation in the frequency resolution. A natural choice for the shape of the smoothing function is a Gaussian, or normal, distribution. A Gaussian window is elegant in that its Fourier transform is also a Gaussian, and is convenient in that its width may be regulated by varying a single parameter. The analytic form of such a window is

$$w(k) = e^{-\frac{(k\Delta t)^2}{2\sigma_t^2}} \quad (4.30)$$

for $1-N \leq k \leq N-1$, where σ_t is a free parameter that represents the half-width of the Gaussian in the time-domain. The Fourier transform of equation (4.30) gives the frequency-domain representation:

$$W(q) = \frac{1}{\sqrt{2\pi\sigma_f^2}} e^{-(q\Delta f)^2/2\sigma_f^2} \quad (4.31)$$

for $1-N \leq q \leq N-1$. Δf is the spacing between adjacent points in the spectral estimate and equals $f_s/2N$, where f_s is the sampling rate. Note that Δf is not the same as the frequency resolution defined above, since adjacent samples of the spectrum are not necessarily uncorrelated with each other, particularly when the spectral estimate has been intentionally smoothed. σ_t and σ_f are related to each other by $\sigma_t = 1/(2\pi\sigma_f)$. So, if we define a resolution factor r_s such that $\sigma_f = r_s\Delta f$, then $\sigma_t = N\Delta t/\pi r_s$. We typically choose $r_s = 4$. The width of the Gaussian in the frequency-domain, defined as twice its standard deviation σ_f , then works out to .011 Hz. Time- and frequency-domain representations of this window are shown in Figure 4.7. Note that with $r_s = 4$, $w(k)$ dies off long before $k = N$, so that truncation effects are minimal.

Inspection of equation (4.31) reveals that $W(q)$ is normalized such that

$$\sum_{q=-\infty}^{\infty} W(q)\Delta f \approx 1. \quad (4.32)$$

As Figure 4.7b shows, $W(q)$ at $q = N$ is so small that in practice we may approximate

$$\sum_{q=1-N}^{N-1} W(q)\Delta f \approx 1. \quad (4.33)$$

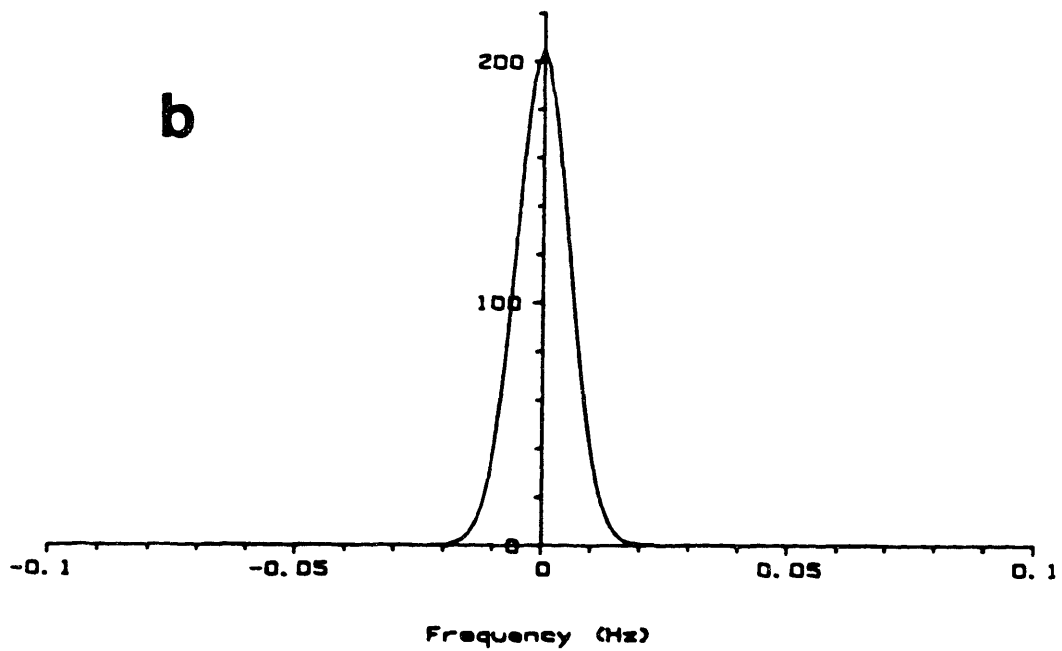
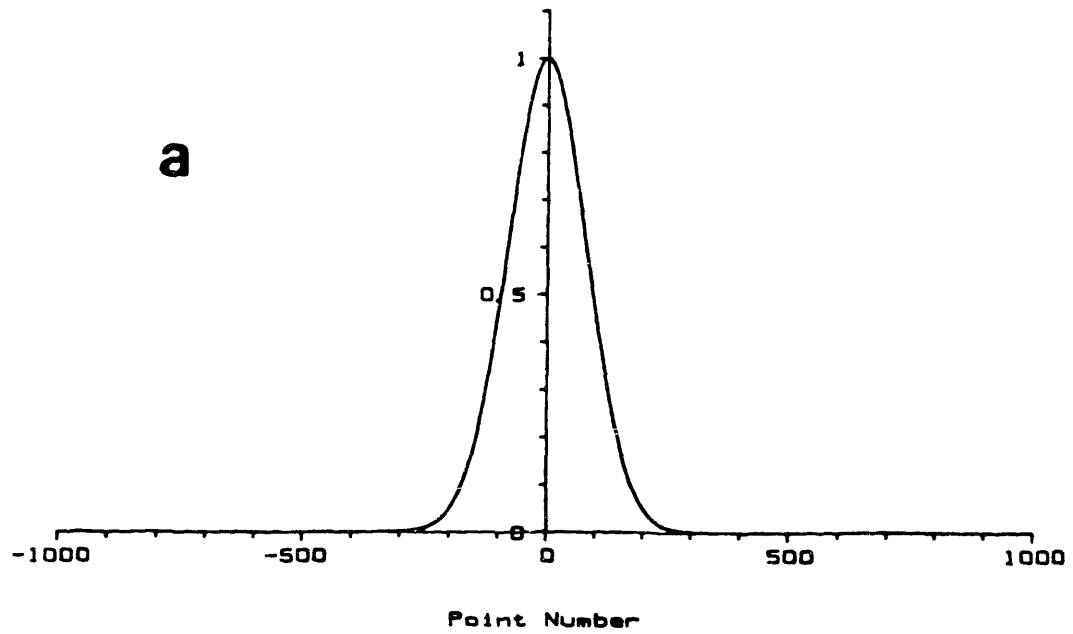


Figure 4.7. a. Time-domain representation of Gaussian window applied to ACVF estimate. b. Fourier transform of Gaussian window shown in (a), where the numbers on the frequency axis assume the sampling frequency $f_s = 2.8125$ Hz.

As a result of this normalization, application of this window does not alter the estimate of total power P_x in the signal $x_0(n)$, where P_x is found according to Parseval's theorem as

$$P_x = \frac{1}{N} \sum_{n=0}^{N-1} x_0^2(n) = \Delta f \sum_{q=0}^{2N-1} \tilde{S}_{xx}(q). \quad (4.34)$$

$\tilde{S}_{xx}(q)$ is a "biased" estimator, however, in the sense that peaks in the spectrum tend to be underestimated and valleys overestimated because of the smoothing operation. But of much greater importance, the smoothing greatly reduces the estimator error. Jenkins and Watts [70] have shown that the estimator variance is reduced by a factor Q , where

$$Q = \frac{1}{N\Delta t} \sum_{k=-N}^{N-1} w^2(k)\Delta t. \quad (4.35)$$

For the Gaussian window,

$$Q = \frac{1}{N\Delta t} \sum_{k=-N}^{N-1} e^{-(k\Delta t)^2/\sigma_t^2} \Delta t. \quad (4.36)$$

If we define $\alpha = \sigma_t / \sqrt{2}$, then equation (4.36) may be rewritten as

$$Q = \frac{\sqrt{2\pi\alpha^2}}{N\Delta t} \sum_{k=-N}^{N-1} \frac{1}{\sqrt{2\pi\alpha^2}} e^{-(k\Delta t)^2/2\alpha^2} \Delta t. \quad (4.37)$$

But,

$$\sum_{k=-N}^{N-1} \frac{1}{\sqrt{2\pi\alpha^2}} e^{-(k\Delta t)^2/2\alpha^2} \Delta t \approx 1 \quad (4.38)$$

since this is essentially the integral of a normalized Gaussian. So we get,

$$Q = \frac{\sqrt{2\pi\alpha^2}}{N\Delta t} = \frac{\sqrt{\pi}\sigma_t}{N\Delta t}. \quad (4.39)$$

Substituting $\sigma_t = N\Delta t/\pi r_s$ from above into equation (4.39) gives finally,

$$Q = \frac{1}{\sqrt{\pi r_s}} \quad (4.40)$$

and for $r_s = 4$, we find $Q = .141$. Multiplication of $\tilde{R}_x(k)$ by this window thus leads to a reduction in the variance of the spectral estimate to roughly 14% of its unwindowed level. Equivalently, the expected error, which equals the square root of the estimator variance, is reduced by roughly a factor of 2.7. It should be noted that the spectral estimate has a chi-square distribution about the true spectral density. The number of degrees of freedom μ in this chi-square distribution is inversely proportional to the variance ratio Q . In particular,

$$\mu = \frac{2}{Q} \quad (4.41)$$

so, for $r_s = 4$, $\mu \approx 14$.

The sequence of steps implemented in computing the spectral estimate is schematized in Figure 4.8. First, the D.C. component of $x(n)$ is removed to provide $x_0(n)$. $x_0(n)$ is then extended to twice its original length by zero-padding. Next, the $2N$ -point FFT of $x_0(n)$ is computed, as is its complex conjugate. $X(q)$ and $X^*(q)$ are then multiplied, and the inverse FFT of the result is computed. At this point, we have found the biased ACVF, and the inverse Bartlett window prefactor must be applied. The Gaussian window may then be applied to the unbiased ACVF. The FFT of the windowed ACVF is finally computed, and the result multiplied by Δt so that the spectrum will have units of power density. Note that $\tilde{S}_{xx}(q)$ represents the spectral estimate at a frequency $f = q\Delta f = qf_s/2N$.

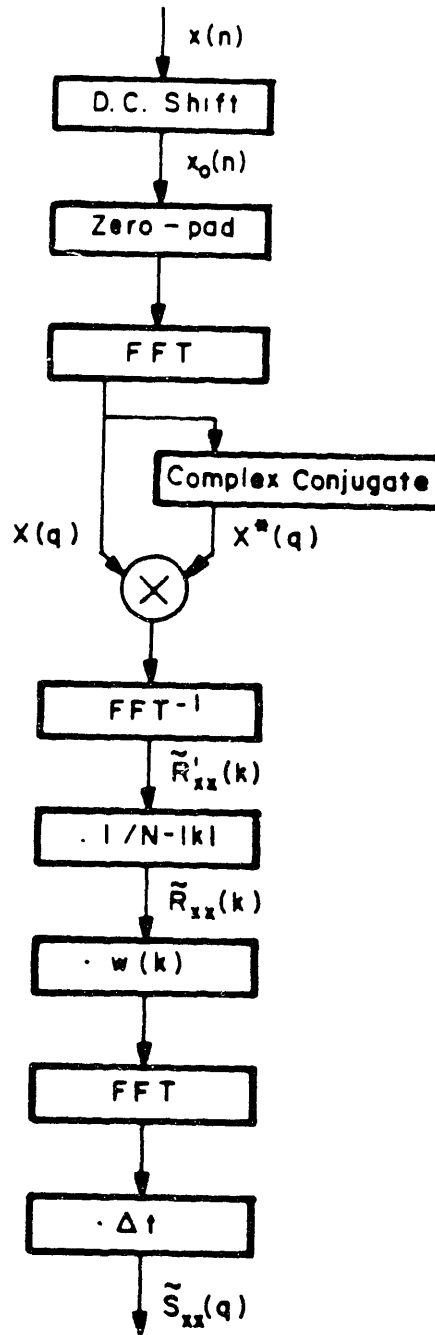


Figure 4.8. Flow chart of steps involved in power spectral estimation algorithm.

4.4.2 Cross-spectrum

In order to determine the transfer and coherence functions for an input/output signal pair $x(n)$ and $y(n)$, we must first obtain estimates not only of the autospectra $\tilde{S}_{xx}(q)$ and $\tilde{S}_{yy}(q)$, but of the cross-spectrum $\tilde{S}_{xy}(q)$ as well. The approach outlined above for estimation of the autospectrum is easily modified to enable computation of the cross-spectral estimate.

By analogy with equation (4.28), $\tilde{S}_{xy}(q)$ is derived from the estimate of the cross-covariance function (CCVF) $\tilde{R}_{xy}(k)$ according to the relation,

$$\tilde{S}_{xy}(q) = \Delta t F_q[\tilde{R}_{xy}(k) \cdot w(k)]. \quad (4.42)$$

The true CCVF is defined by

$$R_{xx}(k) = E[x_o(n) \cdot y_o(n+k)], \quad (4.43)$$

where $y_o(n) = y(n) - \bar{y}$. For ergodic processes, the expectation value may be found by time-averaging. The CCVF is thus estimated using a relation analogous to equation (4.16), except that the limits of the summation must be written explicitly for the two cases $k \geq 0$ and $k < 0$ since the arguments of $x_o(n)$ and $y_o(m)$ are not interchangeable:

$$\tilde{R}_{xy}(k) = \begin{cases} \frac{1}{N-|k|} \sum_{n=0}^{N-k-1} x_o(n) y_o(n+k) & \text{for } k \geq 0 \\ \frac{1}{N-|k|} \sum_{n=-k}^{N-1} x_o(n) y_o(n+k) & \text{for } k < 0. \end{cases} \quad (4.44)$$

A computationally more efficient FFT-based formula for evaluating $\tilde{R}_{xy}(k)$

can be derived using the same arguments that led to equation (4.20). Thus,

$$\tilde{R}_{xy}(k) = \frac{1}{N-|k|} F_k^{-1}[X^*(q) \cdot Y(q)], \quad (4.45)$$

where, again, $x_o(n)$ and $y_o(n)$ are first padded with N zeroes, $X^*(q) = F_q^*[x_o(n)]$, $Y(q) = F_q[y(n)]$, and the FFT and inverse FFT operations are performed on $2N$ -point data sequences. Once the unbiased CCVF estimate $\tilde{R}_{xy}(k)$ has been found, it can be multiplied by the same Gaussian window as that used for evaluation of the autospectral estimates. Finally, equation (4.42) is invoked to derive the cross-spectrum from the windowed CCVF estimate.

A couple of remarks are in order concerning the subtle differences between auto- and cross-spectral estimation. Note that while the ACVF estimate $\tilde{R}_{xx}(k)$ is symmetric in k , the CCVF $\tilde{R}_{xy}(k)$ is not. As a result, their Fourier transforms $\tilde{S}_{xx}(q)$ and $\tilde{S}_{xy}(q)$ differ in that the autospectrum is entirely real-valued and thus has zero phase, while the cross-spectrum is complex and can be decomposed into non-zero magnitude and phase components. This will become important in computing the system transfer function because the transfer phase will be exactly the same as the cross-spectral phase.

The lack of symmetry in the CCVF also brings about a potential difficulty in the estimation of the cross-spectrum. If the system contains any delay between input and output (as any causal system does), then $\tilde{R}_{xy}(k)$ will peak at some value of k other than $k = 0$. Jenkins and Watts [70] have shown that the operation of multiplying such a function by $w(n)$, which does peak at $k = 0$, results in the introduction of bias

error in the spectral estimate $\tilde{S}_{xy}(q)$. While they discuss compensation techniques to eliminate this bias error, they also acknowledge that the error is small unless the delay becomes comparable to $N\Delta t$. Although the autonomic nervous system certainly does contain delay elements, there is no evidence that any such delay exceeds 15 to 30 seconds. As the 6-minute data record length is more than an order of magnitude larger than these delays, we have chosen to ignore the small bias error incurred.

4.5 Transfer Function Estimation

The rationale behind and the meaning of the complex transfer function as a system characterization were discussed in Chapter 3. In addition, the coherence function was introduced as a measure of statistical significance of the transfer function estimate. In this section, we consider the computation of the transfer and coherence function estimates using the auto- and cross-spectral estimates described above. Derivation of the expected error in the transfer function estimate from the coherence function is then discussed. Finally, a method for pooling the transfer function estimates from all experiments within a study and for determining the expected error in the pooled estimate is presented.

4.5.1 Transfer and Coherence Functions

A relationship between the transfer function $H(q)$ and the cross-spectrum and input autospectrum was given in equation (3.25). This equation can be rewritten to provide a means for estimating the transfer function using estimates of the auto- and cross-spectra instead of their theoretical true values:

$$\tilde{H}(q) = \frac{\tilde{S}_{xy}(q)}{\tilde{S}_{xx}(q)} \quad (4.46)$$

where, as before, q refers to the frequency $q\Delta f$ which equals $qf_s/2N$. Equation (4.46) provides a robust estimate for $H(q)$, as it is easily shown [15] that $\tilde{H}(q)$ is unaffected by the addition of noise or other uncorrelated signals to the output $y(n)$. Transfer magnitude and phase components, $|\tilde{H}(q)|$ and $\tilde{H}_\theta(q)$, can be derived from the real part $\tilde{H}_R(q)$ and the imaginary part $\tilde{H}_I(q)$ of the complex function $\tilde{H}(q)$ as follows:

$$|\tilde{H}(q)| = \left[(\tilde{H}_R(q))^2 + (\tilde{H}_I(q))^2 \right]^{1/2} \quad (4.47a)$$

$$\tilde{H}_\theta(q) = \tan^{-1} \left[\frac{\tilde{H}_I(q)}{\tilde{H}_R(q)} \right]. \quad (4.47b)$$

As discussed earlier, only the numerator in equation (4.46) is complex, so that the transfer phase $\tilde{H}_\theta(q)$ is identical to the phase component of the cross-spectrum $\tilde{S}_{xy}(q)$.

Note that there is no guarantee that a transfer function estimated using equation (4.46) will correspond to a causal system. In fact, if the system under investigation contains a feedback path such that fluctuations in the output signal $y(n)$ influence the input $x(n)$, then the computed transfer function will clearly correspond to an acausal system. A useful check that the system at hand includes only a feedforward path is provided by computation of the impulse response function, found by taking the inverse Fourier transform of $\tilde{H}(q)$. A causal impulse response curve deviates significantly from zero only for $t > 0$.

The coherence function may similarly be evaluated using estimates of the input signal autospectrum $\tilde{S}_{xx}(q)$, the output autospectrum $\tilde{S}_{yy}(q)$, and the cross-spectrum $\tilde{S}_{xy}(q)$ according to the relation,

$$\tilde{\gamma}_{xy}^2(q) = \frac{|\tilde{S}_{xy}(q)|^2}{\tilde{S}_{xx}(q)\tilde{S}_{yy}(q)}. \quad (4.48)$$

The theoretical coherence $\gamma_{xy}^2(q)$ is real-valued and bounded between zero and unity. Its estimate $\tilde{\gamma}_{xy}^2(q)$ is also real-valued, and while it never falls below zero, it may attain values greater than unity due to estimator error. The estimation error in both $\tilde{H}(q)$ and $\tilde{\gamma}_{xy}^2(q)$ becomes particularly significant in spectral bands where the input power density $\tilde{S}_{xx}(q)$ is comparable to the level of unmeasurable noise. Thus, reiterating the point made in Chapter 3, successful transfer function analysis requires that the input excitation contain significant power over a broad range of frequencies.

Note that while $\tilde{S}_{xx}(q)$, $\tilde{S}_{yy}(q)$, and $\tilde{S}_{xy}(q)$ must all be found before $\tilde{\gamma}_{xy}^2(q)$ can be evaluated, the number of arithmetic operations required to compute the three spectral estimates is less than three times that required for a single such estimate. This is because the functions $X^*(q)$ and $Y(q)$, required for the computation of $\tilde{S}_{xy}(q)$ using equation (4.45), have already been found in computing $\tilde{S}_{xx}(q)$ and $\tilde{S}_{yy}(q)$.

4.5.2 Confidence Limits of Transfer Function

The coherence function provides a measure of believability in the transfer function estimate. The closer the coherence is to unity, the more appropriate is the linear model in describing the system at hand,

as the output fluctuations are more highly correlated with the input. Evaluation of the coherence function is most useful, however, in that it enables quantitative determination of confidence limits around the transfer function estimate, and of the estimator variance. The latter is particularly important in computing a group average from multiple experiments, as each datum should be weighted in inverse proportion to the variance of its estimate.

The approach presented here for determination of transfer function estimator variance is adapted from Jenkins and Watts [70], with some modification. They derived expressions for arbitrary-percentage confidence intervals for the magnitude and phase, based on the diagrams shown in Figure 4.9. In Figure 4.9a, the complex transfer function estimate is plotted as a vector on the $H_R - H_I$ plane, whose end-point is inscribed in a circular confidence zone. This circle is then approximated by a region that, when plotted in $H_\theta - |H|$ space as in Figure 4.9b, appears as a rectangle described by the pair of equations [70]:

$$|H(q)| = |\tilde{H}(q)| \cdot \left[1 \pm \left[\frac{-2}{\mu-2} f_{2, \mu-2}(1-\alpha) \left[\frac{1-\tilde{\gamma}_{xy}^2(q)}{\tilde{\gamma}_{xy}^2(q)} \right] \right]^{1/2} \right] \quad (4.49a)$$

$$H_\theta(q) = \tilde{H}_\theta(q) \pm \sin^{-1} \left[\frac{-2}{\mu-2} f_{2, \mu-2}(1-\alpha) \left[\frac{1-\tilde{\gamma}_{xy}^2(q)}{\tilde{\gamma}_{xy}^2(q)} \right] \right]^{1/2} . \quad (4.49b)$$

The rectangle represents the 100(1- α)% confidence region for $|H(q)|$ and $H_\theta(q)$. $f_{2, \mu-2}(1-\alpha)$ is a number such that

$$\text{Prob}\{F_{2, \mu-2} \leq f_{2, \mu-2}(1-\alpha)\} = 1-\alpha, \quad (4.50)$$

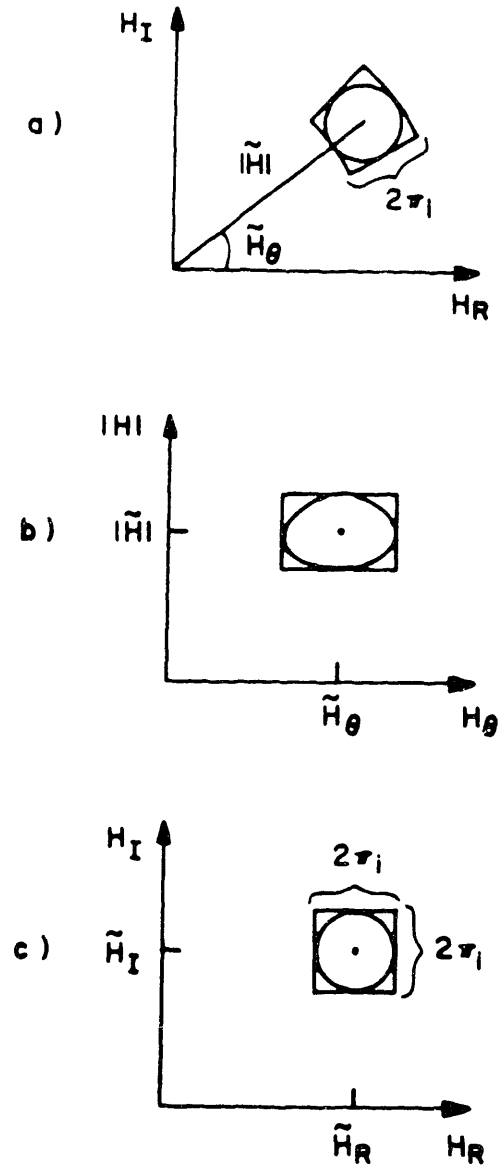


Figure 4.9. Complex transfer function estimate and associated confidence zone. a. Confidence zone shown as a circle in cartesian coordinate system and circumscribed by a piece of polar coordinate sector. b. Sector zone in (a) replotted in magnitude-phase space, showing distortion of original circular confidence region. c. Same as (a), but here the circular zone is circumscribed by a cartesian square whose width is identical to the sector length in (a).

where $F_{2, \mu-2}$ is the Fisher F distribution with 2 degrees of freedom in the numerator and $\mu-2$ degrees of freedom in the denominator. μ represents the number of degrees of freedom in the chi-square distribution that characterizes the spectral estimates, which equals 14, as discussed above. Note that the circular region in Figure 4.9a can also be approximated by the square zone shown in Figure 4.9c. The sides of this square depict the confidence intervals for $H_R(q)$ and $H_I(q)$, and the length of any edge is obviously identical to the confidence interval for $|H(q)|$, given by equation (4.49a).

We are interested in obtaining the variance of the distribution of the transfer function estimate about its theoretical true value. By plotting the width of the confidence interval as a function of α , one could map out the shape of the estimator distribution. While it is not quite a Gaussian distribution, approximating it as one is not terribly inaccurate. A good approximation of the estimator variance, therefore, is the square of half the confidence interval width for $\alpha = .32$, since a Gaussian distribution contains all but 32% of its area within one standard deviation from the mean. The variance $\pi^2(q)$ in the estimate of $H_R(q)$ or $H_I(q)$ is thus,

$$\pi^2(q) = |\tilde{H}(q)|^2 \cdot \left[\frac{2}{\mu-2} f_{2, \mu-2}(1-.32) \left[\frac{1-\tilde{\gamma}^2}{\tilde{\gamma}^2} \frac{xy(q)}{xy(q)} \right] \right], \quad (4.51)$$

and when $\mu = 14$, $f_{2, \mu-2}(1-.32) \approx 1.4$.

4.5.3 Pooling of Transfer Function Data

One of the ultimate goals of this thesis research is the develop-

ment of clinical tools to assess the integrity of an individual's autonomic nervous system. Such a tool will inevitably involve a comparison between transfer function data for the individual and some standard of normal. It therefore became important to devise a method whereby transfer function measurements made on a group of presumably normal experimental animals or human volunteer subjects could be coalesced so as to yield a group average. It is also useful to determine the standard error of the group mean so that pooled transfer function data for various physiologic states can be compared and tested for statistically significant differences.

The estimator variance $\pi^2(q)$ given by equation (4.51) characterizes the error inherent in the measurement of the transfer function due to the imperfection of the analysis technique. It is analogous to the ever-present error in the measurement of an individual's intelligence quotient (I.Q.) because the tests used are never culture-free. Unrelated to such measurement errors, however, is the presence of variability in the theoretical true measures across the population of presumed normals. Just as there is a range of I.Q.s among normal individuals, so too is there a range in autonomic transfer characteristics that comprise the norm. If any single empirical determination of a transfer function were intended to represent an estimate of the theoretical group average transfer function, the estimator variance would include two components. First, the empirical measure would deviate from the individual's true transfer function due to the measurement error, and second, the individual's transfer characteristics would deviate from the group mean due to the population variance.

In deriving a group-average transfer function estimate, the variance present in the individual estimates must be taken into account. At any given frequency, some of the individual transfer function estimates may have less variance, and are thus more reliable, than others due to a better level of input-output coherence. The group-mean should therefore be a weighted sum of the individual estimates, where more reliable terms are weighted more heavily. The maximum likelihood formulation [18] weights each estimate by the reciprocal of its variance. Thus,

$$\langle \tilde{H}_R(q) \rangle = \frac{\sum_{i=1}^K \left[\tilde{H}_{R_i}(q) / \sigma_i^2(q) \right]}{\sum_{i=1}^K \left[1 / \sigma_i^2(q) \right]} \quad (4.52a)$$

$$\langle \tilde{H}_I(q) \rangle = \frac{\sum_{i=1}^K \left[\tilde{H}_{I_i}(q) / \sigma_i^2(q) \right]}{\sum_{i=1}^K \left[1 / \sigma_i^2(q) \right]} \quad (4.52b)$$

where $\langle \tilde{H}_R(q) \rangle$ and $\langle \tilde{H}_I(q) \rangle$ are the real and imaginary part of the group-mean transfer function estimate, $\tilde{H}_{R_i}(q)$ and $\tilde{H}_{I_i}(q)$ are the real and imaginary parts of the i^{th} individual estimate, $\sigma_i^2(q)$ is the total (measurement plus population) variance in $\tilde{H}_{R_i}(q)$ and $\tilde{H}_{I_i}(q)$, and K is the number of measurements contributing to the average.

The key to this approach for pooling transfer function data is the evaluation of the individual estimator variances $\sigma_i^2(q)$. Note that this variance is assumed identical for the real and imaginary parts of the individual transfer estimate, as shown pictorially in Figure 4.10. In

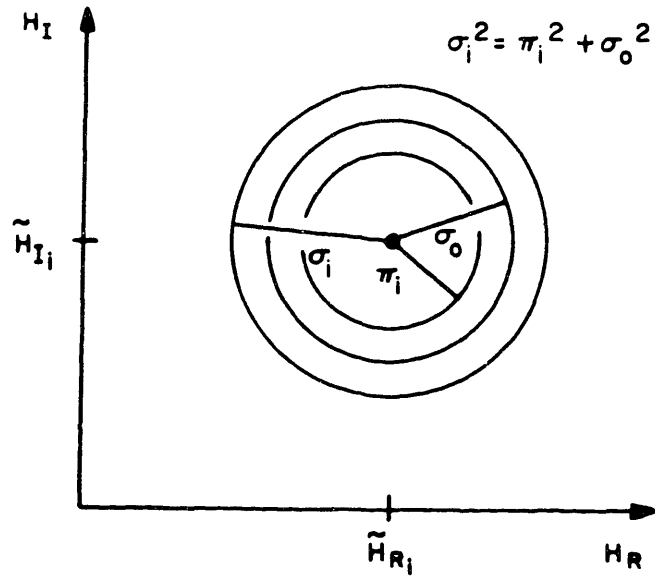


Figure 4.10. Confidence zone around the i^{th} individual transfer function measurement in estimating the group average. The inner ring of radius π_i represents the measurement error and the middle circle of radius σ_o denotes deviation among the population, so that the square of the outer ring radius σ_i^2 is the total estimator variance.

other words, iso-confidence zones around the transfer function estimate are assumed circular. The 68% confidence zone drawn in Figure 4.10 includes an inner circle that represents measurement error $\pi_1(q)$ and a second ring whose radius $\sigma_0(q)$ signifies the standard deviation in $|H(q)|$ among the population. Note that since these sources of error are assumed independent, the associated variances add, so that

$$\sigma_1^2(q) = \sigma_0^2(q) + \pi_1^2(q). \quad (4.53)$$

The derivation of the measurement variance $\pi_1^2(q)$ from the coherence function estimate was discussed above. The population variance $\sigma_0^2(q)$ may be estimated as

$$\sigma_0^2(q) = \frac{1}{N-1} \sum_{i=1}^K \left[|\tilde{H}_i(q)| - \langle |H(q)| \rangle \right]^2 \quad (4.54)$$

where $|\tilde{H}_i(q)|$ is the magnitude of the i^{th} transfer function estimate, and $\langle |H(q)| \rangle$ is the group average transfer magnitude. In fact, equation (4.54) overestimates $\sigma_0^2(q)$ somewhat since the $|\tilde{H}_i(q)|$'s contain measurement errors in addition to population differences. The group average transfer function's error bars ultimately computed will thus be conservatively wide.

Equation (4.54) presents us with a bit of a quandary, however. The population variance estimate $\sigma_0^2(q)$ is required to determine the individual estimator variances $\sigma_1^2(q)$, which in turn are used in deriving the group average transfer function, according to equations (4.52a) and (4.52b). But the group average transfer magnitude $\langle |H(q)| \rangle$ is required to find $\sigma_0^2(q)$, according to equation (4.54). Rather than invoke an iterative approach to resolve this dilemma, we temporarily estimate

$$\langle |H(q)| \rangle = \frac{1}{K} \sum_{i=1}^K |\tilde{H}_i(q)| \quad (4.55)$$

just for the purposes of equation (4.54). Making use of this substitution and some algebra, equation (4.54) may be rewritten,

$$\sigma_o^2(q) = \left[\frac{1}{N-1} \sum_{i=1}^K |\tilde{H}_i(q)|^2 \right] - \left[\frac{1}{N(N-1)} \left[\sum_{i=1}^K |\tilde{H}_i(q)| \right]^2 \right]. \quad (4.56)$$

Then the group average complex transfer function can be computed using equations (4.52a) and (4.52b), and decomposed into group average magnitude $\langle |\tilde{H}(q)| \rangle$ and phase $\langle \tilde{H}_\theta(q) \rangle$ components just as the individual estimates were in equations (4.47a) and (4.47b).

The standard error $\sigma_{\text{mag}}(q)$ of the group mean transfer magnitude estimate $\langle |\tilde{H}(q)| \rangle$ is

$$\sigma_{\text{mag}}(q) = \frac{1}{\left[\sum_{i=1}^K 1 / \sigma_i^2(q) \right]^{1/2}} \quad (4.57a)$$

and the standard error $\sigma_{\text{phase}}(q)$ of the group mean transfer phase $\langle \tilde{H}_\theta(q) \rangle$ is related to $\sigma_{\text{mag}}(q)$ trigonometrically as

$$\sigma_{\text{phase}}(q) = \sin^{-1} \left[\frac{\sigma_{\text{mag}}(q)}{\langle |\tilde{H}(q)| \rangle} \right]. \quad (4.57b)$$

The steps involved in deriving the group average transfer magnitude and phase functions and their standard errors are summarized in Figure 4.11. First, all the individual transfer function arrays $\tilde{H}_{R_i}(q)$ and $\tilde{H}_{I_i}(q)$ are read into core and the quantities $\sum |\tilde{H}_i(q)|$ and $\sum |\tilde{H}_i(q)|^2$ are computed, enabling the evaluation of the array $\sigma_o^2(q)$ using equation

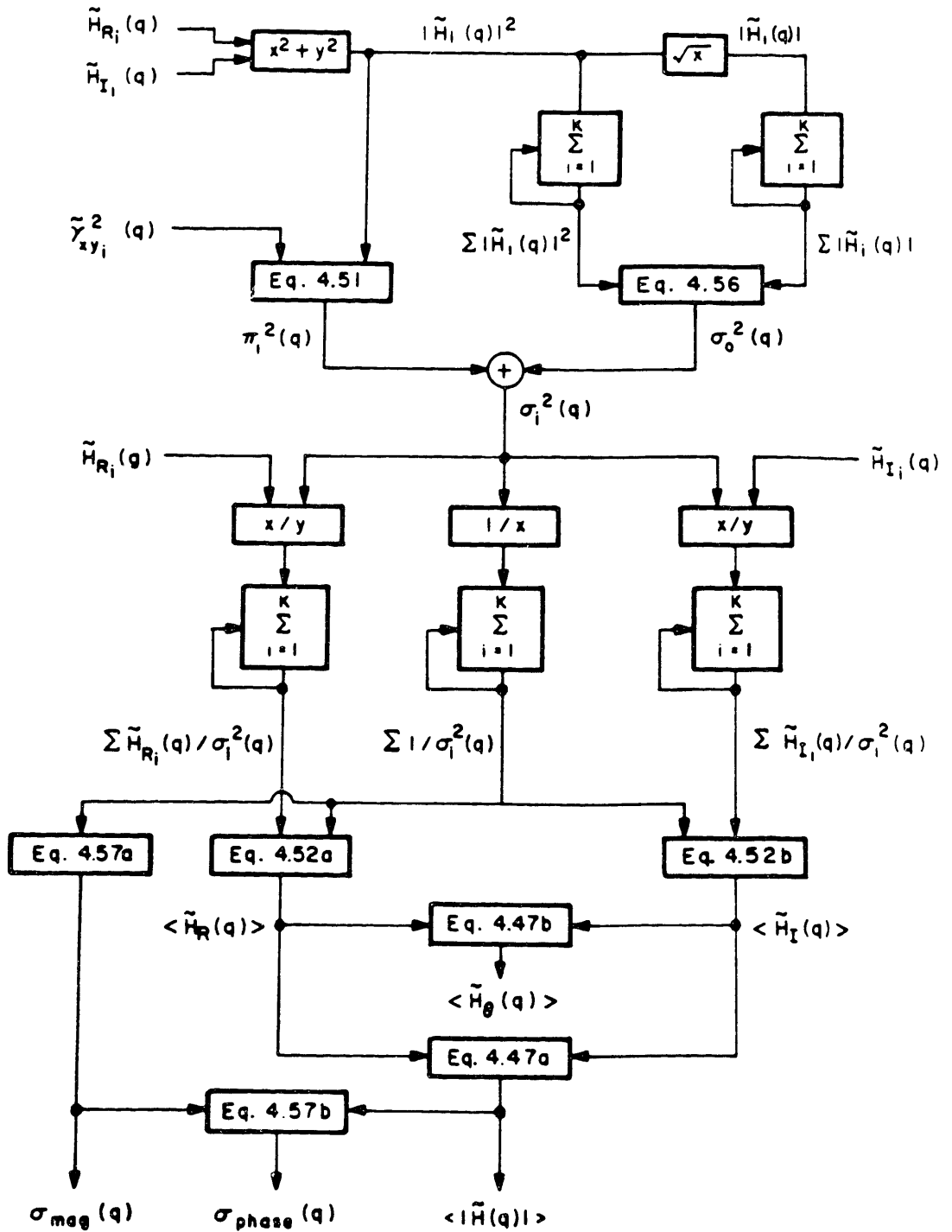


Figure 4.11. Flow chart outlining algorithm for determination of group-average transfer function magnitude and phase estimates and their corresponding expected errors.

(4.56). Next, the individual coherence functions $\tilde{\gamma}_{xy_i}^2(q)$ are read into core, and the transfer function estimator variances due to measurement error $\pi_i^2(q)$ are computed using equation (4.51). The arrays $\sigma_o^2(q)$ and $\pi_i^2(q)$ taken together yield $\sigma_i^2(q)$ according to equation (4.53), which allows for the determination of the quantities $\sum \left[\tilde{H}_{R_i}(q) / \sigma_i^2(q) \right]$, $\sum \left[\tilde{H}_{I_i}(q) / \sigma_i^2(q) \right]$, and $\sum [1 / \sigma_i^2(q)]$. These quantities are used in the numerators and denominators of equations (4.52a), (4.52b), and (4.57a) to find $\langle \tilde{H}_R(q) \rangle$, $\langle \tilde{H}_I(q) \rangle$, and $\sigma_{mag}(q)$. $\sigma_{phase}(q)$ is then found using equation (4.57b), and the group average transfer magnitude and phase components, $\langle |\tilde{H}(q)| \rangle$ and $\langle \tilde{H}_\theta(q) \rangle$, are derived from $\langle \tilde{H}_R(q) \rangle$ and $\langle \tilde{H}_I(q) \rangle$ using equations (4.47a) and (4.47b). In chapters 5, 6, and 7, when group average transfer magnitude and phase estimates are plotted with error bars, the errors represent the quantities $\sigma_{mag}(q)$ and $\sigma_{phase}(q)$.

Chapter 5: Study of the Response of the Sino-atrial Node*

5.1 Introduction

In this chapter, we consider the transfer characteristics of one particular functional block within the cardiovascular regulatory system - the sino-atrial (SA) node. Referring to the model presented in Chapter 2, we recall that the SA node serves as the clock, or pacemaker, of the heart. Since the instantaneous cardiac output is the product of heart rate and stroke volume, changes in heart rate strongly influence the hemodynamic variables, arterial pressure and flow. As shown in Figure 2.5, the SA node is innervated by both sympathetic and vagal fibers. While each of these two neural systems antagonizes the other's influence on nodal function [117], their effects are not simply additive or independent of each other. Samaan [119] showed that with sufficient vagal activity, sympathetic influences on heart rate can be abrogated regardless of the level of sympathetic tone. Levy and coworkers [51,82,90,92] have proposed mechanisms on the cellular level to account for these observations.

The instantaneous level of sympathetic or vagal activity relates to the rate at which these nerve fibers release vesicles of their respective neurotransmitter into the synapses with nodal cells. This, in turn, depends on the frequency of action potentials that are conducted along the nerve axons. Sympathetic and vagal "tone" thus refers to the

* Much of the material in this chapter was presented at the 1986 conference on Computers in Cardiology and published in the conference proceedings[17].

instantaneous neural spike rate in these fibers. Warner and Cox [136] presented a 2-part mathematical model to describe the relations between each, vagal and sympathetic tone, and the heart rate. Warner and Russell [137] took this work a step further by integrating the two halves of the model to account for sympathetic-parasympathetic interactions. These workers tested their model by comparing its predictions of heart rate changes with data from experiments on dogs in which the vagus and cardiac sympathetic nerves were stimulated with various fixed-rate pulse trains.

We, on the other hand, became interested in characterizing the SA nodal rate response to fluctuations in sympathetic and parasympathetic tone. Although Warner and Russell did not specifically investigate the predictions of their model with regard to broad-band fluctuations in autonomic tone, the data presented in this chapter provide an experimental basis for testing this aspect of their model. Previous attempts at characterizing the frequency response of the SA node are limited to the work by Penaz [105] and by Chess and Calaresu[24]. These investigators determined describing functions relating the magnitude and phase of heart rate changes to the rate at which stimulatory pulses, applied to the vagus nerve in either rabbits or cats, were sinusoidally frequency-modulated. By contrast, we compute transfer function estimates of the canine SA nodal rate response by applying to the vagus and sympathetic nerves pulse trains whose frequency is modulated by broad-band noise. As discussed in Chapter 3, this efficient approach enables us to characterize the system around multiple operating points (i.e., mean stimulatory rates) in a single experimental preparation.

5.2 Methods

Two sets of experiments were performed each using eight healthy adult mongrel dogs anesthetized with sodium pentobarbital (30 mg/kg). The apparatus employed in these experiments and the relevant anatomy is schematized in Figure 5.1. In the first group of experiments, we examined the heart rate response to fluctuations imposed in vagal tone. So as not to confound the measurement of the SA nodal response to exogenously applied neural stimulation, all endogenous neural influences on heart rate were interrupted. Endogenous sympathetic activity was eliminated by injecting the animal with reserpine (0.3 mg/kg IM) 24 hours prior to the experiment to deplete stores of catecholamines including norepinephrine. Conduction of endogenous parasympathetic activity was blocked in the left vagus by sectioning the nerve, and in the right vagus by infiltrating the nerve with lidocaine HCl at the level of the base of the skull. Since the stimulatory pulse train was applied to the right vagus, we avoided sectioning this nerve so as to preserve blood vessels that pervade the bundle and maintain its viability. The electrode pair was thus applied across the nerve several centimeters caudal to the level of lidocaine blockade. To prevent the vagus nerve from drying out, the nerve bundle and electrodes were immersed in a pool of mineral oil poured between a skin flap and the trachea on the right side of the neck.

The second series of experiments was designed to study the SA nodal response to fluctuations in sympathetic activity using a similar protocol. In these experiments, vagal activity was blocked with atropine (.1mg/kg) and endogenous sympathetic activity was interrupted by

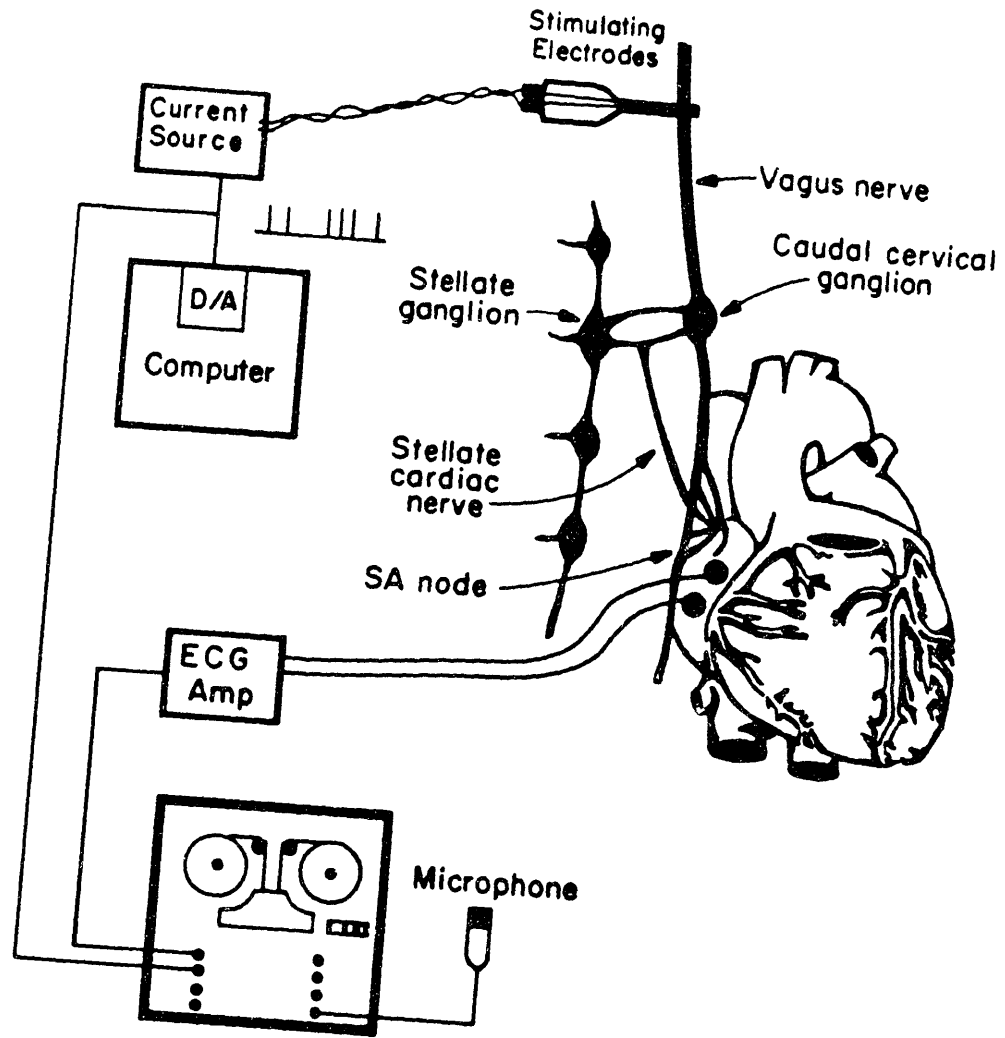


Figure 5.1. Apparatus used in vagal and sympathetic stimulation experiments. Also shown is the relevant canine anatomy, including the right vagus nerve and stellate ganglion.

severing all nerve fibers entering the two stellate ganglia from the spinal cord. Stimulating electrodes were then applied to either the decentralized right stellate ganglion or the cardiac stellate nerve.

In order to excite the system under study with a broad-band input signal, the waveform applied to the stimulatory electrodes in both sets of experiments was a train of 2 msec wide supramaximal* current pulses whose frequency varied about some mean rate in proportion to a Gaussian white noise (GWN) signal. The timing of these pulses was controlled by a Digital Equipment Corp. PDP-11/23 based computer, programmed as follows. Samples of a Gaussian white noise process were generated by summing 12 independent uniformly-distributed random numbers. To confine the GWN signal energy to the spectral band of interest, this sequence of numbers was digitally processed with a 101-point low-pass filter whose band edge was typically set to 0.7 Hz, such that the resulting values represented a 5 Hz sampling of filtered Gaussian noise. Linear interpolation between these points provided samples, at a rate of 500 Hz, of a band-limited GWN signal $f(n)$ signifying the instantaneous pulse rate. This signal was then used as the input to an integral-pulse-frequency-modulation (IPFM) model in that at each tick of the 500 Hz clock, the reciprocal of $f(n)$ (representing the instantaneous inter-pulse interval) was compared to the time t since the last output pulse. Whenever t exceeded $1/f(n)$, the computer output a pulse on its digital-to-analog (D/A) converter and reset t to zero. The resulting output waveform was thus a Gaussian white noise frequency-modulated (GWNFM) pulse train.

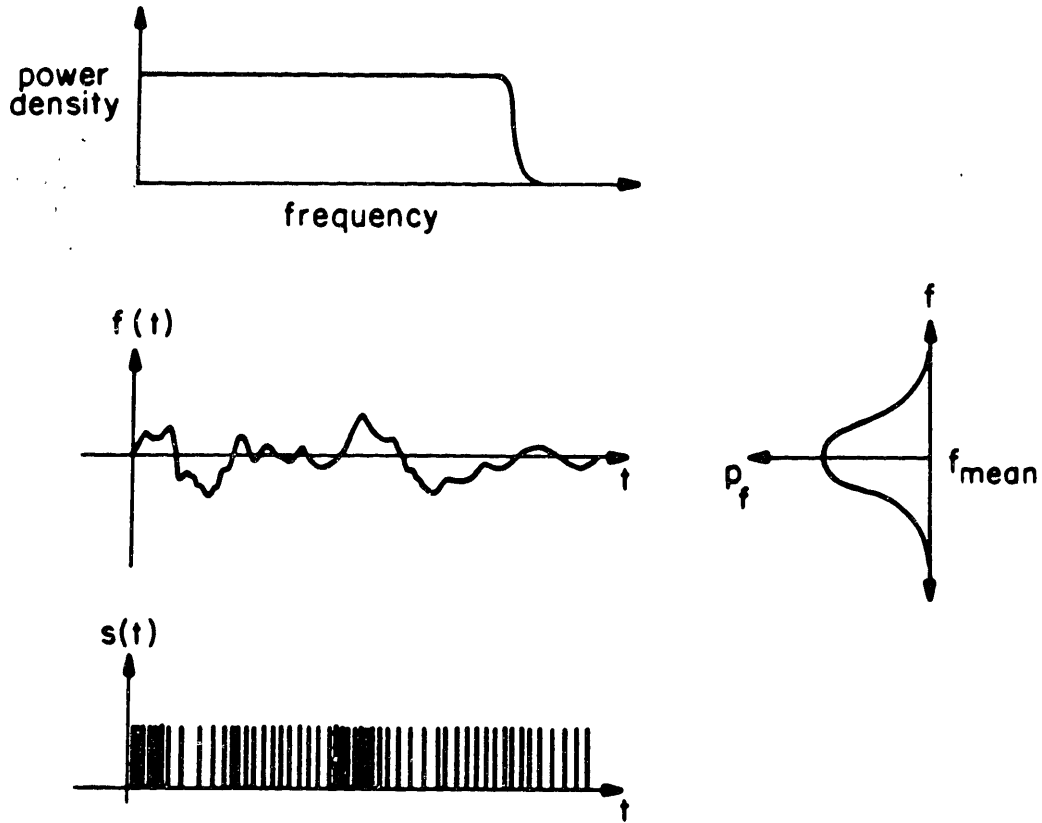
* By "supramaximal" I mean of sufficient magnitude to depolarize all excitable nerve fibers within the bundle (generally about 2 ma).

Stylized representations of the band-limited GWN signal, its theoretical power spectrum and probability distribution, and the corresponding GWNFM pulse train are shown in Figure 5.2.

Importantly, the mean f_{mean} and variance σ_f of the GWN modulator signal was specified for each experimental run. In the vagal stimulation studies, test runs were performed with f_{mean} set to 1, 2, 4, and 6 Hz. By contrast, the mean sympathetic stimulation rates employed were .5, .75, 1.0, 1.25, and 1.5 Hz, as little additional cardiac acceleration is realized beyond sympathetic rates of 1.5 Hz. σ_f was generally set to roughly $f_{\text{mean}}/4$. (Note that when f_{mean} was set below 1 Hz, as in many of the sympathetic stimulation runs, the band-pass edge for the GWN digital filter was, of necessity, reduced from .7 Hz to $f_{\text{mean}} - \sigma_f$.)

Epicardial electrodes were installed on the right atrium so that an atrial electrogram could be obtained. Atrial activations were assumed linked to events of SA nodal firing, with negligible delay. This electrogram, as well as the pulse train produced by the computer, were recorded for off-line analysis. The output of the computer could not, however, be connected directly to the stimulatory electrodes since the D/A converter produces voltage spikes whose current level is small and uncontrolled. We therefore designed and built a voltage-dependent current source to provide current spikes electrically isolated from the computer and recording equipment. A schematic of this circuit is shown in Figure 5.3. The voltage signal from the computer, after attenuation, appears at the input to an Analog Devices model 289 isolation amplifier. The output of this device is then applied to the non-inverting input of a TL062 op-amp coupled to a high-voltage MOSFET (IVN6000). The feedback

Gaussian White Noise (GWN)



Gaussian White Noise
Frequency Modulation (GWNFM)

Figure 5.2. Theoretical power spectrum, time series, and probability distribution of band-limited Gaussian white noise, and corresponding frequency-modulated pulse train.

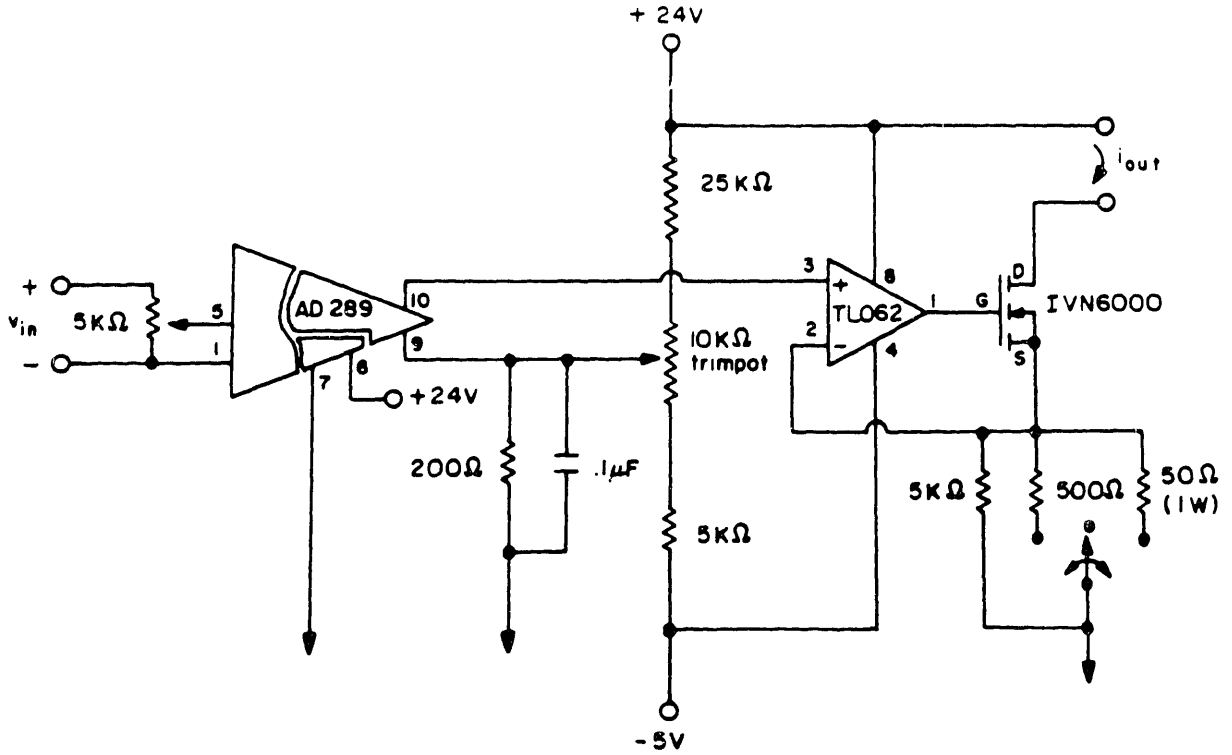


Figure 5.3. Schematic drawing of voltage-to-current converter circuit.

configuration between the op-amp and MOSFET is designed such that the MOSFET draws just enough current from drain to source to maintain the voltage across the source-to-ground resistance the same as that applied to the op-amp. The resistance between the MOSFET source and isolated ground is chosen by the user as 50, 500, or 5k Ohms, allowing for three decades of range in MOSFET drain current. The regulated current signal applied to the stimulatory electrodes is thus taken from the circuit's 24 volt power supply and returned to the drain terminal of the MOSFET.

Data from these experiments was analyzed as outlined in Chapter 4. The input signal $x(n)$ was taken to be the instantaneous rate of neural stimulation, and the output $y(n)$ was the instantaneous SA nodal firing rate. These signals were derived from the recorded pulse train and atrial electrogram signals respectively, using the tachometer algorithm presented in Section 4.3. In the vagal stimulation studies, sampling of the recorded signals at 360 Hz was adequate to resolve changes in the nodal firing rate. In the sympathetic stimulation experiments, however, the induced fluctuations in nodal rate were so small that a sampling frequency of 720 Hz was required. (See Section 4.2.) Six-minute records consisting of 1024 samples of the instantaneous rate signals were used to compute transfer function estimates and corresponding coherence functions for each of the mean stimulatory frequencies employed. Results from within each of the two sets of experiments were pooled to provide group average transfer magnitude and phase estimates and confidence intervals, as described in Section 4.5.

5.3 Results

5.3.1 Vagal Stimulation

Figure 5.4 is a plot of mean SA nodal rate as a function of mean vagal stimulation frequency from one representative experiment. This shows the D.C. response of the SA node to vagal drive, but communicates no information regarding nodal response to fluctuations in vagal tone. These results are similar to those presented by Rosenblueth and Simeone [117], and demonstrate the strong cardiac decelerating effect of vagal drive that does not start to plateau until the heart rate falls below half its resting level.

Data derived from one 6-minute experimental run are displayed in Figures 5.5 and 5.6. Figures 5.5a and b show time series of the instantaneous neural stimulatory rate and SA nodal rate, respectively, when a GWNFM pulse train with $f_{\text{mean}} = 4$ Hz was applied to the vagus nerve. Note that the neural spike rate fluctuates noisily around its mean (240/min), and that this induces wide swings in nodal rate. Autospectral density estimates for these two signals are shown in Figures 5.5c and d. While the vagal rate signal possesses substantial power density out to 0.7 Hz (the GWN generator filter edge), the resulting SA nodal rate fluctuations are clearly less spectrally broad.

Estimates of the transfer function magnitude and phase, the coherence function, and the impulse response for this experimental test of the SA node are shown in Figures 5.6a, b, c, and d. These estimates were computed from the time series of Figure 5.5, using the techniques described in Section 4.5. Figure 5.6c indicates that fluctuations in

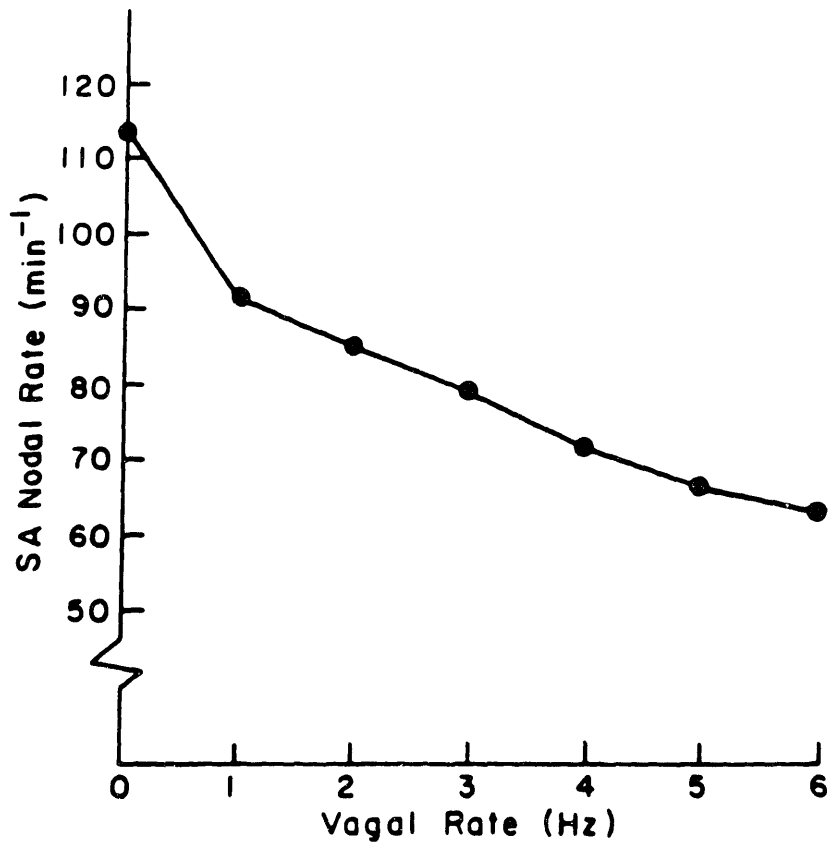


Figure 5.4. Mean SA nodal rate vs vagal stimulation frequency.

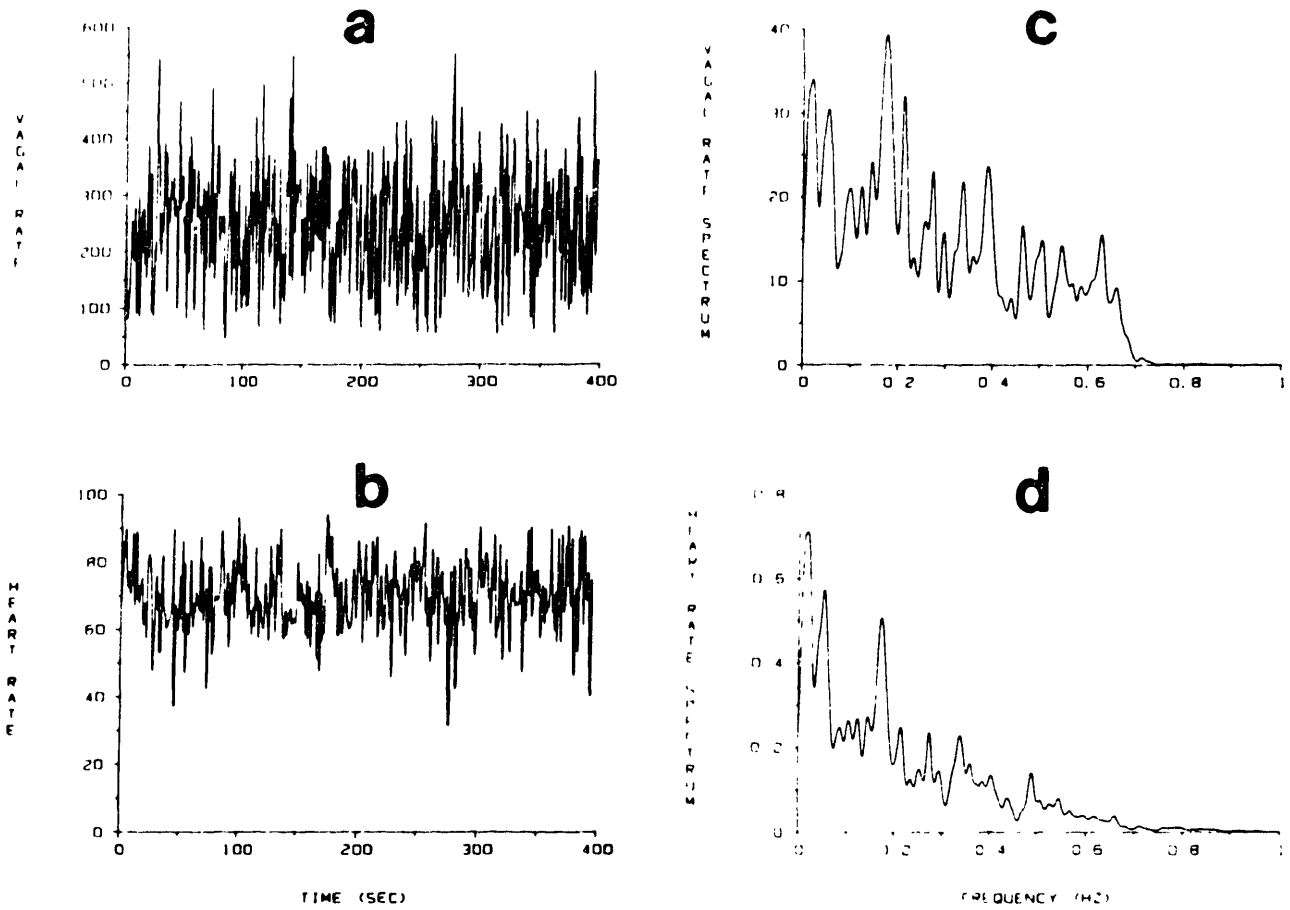


Figure 5.5. Derived instantaneous rate signals from one experimental run of GWNFM vagal stimulation. a. Vagal rate signal. b. SA nodal rate signal. c. Power spectrum of (a). d. Power spectrum of (b).

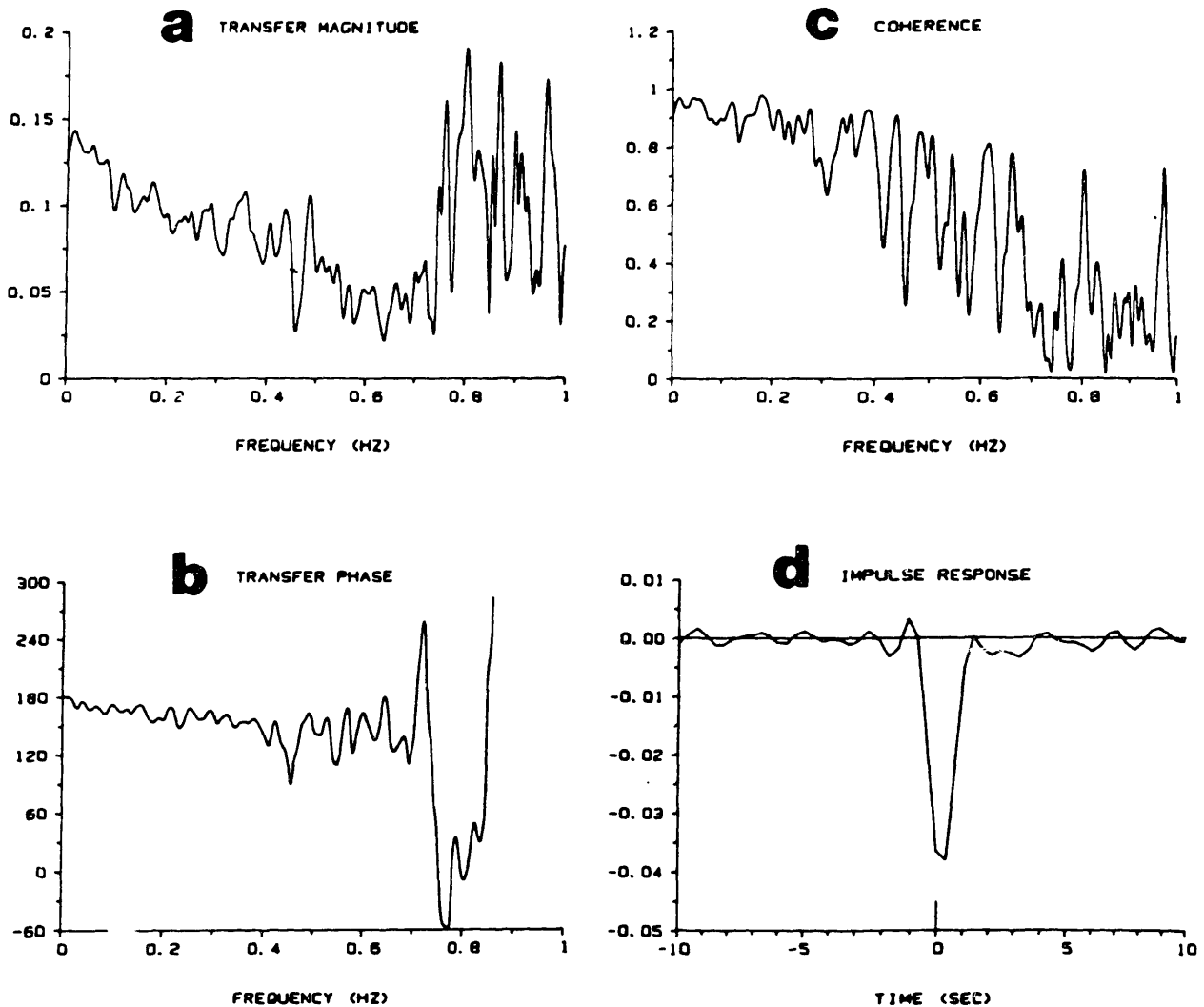
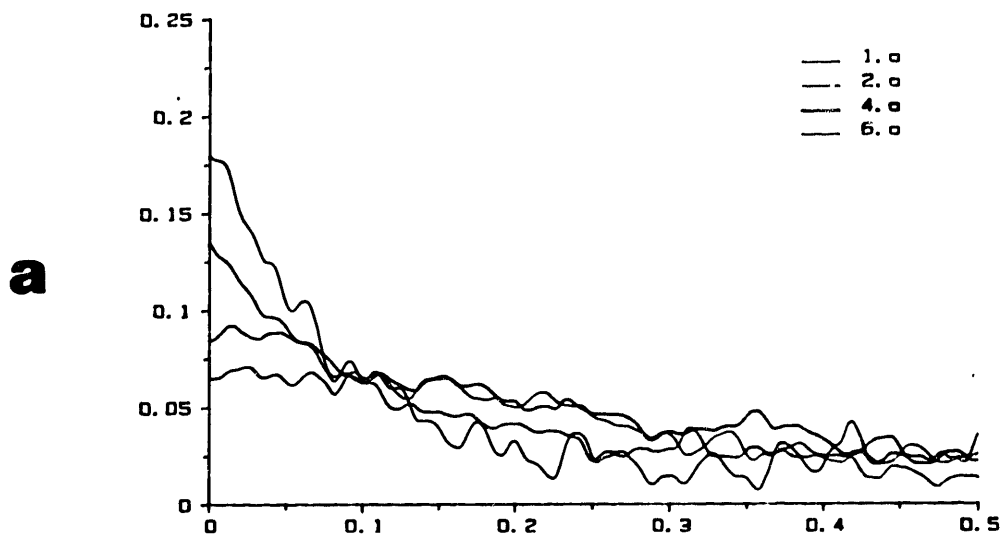


Figure 5.6. Transfer function magnitude (a) and phase (b) estimates, coherence function (c), and impulse response (d) derived from instantaneous rate signals shown in Figure 5.5. Note fall in coherence and noise in magnitude and phase estimates beyond input signal band-edge (0.7 Hz). The significance of nonzero values in the impulse response curve at slightly negative lags is discussed in the text.

the SA nodal rate are indeed quite coherently related to those in vagal tone between D.C. and 0.7 Hz. This frequency range of coherent response, again, relates to the spectral band of input excitation. Of course, even if the spectral content of the GWN neural rate modulator signal extended beyond 0.7 Hz, fluctuations in nodal rate within this spectral region would be meaningless, since the mean SA nodal rate itself is not much higher than this frequency. Within the coherent regime, the transfer magnitude plot shows a slow decline with frequency, reflecting the low-pass filter nature of the SA nodal response to vagal perturbations. The phase plot displays increasing phase delay with frequency, also consistent with low-pass filter behavior. Note that the phase attains a value near 180 degrees at D.C., which reflects the fact that increasing vagal excitation is accompanied by a decrease in SA nodal rate. The impulse response confirms the inverse relation between vagal stimulation rate and heart rate, in that it lies almost entirely below zero. It also reflects the lack of delay in SA nodal response to vagal excitation. In fact, the impulse response curve shown here attains a significantly nonzero value even for the first negative lag point, suggesting a lack of causality. This is an artifact that relates to truncation of the complex transfer function performed before taking its inverse Fourier transform to avoid inclusion of the non-coherent high frequency region of the response. The effect of such truncation is to smear the impulse response curve slightly.

The group-average transfer function magnitude and phase estimates for the vagal stimulation experiments are shown in Figures 5.7 and 5.8 respectively. These pooled estimates characterize the SA nodal fre-

4. a 1. a 2. a 6. a - Magnitude



4. a 1. a 2. a 6. a - Magnitude +/- Standard Error

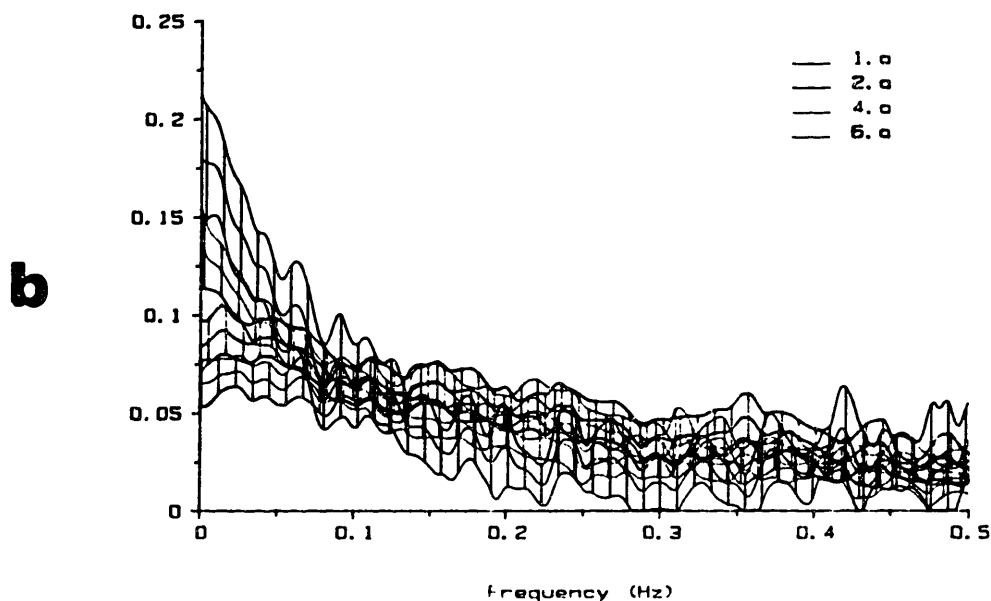


Figure 5.7. Group-average transfer magnitude functions for GWNFM vagal excitation at mean rates of 1, 2, 4, and 6 Hz. The label prefix refers to the mean frequency for that curve. a. Group-average estimates shown without error bars. b. Confidence zones included, indicating the standard error of the mean estimates.

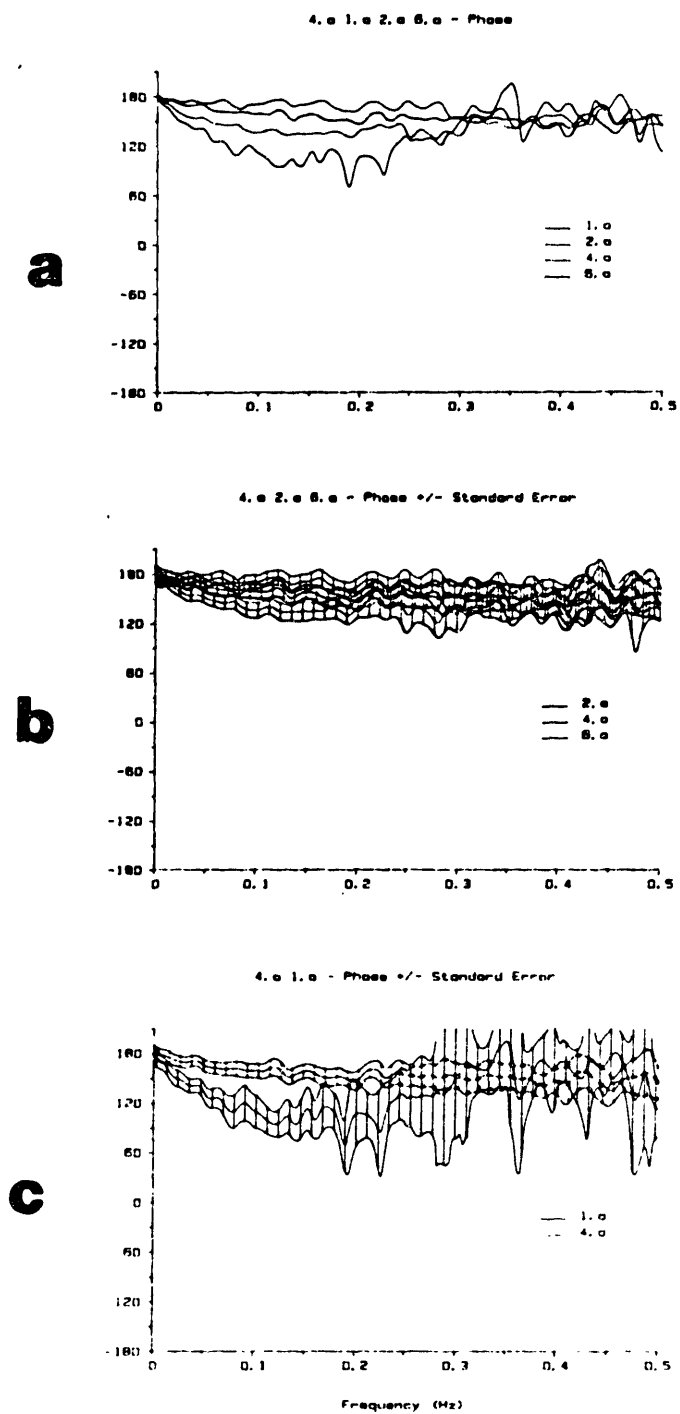


Figure 1.8. Group-average phase estimates for vagal stimulation experiments. a. Without error bars. b. Plots with error bars for mean stimulatory rates of 2, 4, and 6 Hz. c. Plots with error bars for $f_{\text{mean}} = 1$ and 4 Hz.

quency response at each of the four different mean vagal rates tested. Note that all four transfer magnitude curves in Figure 5.7a fall with increasing modulation frequency, but that the precise shape of these curves differs from one mean level of vagal tone to another. Error bars, included in Figure 5.7b, represent the standard error of the mean estimate, as discussed in Section 4.5.3. Although the four magnitude plot error zones overlap for frequencies beyond 0.1 Hz, they clearly become quite distinct at very low modulation rates. Using the Student's t-test [110], one finds that at any point where the standard error of the means for two different magnitude plots just touch (given that each curve represents the group average of eight terms, and assuming the error bars for the two curves are roughly equally wide), there is an 82% certainty that the curves are indeed different. When comparing two non-neighboring transfer magnitude curves, the statistical significance of their differences is obviously even greater. For instance, when the curves are separated by four times their standard error (e.g., the $f_{\text{mean}} = 2$ Hz and $f_{\text{mean}} = 6$ Hz curves at D.C.), the certainty is 99%.

The phase plots shown in Figure 5.8a similarly display a dependence on the operating point at which they were obtained. Phase error zones for mean vagal rates of 2 Hz, 4 Hz, and 6 Hz are displayed in Figure 5.8b, and for 1 Hz and 4 Hz in Figure 5.8c. While the error bars in the $f_{\text{mean}} = 1$ Hz phase plot are fairly wide, significant differences between the four average phase curves are nonetheless discernible over modulation frequencies out to 0.3 Hz.

The data from the magnitude plots presented in Figure 5.7 can be rearranged so as to demonstrate certain nonlinearities in the SA nodal

response to fluctuations in vagal tone. In particular, Figure 5.9 shows how the gain of the system is operating point dependent, rather than constant as in a linear system. In this figure, the transfer function magnitude is plotted against vagal stimulation rate for three different modulation frequencies: D.C., 0.05 Hz, and 0.1 Hz. The value of the ordinate at each plotted point is simply the transfer magnitude at that operating point and modulation frequency. If the system were linear, each curve would maintain a constant gain and thus appear as a horizontal line. Since the four transfer magnitude plots essentially overlaid each other at a modulation frequency of 0.1 Hz, the gain curve for that frequency is essentially horizontal. By contrast, at D.C. the magnitude plots are maximally disparate, so the corresponding gain curve is far from a constant line. Note that if the latter curve were integrated, turned upside-down, and shifted vertically so that the ordinate represented absolute heart rate instead of system gain, then a plot similar to Figure 5.4 would be obtained.

5.3.2 Sympathetic Stimulation

The D.C. characteristics from one representative experiment, relating SA nodal rate to mean frequency of sympathetic stimulation, are shown in Figure 5.10. This plot shows the relatively low level of sympathetic tone at which the system response saturates, as mentioned above. Time series of the instantaneous stimulation rate and SA nodal rate from an experimental run where $f_{\text{mean}} = 1.0$ Hz, along with their corresponding autospectral estimates, are shown in Figure 5.11. The digital filter band-edge for the GWN modulator was set to 0.5 Hz for

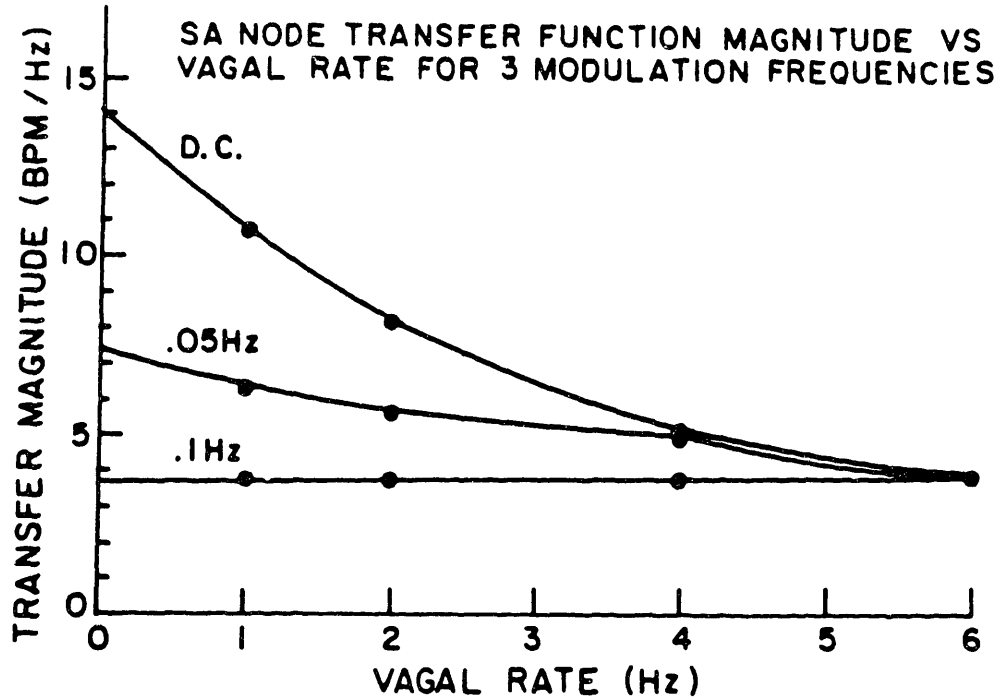


Figure 5.9. System gain plots for SA nodal response to vagal stimulation for three modulation frequencies (D.C., 0.05 Hz, and 0.1 Hz). The gain at each point is the transfer function magnitude for that level of vagal tone and modulation frequency taken from Figure 5.7a.

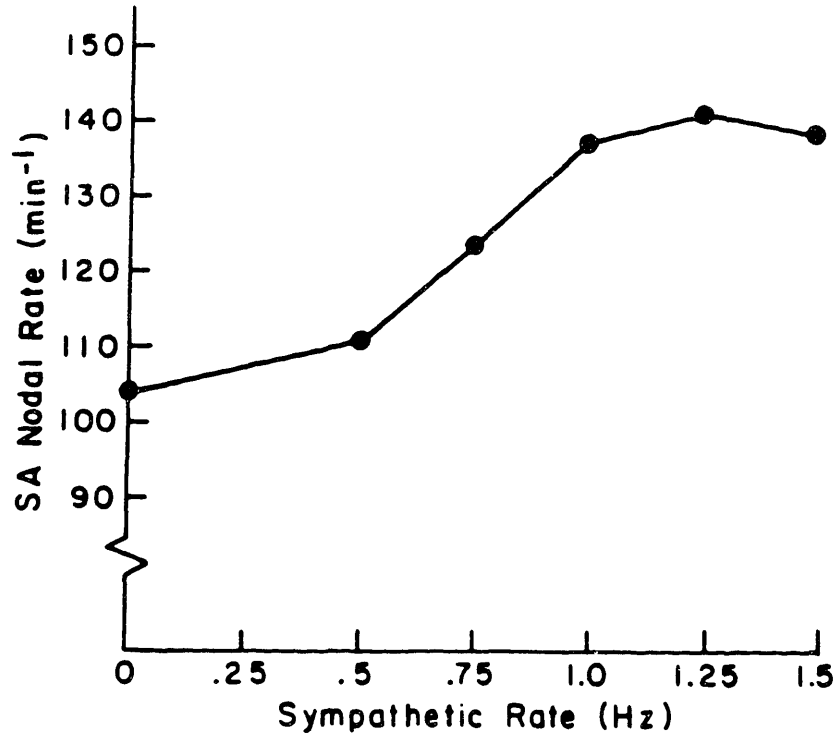


Figure 5.10. Mean SA nodal rate vs sympathetic stimulation frequency.

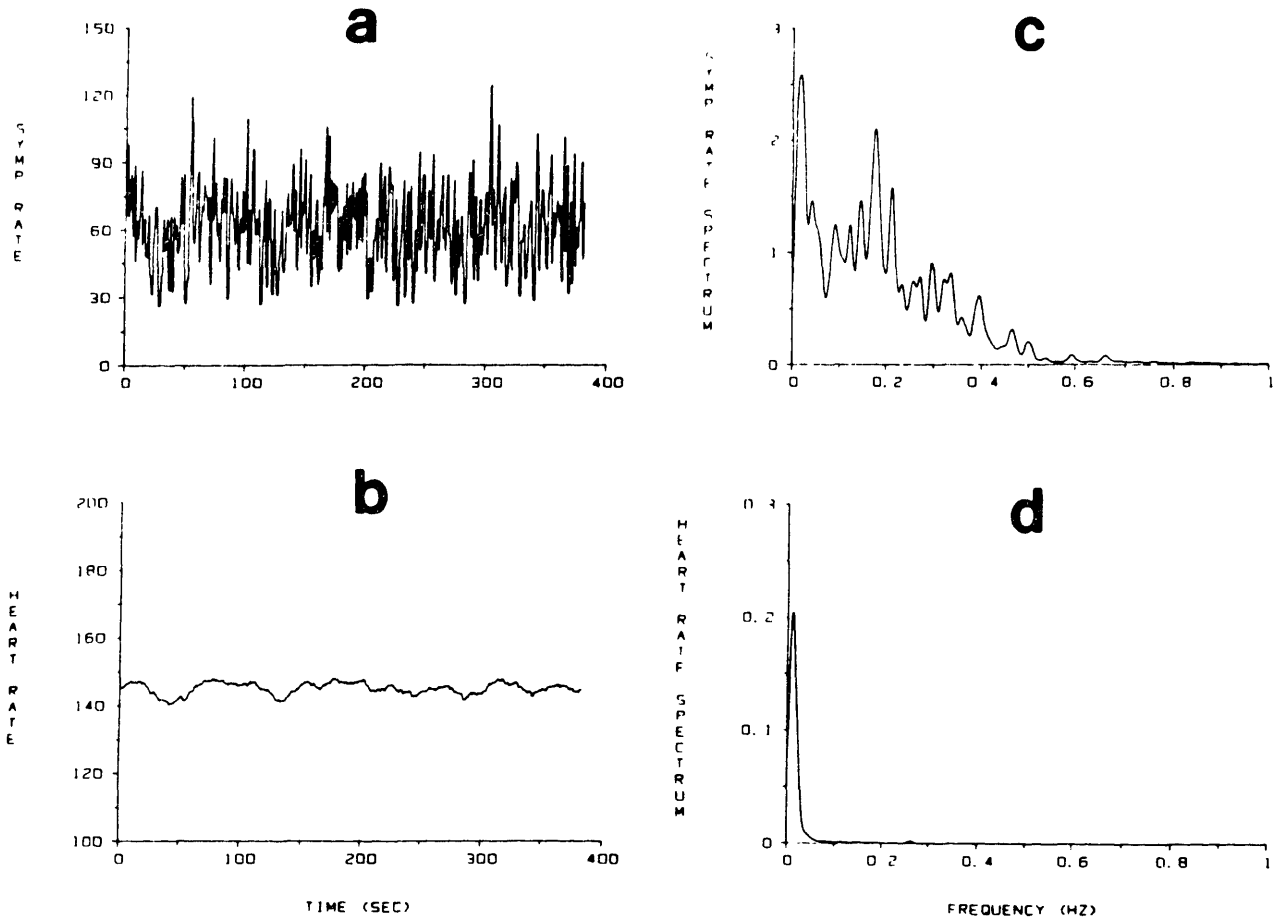


Figure 5.11. Signals from an experimental run of sympathetic stimulation. a. Instantaneous sympathetic pulse rate. b. Resulting SA nodal rate. c. Power spectrum of (a). d. Power spectrum of (b).

this run. Comparison between Figures 5.5 and 5.11 reveals the relative lack of high frequency fluctuations in SA nodal rate that are inducible through modulation of sympathetic tone.

The corresponding transfer magnitude and phase curves, coherence function, and impulse response for this experimental run are shown in Figures 5.12a, b, c, and d. The transfer magnitude curve confirms the lack of high frequency response of the SA node to sympathetic fluctuations, although the coherence plot shows that the response is coherent out to at least 0.25 Hz, even if of low amplitude. The phase function falls with modulation frequency, suggesting the presence of a delay in the SA nodal response to sympathetic fluctuations. The impulse response curve also reveals a delay of 2 to 3 seconds, and it maintains a significantly nonzero level much longer than that shown for vagal stimulation. Note that the impulse response curve here is entirely causal, which serves as a check that the transfer function estimate is consistent with a physically realizable system.

Group average transfer function magnitude and phase plots, pooled from the eight sympathetic stimulation experiments, are shown in Figures 5.13a and c. Confidence zones representing the standard error of the mean transfer magnitude estimates for $f_{\text{mean}} = 1$ Hz and $f_{\text{mean}} = .5$ Hz are displayed in Figure 5.13b. (As these error bars are substantially wider than those in the vagal stimulation transfer plots, a complete graph showing error bars for all five mean levels of sympathetic drive has been omitted since the overlap among the error zones becomes intractably confusing.) Note that the abscissa here extends to only 0.25 Hz (instead of 0.5 Hz, as in Figures 5.7 and 5.8), to enable better

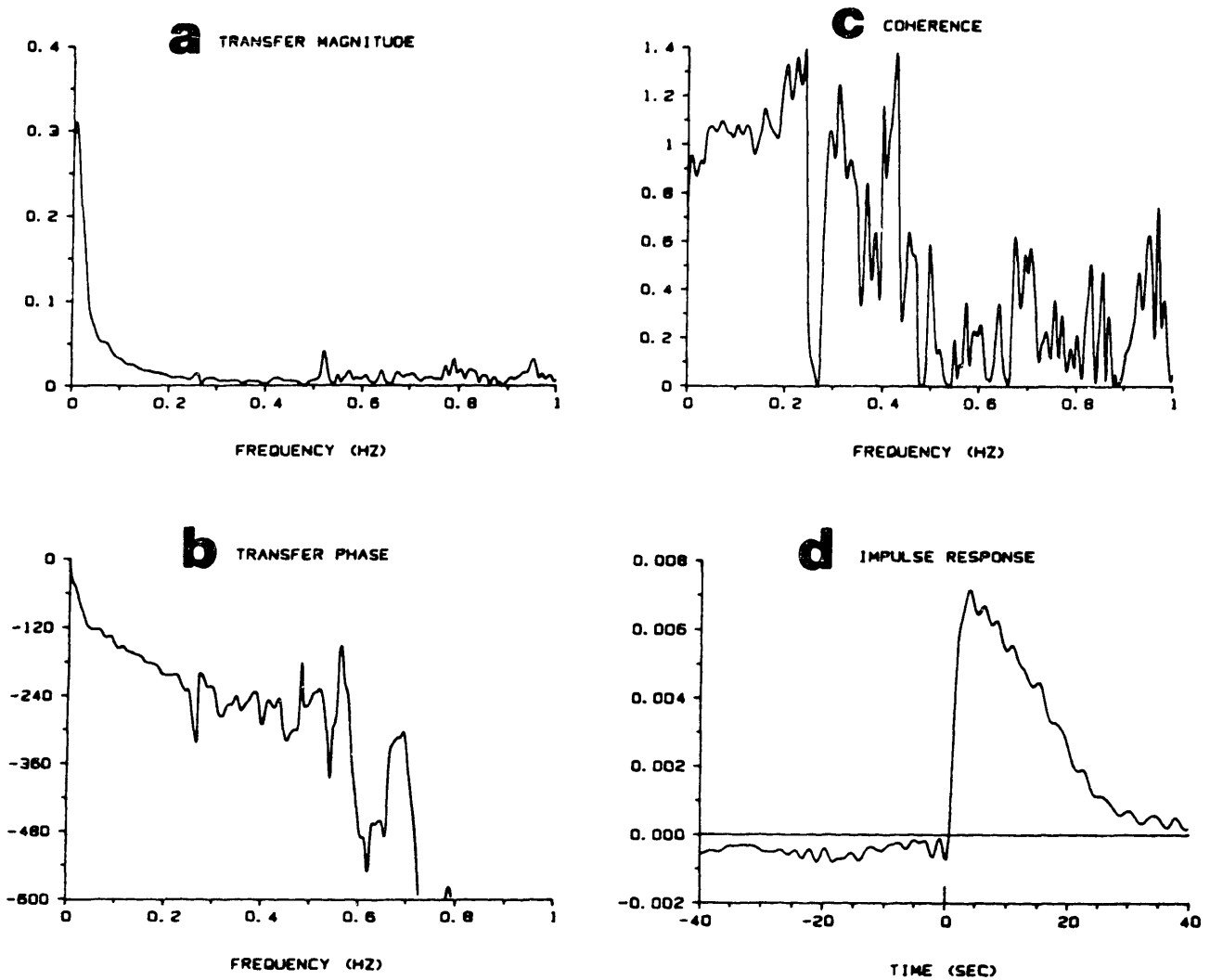


Figure 5.12. Transfer function magnitude (a), phase (b), coherence (c), and impulse response (d) estimates for experimental run of sympathetic stimulation. Coherence values greater than unity reflect some degree of error in estimating the coherence function. Note complete causality in impulse response curve.

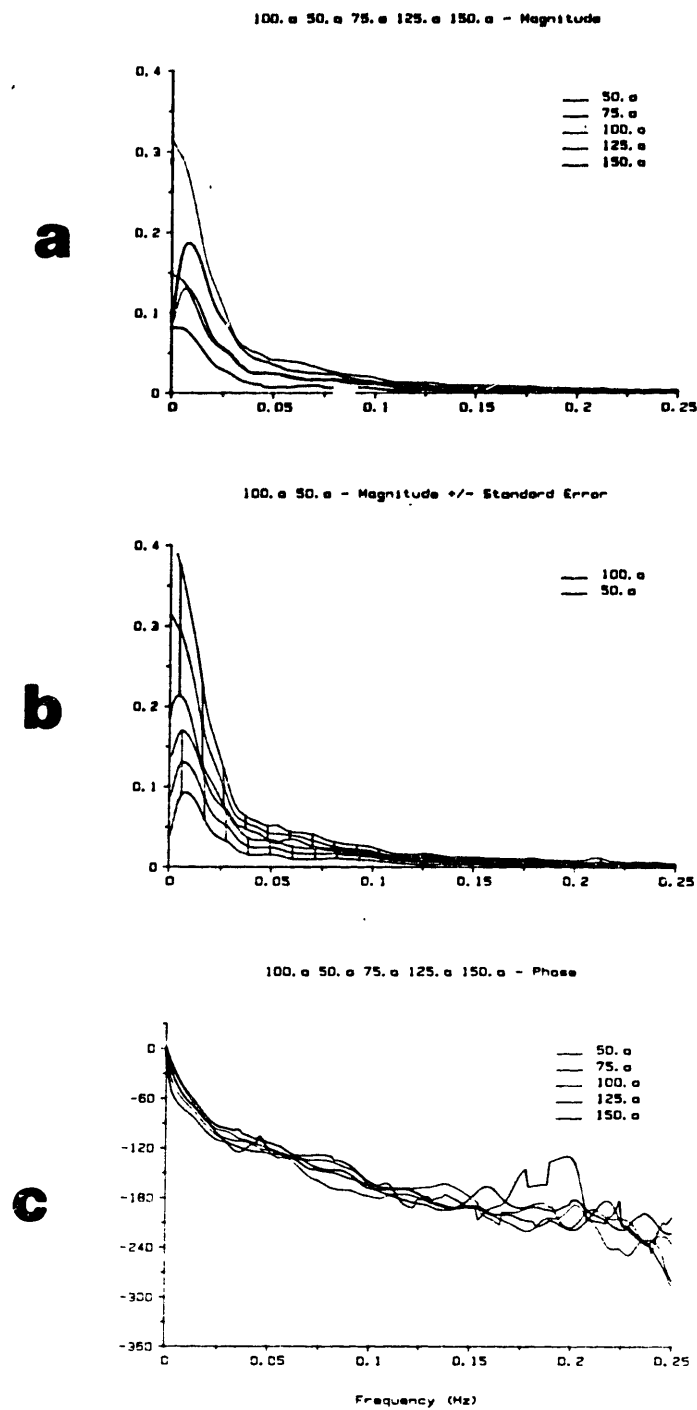


Figure 5.13. Group-average transfer function magnitude and phase plots pooled from sympathetic stimulation experiments. a. Magnitude plots for mean stimulation rates of 0.5, 0.75, 1.0, 1.25, and 1.5 Hz, shown without error bars. b. Magnitude plots with error bars for $f_{\text{mean}} = 0.5$ Hz and 1.0 Hz. c. Phase plots for the five mean stimulation rates. Error bars were omitted in (c), as the phase curves clearly overlie each other. In these graphs, the label prefix refers to the mean stimulatory frequency for that curve, multiplied by 100.

visualization of the graphs in the frequency band below 0.05 Hz.

The transfer magnitude plot for all five mean stimulation rates displays low-pass filter behavior, as in the vagal stimulation experiments. Compared with the nodal response to fluctuations in vagal tone, however, the band-pass edge here is lower and the roll-off steeper, such that the magnitude of the response to sympathetic fluctuations becomes negligible beyond 0.1 Hz. At the very lowest modulation frequencies, the SA nodal response to sympathetic perturbations, like the response to changes in vagal tone, depends on the operating point, with the greatest transfer magnitude occurring at the lowest mean rate of sympathetic stimulation tested.

The transfer phase curves for these experiments, in contrast with the magnitude plots, display remarkable similarity from one operating point to another. Note that the phase curves for all five mean rates of sympathetic stimulation fall almost linearly with increasing modulation frequency at a rate of roughly 1200 degrees/Hz. This attribute of the transfer plots suggests the presence of a greater than 3 second delay in the SA nodal response to sympathetic fluctuations.

Finally, gain curves demonstrating the operating point-dependence of the transfer function magnitude are plotted in Figure 5.14 for three frequencies of sympathetic modulation: D.C., 0.025 Hz, and 0.05 Hz. These curves were derived from the transfer magnitude plots of Figure 5.13a, as was done in Figure 5.9 for the vagal stimulation experiments. The wide departure of these curves from constant gain, especially for the D.C. case, reveals the presence of system nonlinearities in the SA

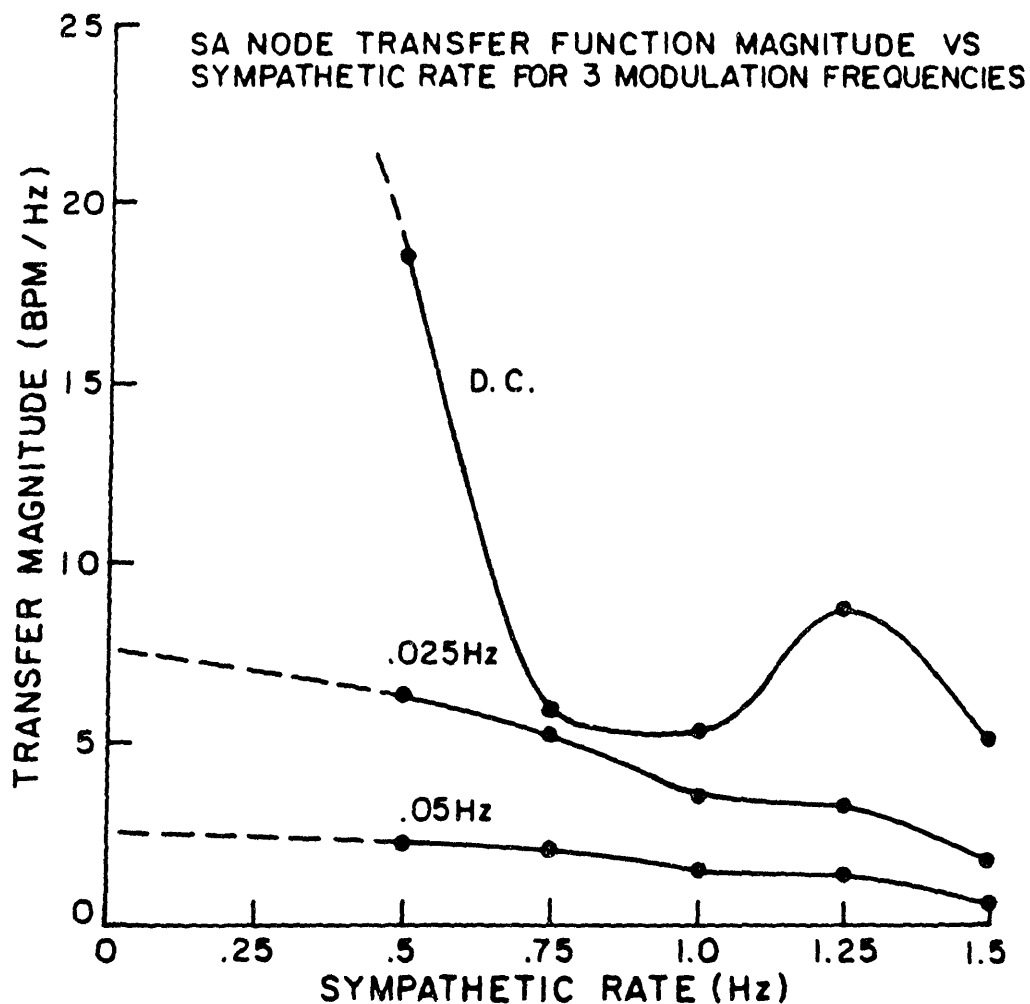


Figure 5.14. Gain curves for SA nodal response to sympathetic stimulation for input modulation frequencies of D.C., 0.025 Hz, and 0.05 Hz. These plots are analogous to those shown in Figure 5.9 for vagal stimulation, and are based on the transfer magnitude curves in Figure 5.13a.

nodal response to fluctuations in sympathetic tone, just as were found in the nodal response to changes in vagal activity.

5.4 Discussion

5.4.1 Experimental Response Characteristics

Several points may be made regarding the results presented above. First and perhaps most important, these data demonstrate the utility of broad-band stimulation and transfer function analysis in studying cardiovascular regulatory dynamics. Not only were we able to characterize the SA nodal response to fluctuations in vagal and sympathetic tone over the entire band of physiologically important modulation frequencies, but we obtained these frequency response curves at multiple mean rates of neural stimulation. Through pooling of this data, we could examine the system response as a function either of frequency of autonomic fluctuations or of operating point.

In considering the frequency response of the SA node to modulation of either sympathetic or vagal tone, we found that at any given operating point, the system behaves as a low-pass filter. This is consistent with the observations by Chess and Calaresu [24] and Penaz [105], whose describing function characterizations of the SA nodal response to sinusoidally modulated vagal tone also demonstrated the low-pass filter behavior of the system. Furthermore, our finding that the nodal response to sympathetic fluctuations consists of a very narrow low-frequency band-pass region coupled with a pure delay is in concert with the data presented by Warner and Cox [136]. Their tracings from animal

experiments show that upon initiation of sympathetic stimulation, the heart rate climbs slowly and only after a several second delay, and then upon cessation of the neural excitation, the heart rate falls as a dying exponential. Similarly, through the implementation of selective autonomic blockade, Akselrod et al [4] found that spontaneous fluctuations in heart rate at frequencies above 0.2 Hz are almost completely vagally mediated. Of course, it remains entirely possible that this paucity of high-frequency content in sympathetically-mediated spontaneous heart rate fluctuations stems from low-pass filter behavior in the central production of sympathetic outflow, as well as in the operation of the SA node. We are interested in trying to relate our findings to the kinetics of neurotransmitter release and receptor binding in the SA node. In the following section, we compare our results with predictions of Warner and Cox's 25-year-old model of neurotransmitter kinetics [136]. Unfortunately, relatively little new information on these kinetics is available, despite active research in this area [68].

Note that the data we display in the form of transfer function magnitude and phase curves could also be used to determine the best-fit locations of poles and zeroes in a Nyquist plot [38]. This sort of decomposition is best performed through a multi-variate autoregressive analysis, as discussed in Chapter 3. However, reiterating the point made in Section 3.4, implementation of autoregressive analyses imposes various assumptions about the system at hand, regarding not only the linearity of operation, but the complexity of the system as well. Since we have pursued an approach specifically designed to avoid making the assumptions required by a parametric model, no attempt is made here to

fit the observed transfer functions to a set of poles and zeroes.

The finding of greatest interest suggested by our data is a dependence of the transfer function shape on the operating point, particularly when considering the transfer between modulation of vagal tone and SA nodal rate. The existence of such a dependence is not entirely surprising given the nonlinear shape of the curve relating heart rate to fixed frequency of vagal stimulation (i.e., Figure 5.4). However, our approach has enabled us to characterize the extent of this operating point dependence over the full range of physiologically important modulation frequencies, instead of solely at fixed rates of stimulation. In fact, as Figure 5.9 shows, around some operating points the system appears quite linear, or at least displays much less operating point dependence than in the quasistatic case (D.C. curve).

The presence of operating point dependence in system behavior is seemingly in contradiction with the assumption of linearity required for appropriate application of transfer function analysis. We suggest, however, that the SA nodal response may be considered piece-wise linear. In other words, its response within a narrow range around a particular operating point is quite linear, as evidenced by the generally good coherence between input excitation and output signal, but the precise character of the transfer function changes somewhat from one operating point to another. This understanding of SA nodal function sheds new light on the interpretation of changes in spectral content of spontaneous heart rate fluctuations between different physiologic states. For example, our data show that a diminution in low-frequency power in the heart rate variability may result from an increase in mean vagal or

sympathetic tone even without any change in the amplitude of vagal or sympathetic fluctuations. Furthermore, the gain curves shown in Figures 5.9 and 5.14 suggest the system nonlinearities become exaggerated at low modulation frequencies, but are less apparent at frequencies beyond 0.1 Hz. Thus, the assertion made by some investigators that specific peaks in the power spectra of spontaneous heart rate fluctuations correlate well with changes in vagal or sympathetic tone [42,47,77,103] may have questionable validity at very low modulation frequencies.

5.4.2 Warner and Cox Model of the Sino-atrial Node

The Warner and Cox model of SA node regulation was mentioned briefly in Section 5.1. At this point, we consider the model's predictions regarding the heart rate response to broad-band fluctuations in vagal and sympathetic tone. These predictions can then be compared to the observed transfer relations presented above. The set of coupled equations that Warner and Cox devised to describe vagal influence on SA node function [136] are shown in Figure 5.15a. Note that the resulting heart rate HR_v varies inversely with the instantaneous synaptic acetylcholine concentration C_2 . C_2 , in turn, is incorporated in the coupled pair of differential equations.

The model for sympathetic modulation of nodal function is depicted in Figure 5.15b, along with the corresponding set of state relations. Note that this half of the Warner and Cox model is more complicated than the part that describes vagal effects, since here a second messenger AB is taken into account. The resulting differential equations are thus of higher order than those for vagal activation.

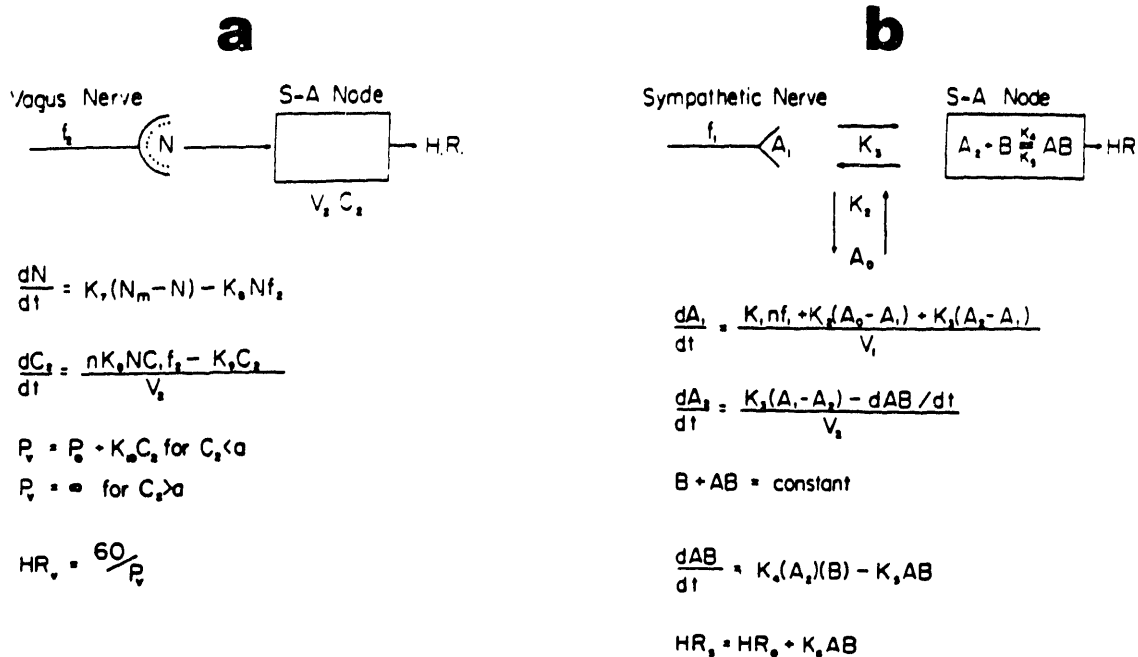


Figure 5.15. Warner and Cox model of neural regulation of heart rate. a. Schematic of synapse between vagal fiber and nodal cells, with associated differential equations describing release, binding, and degradation of neurotransmitter molecules. f_2 is the vagal stimulation rate, N is the number of acetylcholine vesicles at each nerve terminal, N_m is the maximum number of vesicles, C_1 is the concentration of acetylcholine in the vesicles, C_2 is the concentration in the synaptic fluid outside the vesicles, V_1 is the volume into which the acetylcholine is diluted, n is the number of fibers responding to the stimulus, P_v is the period of the heart cycle, and K_7 , K_8 , K_9 , and K_{10} are constants.

b. Diagram of synapse with sympathetic nerve fiber. Equations describing dynamics of norepinephrine effect on nodal cells include extra complexity to account for reaction with second messenger. f_1 is the sympathetic stimulation rate, A_1 is the norepinephrine concentration at the nerve ending, A_0 is the concentration in blood, A_2 is the concentration at the active site on the SA node, B is a substance which must react with norepinephrine to give rise to the second messenger AB , V_1 and V_2 are apparent volumes of dilution for A_1 and A_2 , respectively, n is the number of fibers responding to the stimulus, and K_1 through K_6 are constants. These schematics and equations are reproduced from Warner and Russell, 1969.

We implemented the two halves of the model on a digital computer, using difference equations in place of the differential relations and updating the state variables at an effective clock rate of 2.8125 Hz. Since this was the frequency at which instantaneous rate signals were derived in the dog experiments, we could drive the computer-implemented model with the measured vagal or sympathetic rate signal from an experimental run and compare the model's resulting SA nodal rate to that found empirically. Of course, both halves of the Warner and Cox model include several free parameters for which appropriate numerical values had to be chosen. This was done through a fairly painstaking trial-and-error search so as to match the model's D.C. characteristics to the experimental curves shown in Figures 5.4 and 5.10. In addition, the rate constants of the model were adjusted to match the model's dynamics to that observed experimentally when either the vagus was stimulated with a GWNFM pulse train with $f_{\text{mean}} = 4$ Hz or the sympathetic chain was stimulated at a mean rate of 1 Hz. Once these best-fit model parameters were chosen, they were left unchanged as other experimental neural rate signals were then applied as the driving sequence.

Figure 5.16 shows magnitude and phase plots for the Warner and Cox model when the vagus nerve is driven with pulse trains of mean rate 2, 4, and 6 Hz. While the transfer magnitude plot for the 4 Hz mean rate signal closely resembles the corresponding experimental curve in Figure 5.7a, the curves for mean rates of 2 Hz and 6 Hz differ from their experimental counterparts in that they do not merge until the modulation frequency exceeds the input signal band-edge (0.7 Hz), where the transfer plots become too noisy to interpret. In fact, the model

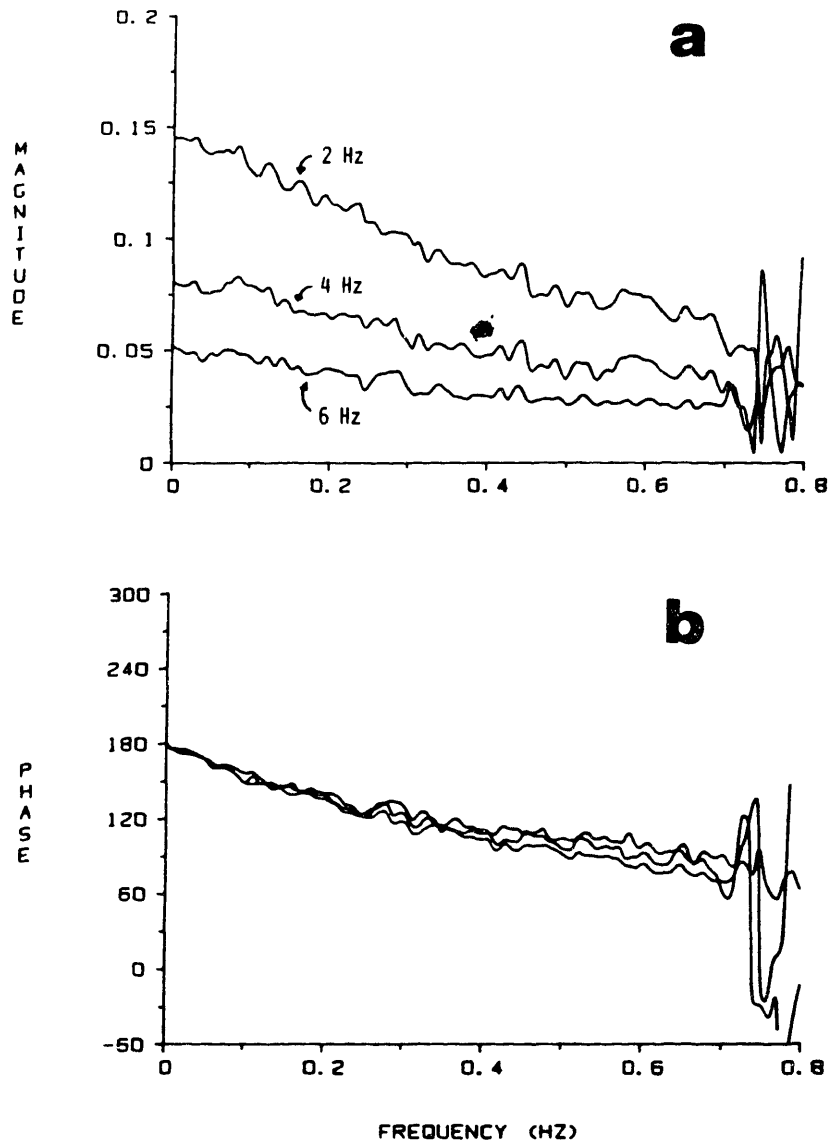


Figure 5.16. Results of implementation of Warner and Cox model for vagal stimulation. Model parameters were adjusted to make best fit with experimental data, where the mean stimulation rates were 2, 4, and 6 Hz. a. Transfer magnitude plots. b. Transfer phase curves.

transfer magnitude curves appear identical to each other to within a scale factor, unlike the experimental plots where the roll-off is increasingly rapid at progressively lower mean rates of excitation. The model phase plots essentially overlie each other, further supporting the assertion that the model filter characteristics change with the operating point only by a scale factor.

The model transfer magnitude and phase plots for sympathetic modulation are shown in Figure 5.17. Again, these curves essentially lack operating point dependence. However, since the experimental magnitude plots, shown in Figure 5.13a, depend somewhat unclearly on the operating point, and the experimental phase plots (Figure 5.13c) do in fact overlie each other, it is difficult to assess to what extent the model transfer relations for sympathetic stimulation do or do not reconcile with the experiments. It is quite clear, however, that in order for operating point dependence in the model transfer functions to appear, the model parameters must change as a function of mean vagal or sympathetic stimulation. To the extent that Warner and Cox did not consider this possibility, their model appears incomplete.

5.5 Comments

While the data presented in this chapter provides new insights into SA nodal function, a couple of remarks are in order regarding the limitations of this work. An important assumption that underlies our approach is that neural stimulation with supramaximal current spikes emulates endogenous neural activity and has the same influence on nodal function. In reality, fibers within either the vagus nerve or the

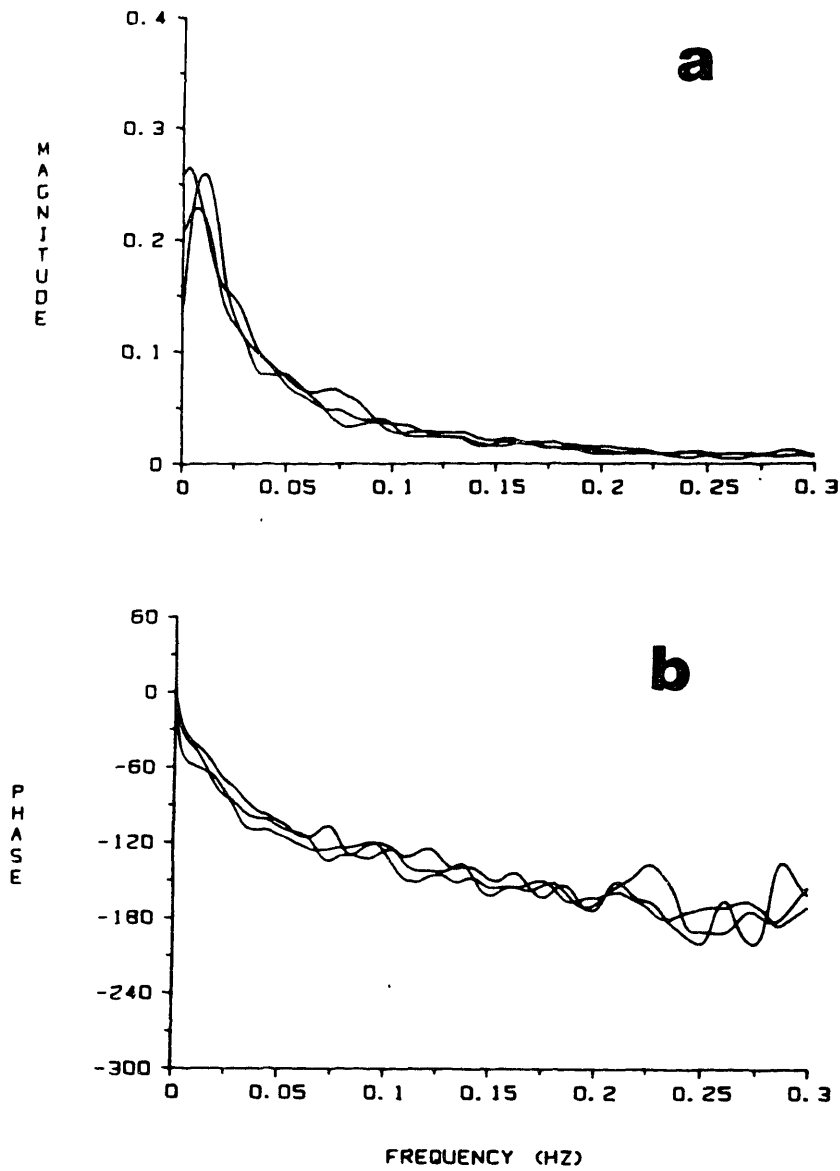


Figure 5.17. Results of implementation of Warner and Cox model for sympathetic stimulation, for mean rates of 0.75, 1.0, and 1.25 Hz. a. Transfer function magnitude plots. b. Transfer phase curves.

stellate ganglion are not, in general, all recruited simultaneously in moment-to-moment autonomic regulation, as occurs in supramaximal activation. Furthermore, among the nerve fibers that do participate in the conduction of endogenous neural impulses, their activations occur asynchronously. Thus, efferent electrical activity measured in a multifiber unit of the vagus or sympathetic nerve might contain pulses whose mean frequency is an order of magnitude higher than those employed in supramaximal stimulation, and yet elicit the same response in terms of changes in heart rate. This is because each recorded spike of endogenous activity represents conduction in only a small number of neurons so that many such spikes will be seen when neurotransmitter is released at a rate comparable to that accompanying synchronous activation. Of great interest would be a study where vagal and sympathetic tone are modulated reflexogenically (e.g., with manipulations of blood pressure) and the resulting endogenous neural activity is measured. Then transfer relations between the true instantaneous neural tone and SA nodal rate could be obtained.

The other issue left unaddressed in this chapter is interactions between vagal and sympathetic activity. In Section 5.1, we mentioned the work of Levy et al [51,82,90,92], who investigated these interactions, but in our experimental protocol we never stimulated both limbs of the autonomic efferent system simultaneously. The reason for this is largely due to equipment limitations. In particular, we built only a single-channel voltage-to-current converter, preventing us from delivering independent pulse trains to the vagus and sympathetic nerves. In future work with additional equipment, we hope to more fully explore the

effects of sympathetic/parasympathetic interactions on the transfer properties of the SA node.

Chapter 6: Study of Autonomic Response to Respiratory Activity*

6.1 Introduction

In Chapter 2, the effects of respiration on the cardiovascular system were briefly introduced. While these effects may include phasic changes in contractility and peripheral resistance as well as in heart rate, it is the latter that is considered in this chapter. The rhythmic variation in heart rate linked to the respiratory cycle, termed the respiratory sinus arrhythmia (RSA), has been shown to result largely from modulation of vagal efferent activity [42,46,77,78]. While some studies have also implicated sympathetic efferent activity in the mediation of the RSA [46,91], vagal influences are generally recognized as the predominant factor. Several investigators, in fact, have suggested that quantification of the RSA could provide a measure of mean vagal tone [42,47,77]. Furthermore, Eckberg [43] has suggested that measurement of the RSA can provide a window on autonomic function in the clinical setting, since the magnitude of the RSA depends on a multiplicity of physiologic factors. As vagal activity in general, and the RSA in particular, is influenced by higher cortical function, diminution of the RSA has been shown to correlate with mental loading [62] and with psychiatric illness [114]. In addition, it has been well established that the RSA declines with age [56,59,71], and Hrushesky et al [61] suggest this phenomenon reflects progressive deterioration in cardiac reserve. In this chapter, we discuss the transfer relation between

* Much of the material in this chapter was presented at the 1986 conference on Computers in Cardiology and published in the conference proceedings [23].

instantaneous lung volume and heart rate, and show how quantitative characterization of this relation may represent a more sensitive metric of autonomic integrity than measurement of the heart rate fluctuations alone.

It is worthwhile to review the various physiologic mechanisms that have been cited as responsible for the genesis of the RSA. As far back as 1865, Traube [134] discovered that the RSA persists in experimental animals even after they have been paralyzed by administration of curare. Since all the mechanical variations associated with normal respiration (e.g., lung inflation, chest wall movement, and changes in intrathoracic pressure) are abrogated by curarization, Traube concluded that the arrhythmia could not be explained other than by a direct neural link between respiratory centers within the brainstem and centers controlling heart rate. The existence of such a central neural connection in the genesis of the RSA, although of unclear survival value, has been substantiated by numerous other investigators [7,58,59,72,78,84,91].

In 1915, Bainbridge presented his classic paper [9] describing the now well-known reflex named for him, in which the heart rate accelerates in response to increased atrial distention. In a second paper [10], Bainbridge discussed the role this reflex plays in generating the RSA. Both Kitney [84] and Melcher [50,98,99] have provided evidence supporting the importance of the Bainbridge reflex as a mechanism responsible for, or at least contributing to, the RSA.

Anrep et al [7,8] showed that stretch receptors in the lungs and chest wall are stimulated on inspiration, and that neural activity from

these receptors has an inhibitory influence on vagal outflow, thus eliciting an acceleration in heart rate. Angelone and Coulter [6] and Clynes [26] also considered thoracic stretch receptors the primary afferent limb giving rise to the RSA. Davies and Neilson [31] suggested that a fourth mechanism responsible for the RSA may be phasic changes in arterial baroreceptor activity resulting from the effect of respiration on blood pressure in the aorta and other thoracic vessels. This hypothesis has been essentially refuted by more recent investigations that demonstrated rises in heart rate with respiration that were paradoxically in sync with the rising phase of arterial pressure [50,71]. However, a number of studies have provided convincing evidence that the sensitivity of the arterial baroreceptors, or of the brainstem centers that receive their information, is reduced during the inspiratory phase of the respiratory cycle [45,55,98,99]. This would obviously lead to vagal inhibition and an elevation in heart rate during inspiration, which is what is generally observed.

A final pathway that may contribute to the mediation of the RSA is an intra-cardiac reflex. In fact, Bainbridge [10] suggested that the reflex tachycardia with atrial distention he observed may or may not involve the central nervous system, and could conceivably lie entirely within the heart. More recently, Hrushesky et al [61] described the presence of the RSA in a man who had received a transplanted, and thus denervated, heart. While the anatomy of such an intra-cardiac pathway remains unknown, its existence has not been convincingly ruled out.

Referring to Figure 2.5, we see that the components of the cardiovascular control system that mediate the RSA are largely in common

with those involved in other autonomic reflexes. The vagus and sympathetic efferent nerves and the sino-atrial (SA) node are involved as described above, and a substantial chunk of the central autonomic nervous system (ANS) participates as well. Our approach toward studying the RSA was to characterize the network of elements that give rise to the arrhythmia in much the same way we investigated the behavior of the SA node in Chapter 5. Hopefully, this information would then shed light on autonomic control of a variety of cardiovascular responses.

A number of workers have characterized the generation of the RSA by measuring the amplitude of heart rate fluctuations at a given tidal volume and fixed rate of respiration. A composite plot of these measurements made at many different respiratory rates then comprises a describing function characterization of the system involved [6,59,83,91,141]. The collection of data at enough different frequencies of respiration to adequately characterize the system at hand can obviously take an inordinate amount of time. Furthermore, the results may suffer from artifacts that stem from changes in experimental conditions between data points. For example, when subjects are asked to take very few breaths per minute, they may easily become hypercapneic, which may in turn affect the resulting amplitude of the RSA.

We sought a method for characterizing the RSA-generating system in humans whereby the system response could be determined at all frequencies of interest simultaneously through the use of broad-band input waveforms. Since the system input here is the instantaneous lung volume, we needed to devise a technique to whiten the normally narrow-band respiratory activity without significantly disrupting the normal

ventilatory mechanics. The utility of such an approach was recognized by Womack [141] and Ahmed et al [1], but these investigators claimed it is impossible or impractical for subjects to breathe in a manner that would broaden the respiratory signal content. In the following section, we describe a very simple method for eliciting such broad-band respiratory activity.

6.2 Methods

Eighteen volunteer subjects (10 men and 8 women) aged 21 to 34 years, with no history of cardiopulmonary disease, participated in this study. The apparatus involved in data collection and digitization is depicted in Figure 6.1. Instantaneous lung volume was measured with a two belt chest-abdomen inductance plethysmograph (Ambulatory Monitoring, Inc.), calibrated with an 800 cc bag. This signal and the surface ECG (lead II) were recorded on an FM tape machine, as described in Chapter 4. Data was collected in 6-minute segments, with the subject in both standing and supine positions. After a postural change, the subject was given five minutes for hemodynamic equilibration before the next data segment was collected.

The subject was instructed to initiate an inspiratory/expiratory cycle each time he was cued by an audible tone. The sequence of tones, or beeps, was generated by a PDP-11/23 based computer (Digital Equipment Corp.). The computer was programmed to space the beeps evenly in time at a preset rate λ_0 for the first few minutes so that the subject could find a comfortable depth of inspiration. The program would then switch to a mode in which the tones were spaced at irregular intervals, but

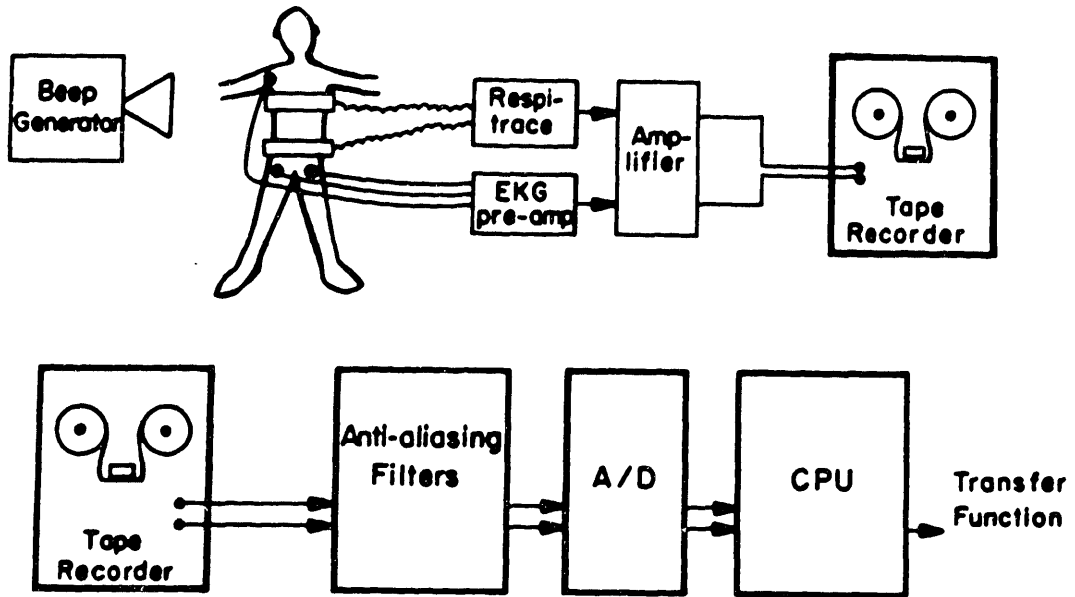


Figure 6.1. Apparatus for recording and analyzing data collected from subjects instructed to breathe on cue to a sequence of beeps.

with the same mean occurrence rate λ_0 , for six minutes of data collection. Importantly, although we controlled the timing of the subject's breathing pattern, he was allowed to maintain his normal residual lung volume and to titrate the depth of his inspirations throughout the experiment, thus preserving essentially normal blood gases and ventilatory mechanics.

A rough idea of the spectral content of the resulting instantaneous lung volume signal $x(t)$ can be derived as follows. $x(t)$ approximates the result of convolution between a sequence of unevenly spaced delta functions $q(t)$ and the average single-cycle respiratory waveform $r(t)$. Thus,

$$x(t) = q(t) * r(t) \quad (6.1)$$

where "*" is the convolution operator. This leads to the relationship in the frequency domain:

$$S_{xx}(f) = S_{qq}(f) \cdot |R(f)|^2 \quad (6.2)$$

where $S_{xx}(f)$ is the power spectrum of $x(t)$, $S_{qq}(f)$ is the power spectrum of the pulse sequence $q(t)$, and $|R(f)|^2$ is the Fourier transform magnitude squared of the waveform $r(t)$. The input signal $x(t)$ is sufficiently broad-band for transfer function analysis if its power spectrum $S_{xx}(f)$ is significantly non-zero for all frequencies f of interest. This requires that both $S_{qq}(f)$ and $|R(f)|^2$ are non-zero over the same frequency range. $|R(f)|^2$ falls to zero beyond some frequency, but is assumed to remain significantly non-zero to at least 0.5 Hz. In any case $r(t)$, and thus $|R(f)|^2$, can not be modified without altering the

subject's respiratory mechanics. The shape of $S_{xx}(f)$ thus depends strongly on the nature of $S_{qq}(f)$ within the frequency band of interest, which in turn depends on the distribution of intervals used.

A sensible choice for the distribution of intervals is that of a Poisson process, since the power spectrum of a sequence of Poisson impulses is a constant over all frequencies. The distribution $p_t(t)$ in this case is a decaying exponential in t . Thus,

$$p_t(t) = \lambda_0 e^{-\lambda_0 t} \quad (6.3)$$

where λ_0 is, again, the mean occurrence rate of the tones. The difficulty with this distribution is that not only can arbitrarily short intervals occur, but such intervals are in fact favored to occur. In practice, we found a subject had difficulty initiating a new respiratory cycle if he was in the midst of an inspiratory/expiratory cycle when he heard the next tone, even though we instructed him to attempt to do so. The interval distribution could be modified to avoid this problem by prohibiting intervals shorter than some minimum duration t_{\min} :

$$p_t(t) = \lambda_1 e^{-\lambda_1(t-t_{\min})} \cdot U(t-t_{\min}) \quad (6.4)$$

where $U(\tau)$ equals unity for $\tau > 0$ and zero otherwise.

We further modified the distribution to restrict the intervals between both a minimum and a maximum limit:

$$p_t(t) = k\lambda_1 e^{-\lambda_1(t-t_{\min})} \cdot U(t-t_{\min}) \cdot U(t_{\max}-t) \quad (6.5)$$

as shown in Figure 6.2. λ_1 is chosen such that the mean interval

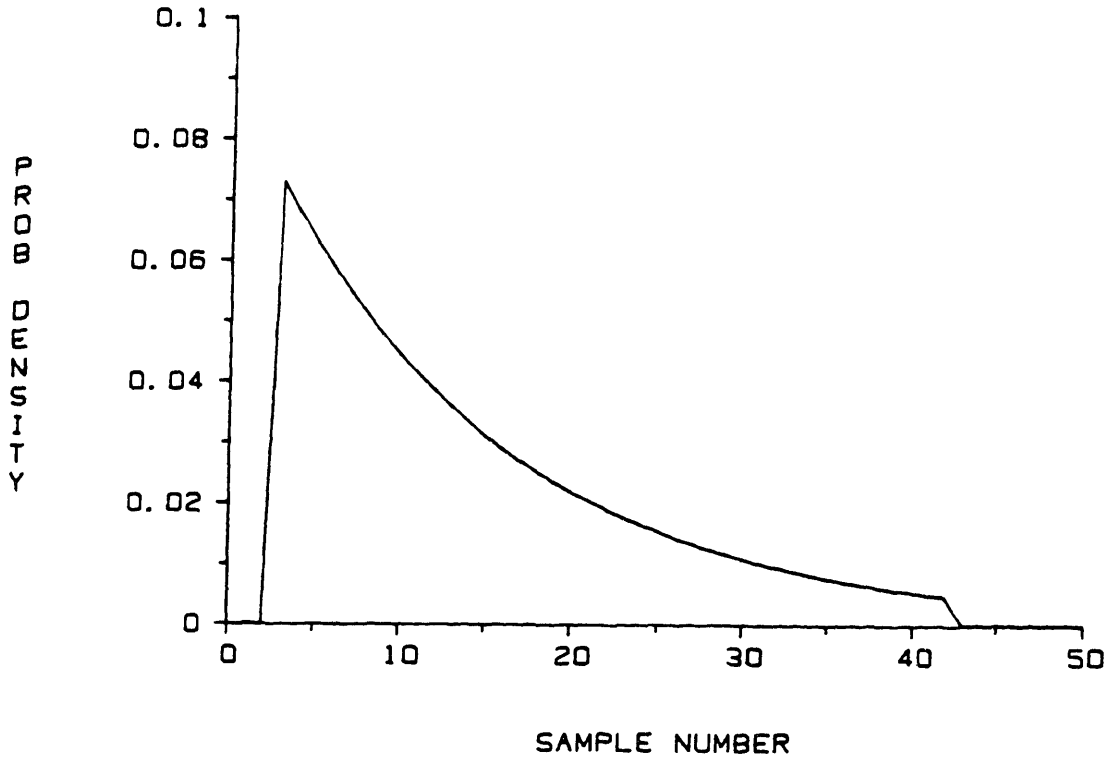


Figure 6.2. Distribution of intervals between successive beeps used to elicit broad-band respiratory activity. The time axis is quantized to a sampling rate of 2.8125 Hz, and the distribution is normalized such that the sample probability masses sum to unity.

remains $1/\lambda_0$, and is found through an iterative technique. The normalization constant k is simply

$$k = \left[1 - e^{-\lambda_1(t_{\min}-t_{\max})} \right]^{-1}. \quad (6.6)$$

The computer was programmed to generate a sequence of intervals t_i from the distribution of equation (6.5) by a transformation of variables, given a sequence of random numbers x_i uniformly distributed between zero and unity. The transformation may be derived as follows: Given $p_t(t)$ defined in equation (6.5), and $p_x(x)$ which equals unity for $0 \leq x \leq 1$ and zero otherwise, we set

$$\int_0^{x_i} p_x(x) dx = \int_{t_{\min}}^{t_i} p_t(t) dt \quad (6.7)$$

Thus,

$$\begin{aligned} x_i &= \int_{t_{\min}}^{t_i} k\lambda_1 e^{-\lambda_1(t-t_{\min})} dt \\ &= k \left[1 - e^{-\lambda_1(t_i-t_{\min})} \right]. \end{aligned} \quad (6.8)$$

Rearranging, we obtain the relation

$$t_i = t_{\min} - \frac{1}{\lambda_1} \ln \left[1 - \frac{x_i}{k} \right]. \quad (6.9)$$

The parameters for the distribution of intervals used in this study were $t_{\min} = 1$ sec and $t_{\max} = 15$ sec, and the mean interval duration was 5 sec.

We found that the imposition of such limits on the intervals

greatly improves the ability of the subject to follow the desired breath generating sequence, while only slightly compromising the broad-band nature of the impulse train $q(t)$. In fact, given the interval distribution $p_{\tau}(\tau)$, the power spectrum of the impulse train $S_{qq}(f)$ can be computed as follows. Since the mean occurrence rate is defined λ_0 , we know that

$$E[q(t)] = \lambda_0 \tag{6.10}$$

where E represents the expectation value operator. The autocorrelation function $R_{qq}(\tau)$ of the signal $q(t)$ may be expressed as

$$\begin{aligned} R_{qq}(\tau) &= E[q(t)] \cdot \text{Prob}\{\text{impulse exists at } t = \tau \\ &\quad \text{given impulse exists at } t = 0\} \\ &= \lambda_0 \left[\delta(\tau) + p_{\tau}(\tau) + p_{\tau}(-\tau) + p_{\tau}(\tau) * p_{\tau}(\tau) \right. \\ &\quad \left. + p_{\tau}(-\tau) * p_{\tau}(-\tau) + \dots \right] \end{aligned} \tag{6.11}$$

where "*" is the convolution operator. If we define $P(f)$ as the Fourier transform of $p_{\tau}(\tau)$ and take the Fourier transform of equation (6.11), we get

$$\begin{aligned}
 S_{qq}(f) &= \lambda_0 \left[1 + P(f) + P^*(f) + (P(f))^2 + (P^*(f))^2 + \dots \right] \\
 &= \lambda_0 \left[1 + \sum_{i=1}^{\infty} (P(f))^i + \sum_{i=1}^{\infty} (P^*(f))^i \right] \\
 &= \lambda_0 \left[\sum_{i=0}^{\infty} (P(f))^i + \sum_{i=0}^{\infty} (P^*(f))^i - 1 \right] \\
 &= \lambda_0 \left[\frac{1}{1 - P(f)} + \frac{1}{1 - P^*(f)} - 1 \right] \tag{6.12}
 \end{aligned}$$

where $P^*(f)$ is the complex conjugate of $P(f)$. Figure 6.3 is a plot of $S_{qq}(f)$, computed from the distribution $p(t)$ shown in Figure 6.2, using the Fast Fourier Transform (FFT) to derive $P(f)$ in equation (6.12). Again, this is the theoretical power spectrum of the impulse train used. The spectrum of the actual respiratory signal is limited by the bandwidth of the average single-breath waveform. Furthermore, since the signals used are realizations of only 6-minutes duration, the actual respiratory power spectrum (computed as described in Chapter 4) for a particular experimental run will differ somewhat from theory and from that in any other run.

Transfer function analysis was performed on data collected from each subject in both supine and standing postures, using the techniques described in Chapter 4. The system input was taken to be the respiratory (instantaneous lung volume) signal, and the output was the instantaneous heart rate derived from the recorded ECG. Group average transfer functions and associated error bars were then computed for each posture by pooling data from the 18 subjects.

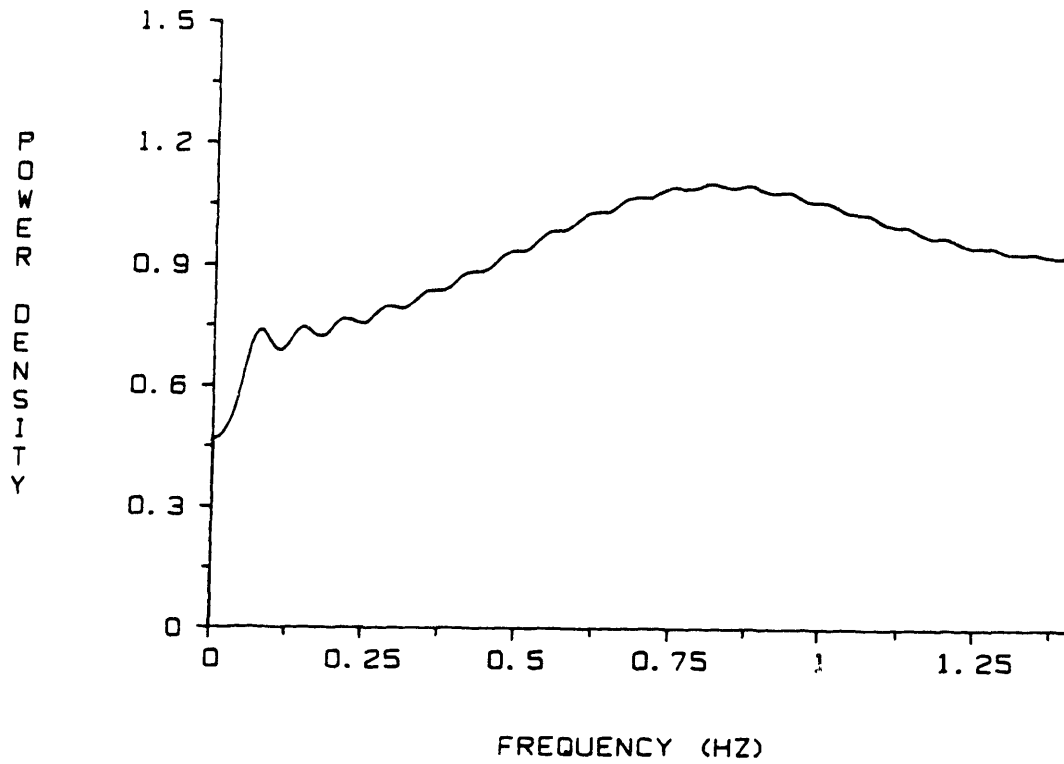


Figure 6.3. Power spectrum for sequence of impulses with interval distribution defined by Figure 6.2.

6.3 Results

Representative respiratory and heart rate signals from an experimental run in which the subject was supine are shown along with their corresponding power spectra in Figure 6.4. The respiratory spectrum (Figure 6.4c) shows that the instantaneous lung volume signal does indeed possess power over a broad range of frequencies (D.C. to 0.4 Hz) during random interval breathing. Note that the hills and valleys of the heart rate spectrum roughly follow those of the respiratory spectrum. The transfer function magnitude and phase estimates and the coherence function computed from these particular data records are shown in Figure 6.5. The coherence plot (Figure 6.5c) indicates that the transfer function estimate is quite reliable over the range from 0.05 Hz to 0.4 Hz.

The group average transfer magnitude and phase plots, with confidence zones representing the standard error of the mean, are shown in Figure 6.6 for both the supine and standing position. These plots were computed using data pooled from all 18 subjects. Although we considered the possibility that systematic sex-related differences could exist in the transfer properties of the ANS, when we computed the group average transfer plots for the 10 male subjects and the 8 females separately, no significant differences could in fact be discerned.

The prominent dip in transfer magnitude for both postures below 0.1 Hz, seen in Figure 6.6a, must be interpreted carefully. The drop in coherence at very low frequencies evident in Figure 6.5c was quite reproducible from subject to subject, although the exact location of the

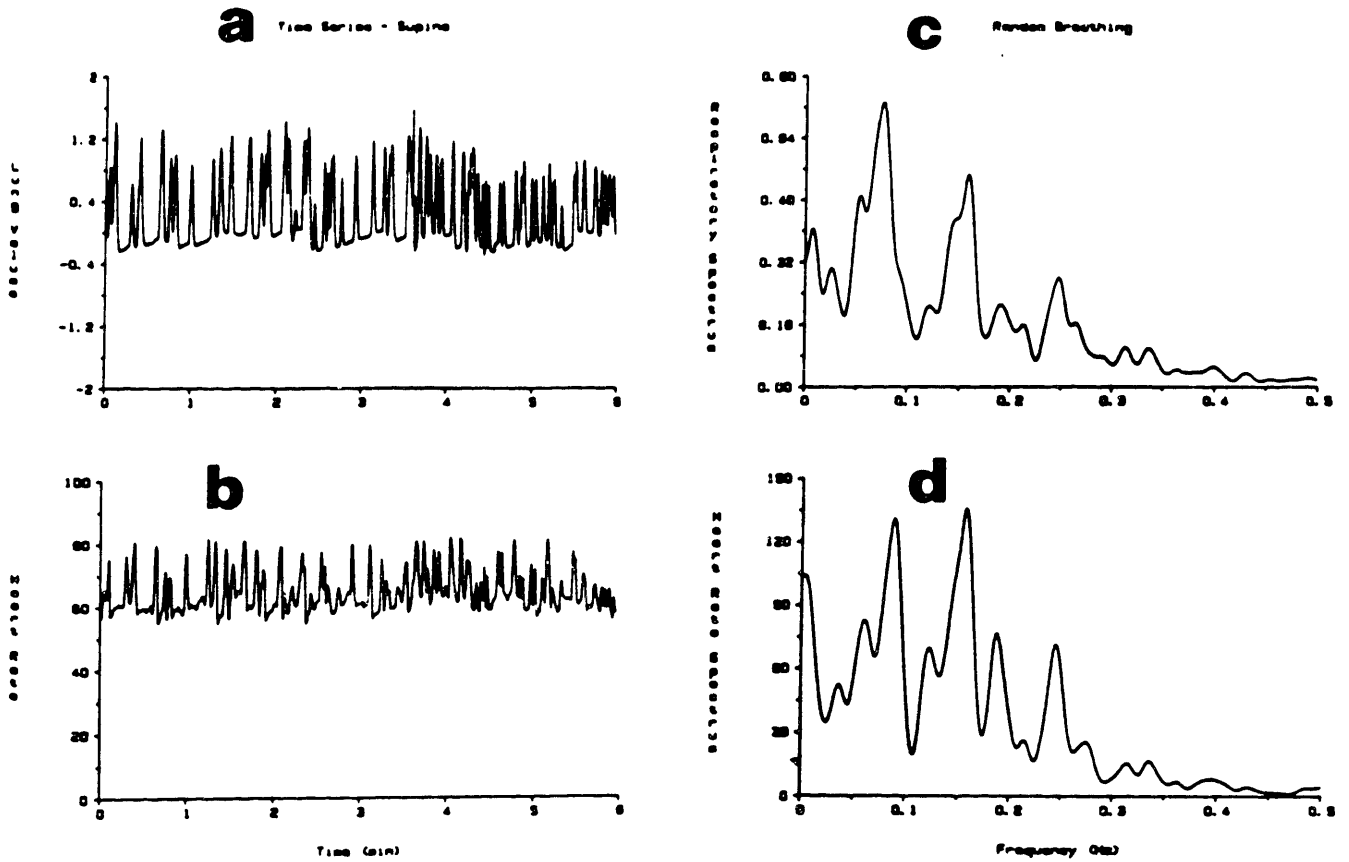


Figure 6.4. Representative six-minute time series of instantaneous lung volume (a) and heart rate (b) during random interval breathing, and their corresponding power spectra (c) and (d), respectively.

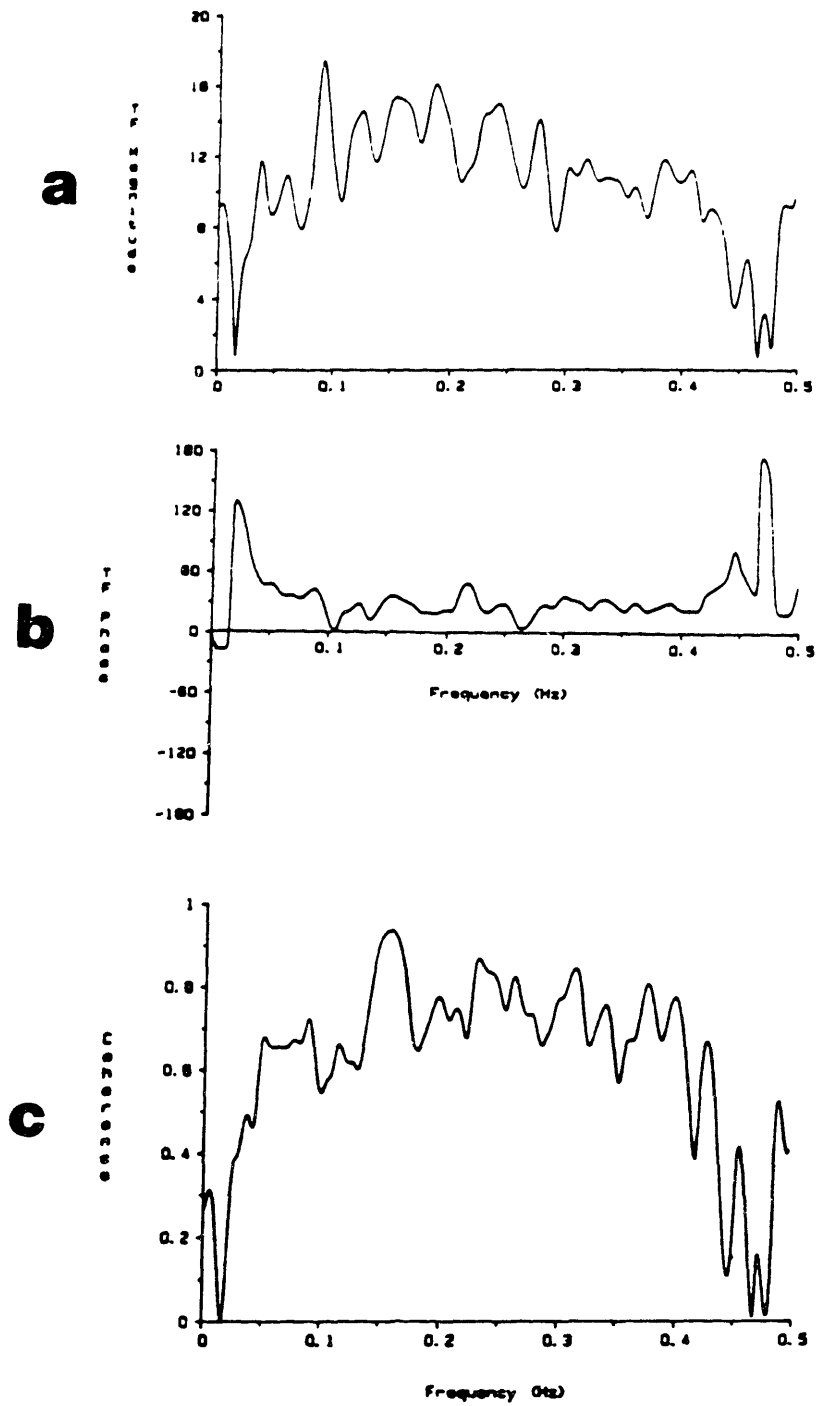


Figure 6.5. Transfer function magnitude (a) and phase (b) estimates for the experimental run shown in Figure 6.4, and the corresponding coherence function (c).

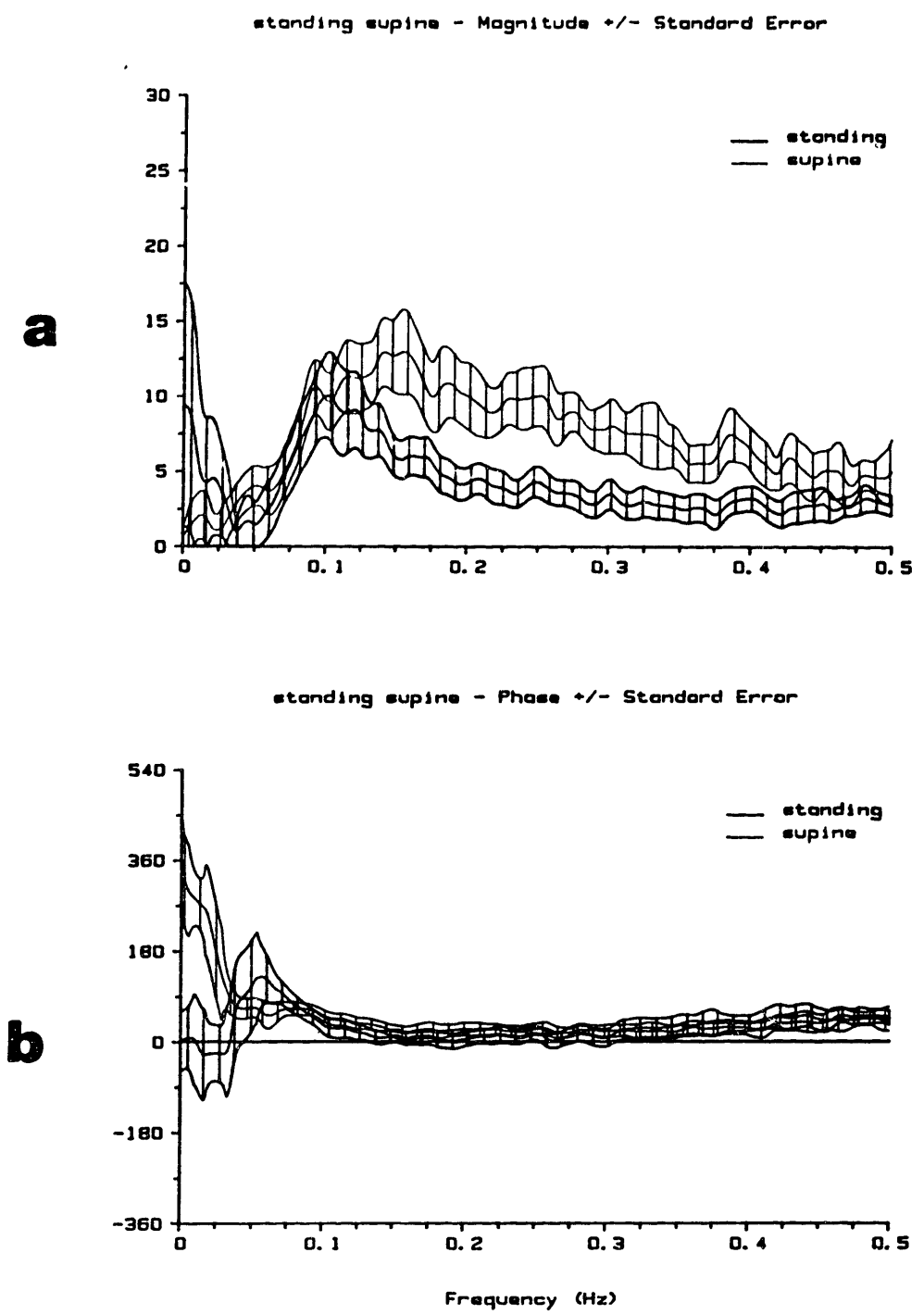


Figure 6.6. Group-average transfer function magnitude (a) and phase (b) plots for subjects breathing according to random-interval distribution. Figures include the group mean and error bars for subjects in both the supine and standing positions. The significance of the erratic behavior seen in these plots at frequencies below 0.1 Hz is discussed in the text.

coherence minima varied between nearly D.C. and 0.1 Hz. As a result of this poor coherence, not only were the error bars for the transfer function estimate widened at low frequencies, but the group average estimate itself was biased low. The latter effect stems from the way in which the group average is computed. As described in Section 4.5.3, the group average represents the mean vector when the individual transfer function estimates are plotted in the complex plane. When the coherence falls, however, the transfer phase randomizes from one subject to another, even if the transfer magnitude at that frequency were exactly identical for all subjects. The magnitude of the resultant mean vector for a set of vectors with identical magnitude but random phase is likely to be quite small. Hence, the group average transfer magnitude estimate is expected to be artifactually low in regions of reproducibly poor coherence.

Beyond 0.1 Hz, the group average magnitude plots for both postures fall gradually with frequency, although the curve for the standing position drops off sooner and then stays below that for the supine position. From 0.15 Hz to 0.4 Hz, these postural differences in autonomic response characteristics are statistically significant, as evidenced by the lack of overlap of the error bars for the two curves. Furthermore, the differences between the two curves can not be passed off as an artifact related to use of absolute lung volume and heart rate instead of percent changes in these variables as the input and output signals. When standing, the subject's mean heart rate generally rose from the supine level, making the percent change in heart rate smaller for the standing position than for supine, given identical amplitudes of fluctuations in absolute heart rate. Thus, were the transfer function estimates com-

puted using percent change in heart rate as the output variable, the postural differences in the transfer magnitude plots would appear even more significant than those seen here.

The group average phase characteristics for the two postures are shown in Figure 6.6b. Statistically significant differences between these two curves are absent except at frequencies below 0.05 Hz. Throughout most of the frequency band of interest, the phase lag for both postures is roughly zero, demonstrating synchrony between a rising heart rate and the inspiratory phase of respiration. Of note, however, many of the individual phase plots display progressively increasing lags as the frequency approaches zero, as in Figure 6.5b, suggesting the rise in heart rate may not always be synchronous with inspiration at very low rates of lung inflation.

6.4 Discussion

Despite the assertion by Womack [141] and Ahmed [1] that broad-band respiratory drive of the autonomic nervous system is unrealizable, the experiments described in this chapter demonstrate that the respiratory input signal can be easily modified to broaden its spectral content. These studies further show that the use of such maneuvers offers a means of efficiently and noninvasively assessing autonomic function. While the emphasis in the results presented above was on elucidation of physiologic mechanisms through averaging of data derived from a group of normals, we hope to refine the approach to allow reliable quantification of an individual's autonomic response characteristics from a single segment of random-interval breathing.

The most identifiable feature of the group average transfer function plots is the low-pass filter nature of the magnitude response curves for both supine and standing postures. This is not at all surprising, as a number of investigators have documented this phenomenon through describing function analysis [6,59,91]. However, to reiterate, the approach employed in those studies entailed making many test runs in which the subject breathed at one fixed frequency at a time. In fact, it was the greater efficiency of our technique that made it feasible for us to study postural differences in a subject in as little as a half-hour of recording, while describing function analysis may necessitate several hours of data acquisition to determine a single response curve.

The finding of accentuated transfer magnitude in the frequency band from 0.15 Hz to 0.4 Hz when supine as compared with standing is also not unexpected. Pomeranz et al [108] have shown that there is a relative shift in autonomic balance from sympathetic to vagal predominance in moving from the supine position to standing. Akselrod et al [3,4] showed that the vagus is capable of mediating heart rate fluctuations over a much broader frequency range than the sympathetic nervous system can, and the data presented in Chapter 5 of this thesis suggests that this phenomenon relates to the differential response of the SA node to fluctuations in tone along these two branches of the ANS. We therefore believe that the elevated transfer magnitude in the supine position for frequencies above 0.15 Hz reflects the greater participation by the fast-responding vagal system in mediating the heart rate response in this position compared with standing. It is of course possible that changes in thorax mechanics associated with shifts in posture exert some

direct influence on the transfer from lung volume to heart rate, masquerading as a shift in autonomic balance. Pharmacologic studies entailing selective β -sympathetic and parasympathetic blockade are required to test our hypothesis, as discussed in the following section.

Unfortunately, we were less successful in demonstrating posture-related differences in the group average transfer phase plots. In a few individual cases, we found that in the standing position the phase grew progressively negative with frequency, suggesting the presence of a delay in the system response. This finding is again in concert with the notion that the slow-responding sympathetic nervous system becomes dominant when the individual stands. The group average phase plots, on the other hand, displayed little deviation from zero for both postures, except for erratic variations below 0.1 Hz. At these low frequencies, however, the plotted curves are less reliable because of the consistently poor coherence found between respiration and heart rate. Nonetheless, these curves do suggest that the phase lag at very low frequencies of respiration may differ from the value of zero observed at frequencies above 0.1 Hz (particularly evident for the supine case). The implication here is that the common dogma that heart rate rises with inspiration may not always be correct. Several other investigators [6,31,42,83,91] have also found that the phase relationship of the respiratory sinus arrhythmia generally observed at normal respiratory frequencies (0.2 Hz - 0.3 Hz) changes as the respiratory rate falls, such that the rise in heart rate actually precedes inspiration.

While the poor coherence found at low frequencies on the one hand makes interpretation of the transfer magnitude and phase plots difficult

in that band, on the other hand the consistency of this finding is itself intriguing. It suggests either that the system includes a non-linear element that quite selectively affects a narrow band of frequency components, or that some influence uncorrelated with respiration overwhelms the respiratory effects on heart rate in that band. Certain nonlinearities in the effect of respiration on heart rate have been demonstrated by Kitney and coworkers [127,128]. However, we speculate that the poor coherence reflects the strong influence of low-frequency fluctuations in hemodynamic variables, such as arterial blood pressure, on heart rate control. In the following section, we describe follow-up studies, currently in progress, designed to address this and other issues.

6.5 Follow-up Studies

In the study conducted by Pomeranz et al [108], the effects of postural changes on the spectral pattern of spontaneous heart rate fluctuations were explained as due to shifts in autonomic activity, since high-frequency fluctuations normally present in the supine position could be abolished by parasympathetic blockade. Likewise, selective β -sympathetic blockade was found to reduce the power of low-frequency heart rate fluctuations when the subjects were standing, suggesting a relatively greater role of the sympathetics in cardiovascular regulation in this position.

We have initiated a study to explore the effects of selective pharmacologic blockade on the transfer function estimates obtained by broad-band respiration, using the same drug regimens that Pomeranz et al

used. Furthermore, in order to investigate the importance of blood pressure fluctuations on heart rate control, we measure arterial pressure via a radial artery catheter and record this signal along with respiration and ECG for off-line analysis. In this way, we can compute transfer function estimates between arterial pressure and heart rate, as well as between respiration and heart rate.

This study is being performed on paid volunteers, free of known cardiopulmonary disease, and has been approved by the M.I.T. Committee on Human Studies. The entire protocol takes less than two hours. After placement of surface ECG leads, plethysmographic belts, and the radial artery catheter, but before administration of drugs, random-interval breathing data is collected while the subject is first supine, then standing. The subject is randomized to either of two groups, denoted A and B. If he is in Group A, he first receives the parasympathetic blocking agent atropine (.03 mg/kg), after which he repeats the random-interval breathing routine in both postures. Next, he receives the β -sympathetic blocker propranolol (.2 mg/kg), and then breathes to the random-interval sequence in both postures for a third and final time. If he is in Group B, the protocol is identical except that the drugs are administered in reverse order. In this way, we observe all subjects in the baseline and double-blockade states, half in selective β -sympathetic blockade, and the other half in selective parasympathetic blockade.

The data from these studies has not yet been analyzed. We are obviously interested in examining the effects of selective autonomic blockade on the transfer magnitude and phase plots and comparing these effects to those of postural changes. Of greatest interest, however,

will be the level of the coherence function in the 0.05 Hz region between respiration and heart rate, as compared with that between blood pressure and heart rate. This analysis will hopefully help elucidate the relative influences of respiration and arterial pressure on heart rate control.

As a final note, we point out that the shifts in autonomic balance associated with postural changes are small compared with those seen in pathological states [44]. The results presented in this chapter, however, demonstrate that transfer function analysis is sufficiently sensitive to detect these subtle alterations in autonomic function, and could therefore presumably be at least as useful as a noninvasive tool to assess autonomic integrity in a variety of disease states. To that end, we are currently designing additional studies to compare the results of transfer function analysis using broad-band respiration on patients with diabetes, sick sinus syndrome, and hypovolemia (post-phlebotomy) with normals.

Chapter 7: Animal Model for Analysis of Autonomic Response

7.1 Introduction

In Chapter 5, we discussed the application of broad-band stimulation to the study of one effector organ of the cardiovascular control system, the sino-atrial node. In Chapter 6, a similar approach was employed to enable investigation of central neural mechanisms involved in the mediation of respiratory-induced heart rate fluctuations. While both of these studies demonstrated the utility of broad-band stimulation in the analysis of several key components implicated in cardiovascular regulation, neither addressed specifically the transfer properties of the system's feedback limb, i.e., the baroreflex.

In this chapter, we present an experimental preparation designed to allow characterization of the baroreflex in terms of transfer functions between arterial blood pressure and sinus node rate, and between arterial pressure and systemic vascular resistance. These experiments are performed on experimental animals instrumented with epicardial electrodes, aortic flow probe, and arterial cannulae. Although the data presented here was derived from a pilot study performed on an acutely anesthetized dog, these experiments may eventually be performed on fully conscious chronic animals previously instrumented using aseptic technique.

The anatomic elements involved in the baroreflex include the arterial baroreceptors, located in the aortic arch and carotid bifurcations, the autonomic nuclei of the brainstem, and the cardiovascular effector organs, particularly the SA node and the systemic arterial

resistance vessels. This network is schematized in Figure 2.5 and was discussed in detail in Chapter 2. In order to investigate the frequency response of the baroreflex using the transfer function analysis techniques introduced in Chapter 4, broad-band fluctuations must be imposed on the subsystem's input signal, namely the arterial blood pressure.

In previous attempts to characterize the dynamic response of the baroreflex, investigators have employed servo-mechanisms to impose sinusoidal oscillations on the arterial pressure [49,89,93,118,122,123,125,129]. Although these studies led to the computation of describing functions, the technique could be modified to enable estimation of transfer functions if broad-band fluctuations were applied instead of sinusoids. It is somewhat difficult to generate an arbitrary waveform using a mechanical servo-system, however, due to the inherent low-pass filter characteristics of such systems.

Our approach toward generating broad-band fluctuations in arterial pressure is through modulation of the ventricular activation rate. Although changes in ventricular rate only indirectly elicit blood pressure fluctuations, this approach offers two advantages over the mechanical methods discussed above. First, the experimental apparatus required is much simpler. All that are needed to control the ventricular rate are two ventricular epicardial pacing electrodes and the pulse train generator described in Chapter 5 for vagal and sympathetic nerve stimulation. The other benefit of ventricular rate modulation is that it allows for characterization of the feedforward limb of the cardioregulatory system as well as the feedback path. That is, not only may we observe the effects of blood pressure fluctuations on SA nodal rate and

peripheral resistance, but we can measure the transfer function between ventricular rate and arterial pressure, as well.

Regulating ventricular activations while trying to measure reflexogenic changes in SA nodal rate poses an interesting difficulty, however. If the atrial activations were to conduct through the atrioventricular junction (AVJ), then we would lose control over the timing of ventricular activations, since conducted beats may either interpolate between paced beats or render the ventricular myocardium refractory to exogenous pacing. Furthermore, waves of myocardial depolarization elicited by the pacing spikes may conduct retrograde through the AVJ, thereby activating the atria and confounding our measurement of SA nodal rate. Both of these problems can be avoided by ablation of the AVJ. A variety of techniques exist to achieve atrioventricular blockade [14,69,132,138], and the method we employ is described in the Methods section. Once the AVJ is blocked, then the baroreflex heart rate control loop is opened and transfer functions characterizing the feedforward and feedback limbs of the system may be determined independently.

The analysis of baroreflex-mediated changes in peripheral resistance is somewhat more complicated, however. The system's input signal, arterial pressure, depends critically on the output, instantaneous systemic vascular resistance, and it is impossible to decouple the two without surgically rerouting the cardiac output through an extracorporeal circuit. If we make appropriate assumptions, however, we can deduce the transfer properties of the feedback limb specifically (i.e., from blood pressure to vascular resistance), even though our measurements are derived from a necessarily closed-loop system.

Figure 7.1 shows a block diagram of vascular resistance regulation mediated by the baroreflex. This model represents a portion of the more complete system depicted in Figure 2.5. The neural components that comprise the feedback limb are represented as a "black box" whose transfer function $H(f)$ we wish to estimate. In order to compute $H(f)$, we need to know both the input and output signals, $x(t)$ and $y(t)$ respectively. $x(t)$ is the arterial pressure, which we measure directly. $y(t)$ represents instantaneous systemic vascular resistance, which Figure 7.1 depicts as the quotient between pressure $x(t)$ and the aortic flow $w(t)$. This relationship represents a simplification, in which we consider fluctuations in arterial resistance to occur over a time scale that is long compared to the duration of the impulse response of the arterial tree (i.e., at frequencies below roughly 0.1 Hz). The derivation of this relationship is as follows.

If we assume a Windkessel model of the arterial tree, then the vasculature may be modeled as a complex impedance load that includes a resistor and a capacitor, as shown in Figure 2.2. Rewriting equation (2.2) in terms of the pressure $x(t)$, flow $w(t)$, vascular resistance $y(t)$, and vascular capacitance C (assumed constant), we obtain the relation,

$$\frac{dx(t)}{dt} + \frac{x(t)}{Cy(t)} = \frac{w(t)}{C}. \quad (7.1)$$

Rearranging terms and averaging over a time period from t_1 to t_2 , we get

$$\frac{1}{T} \int_{t_1}^{t_2} x(t) dt = \frac{1}{T} \int_{t_1}^{t_2} y(t)w(t) dt - \frac{1}{T} \int_{t_1}^{t_2} Cy(t) dx(t), \quad (7.2)$$

where $T = t_2 - t_1$. If during the period of integration $t_1 \leq t \leq t_2$ the

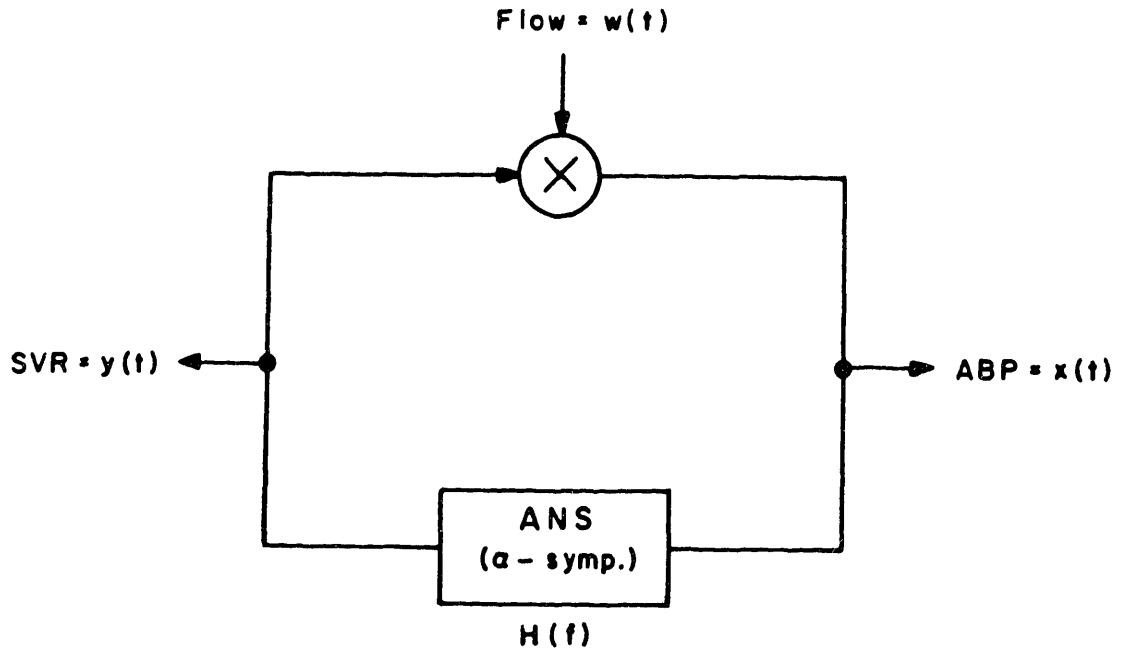


Figure 7.1. Block diagram model of baroreflex control over systemic vascular resistance (SVR). Note that the feedforward relationship between resistance and arterial blood pressure (ABP) is depicted as multiplicative, while the feedback behavior is mediated by the autonomic nervous system (ANS).

resistance $y(t)$ remains virtually constant, then equation (7.2) may be approximated

$$\begin{aligned} \frac{1}{T} \int_{t_1}^{t_2} x(t) dt &\approx \frac{Y(t)}{T} \int_{t_1}^{t_2} w(t) dt - \frac{CY(t)}{T} \int_{t_1}^{t_2} dx(t) \\ &\approx \frac{Y(t)}{T} \int_{t_1}^{t_2} w(t) dt - \frac{CY(t)}{T} [x(t_2) - x(t_1)]. \end{aligned} \quad (7.3)$$

Now, if $Cy(t)/T \ll 1$ or if we choose the time limits of integration, t_1 and t_2 , such that $x(t_2) \approx x(t_1)$, then we have

$$y(t) \approx \frac{\int_{t_1}^{t_2} x(t) dt}{\int_{t_1}^{t_2} w(t) dt}. \quad (7.4)$$

To recapitulate, the instantaneous vascular resistance $y(t)$ can be derived as the quotient of the time-averaged arterial pressure $x(t)$ and aortic flow $w(t)$ signals, given that the following assumptions are valid:

- (1) The vascular capacitance C is a constant.
- (2) The instantaneous vascular resistance $y(t)$ is virtually constant for the period of integration $t_1 \leq t \leq t_2$.
- (3) Either $Cy(t)/T \ll 1$ or the instantaneous arterial pressure at the beginning of the period of integration is essentially the same as at the end, i.e., $x(t_2) \approx x(t_1)$.

We choose the period of integration to span from one R-wave of the surface ECG to the next. The value of $y(t)$ then found using equation (7.4) is taken to represent the instantaneous vascular resistance for the duration of that RR interval. We may now consider whether or not each of the above assumptions is reasonable. The first assumption is

the most tenable. Vascular capacitance is known to remain essentially constant from minute to minute, even from day to day, and decreases only very slowly with age [100].

Changes in resistance, mediated through modulation of α -adrenergic tone, are also known to take place slowly compared to the typical RR interval [100], so that the second condition above also appears satisfied. On the other hand, any fluctuations we might find in the derived signal $y(t)$ at frequencies within an order of magnitude of the mean heart rate (e.g., beyond roughly 0.1 Hz) must be interpreted cautiously, since they would obviously be inconsistent with the assumption of a slowly varying vascular resistance.

The validity of the third assumption is the least certain. The right-most term in equation (7.3) will become significant if the difference in arterial pressure between the limits of integration is comparable to the induced beat-to-beat fluctuations in pressure and if the mechanical time constant $Cy(t)$ is comparable to the length of integration T . Since the latter is true, especially at high ventricular rates, the importance of this term depends critically on the change in instantaneous pressure from one R-wave to the next. Methods to avoid this difficulty are considered in the Discussion section.

Note that the reliability of equation (7.4) depends not only on the validity of the three assumptions mentioned above, but also on how well the Windkessel model represents the mechanical properties of the arterial tree. For instance, in order to account for any inductive effects of the vasculature or for the effects of a distributed capaci-

tance, higher-order terms would have to be added to equation (7.1), which would obviously complicate the derivation of equation (7.4).

Once the instantaneous resistance signal $y(t)$ has been derived, $H(f)$ is found using the statistical techniques described in Chapter 4. Note that the feedback relation that enables us to compute $H(f)$ from the cross-spectrum $S_{xy}(f)$ and input autospectrum $S_{xx}(f)$,

$$H(f) = \frac{S_{xy}(f)}{S_{xx}(f)}, \quad (7.5)$$

is neither redundant nor inconsistent with equation (7.4), which defines only the feedforward relation between $y(t)$ and $x(t)$ in Figure 7.1.

7.2 Methods

A 15 kg adult mongrel dog, anesthetized with sodium pentobarbital (30 mg/kg), was instrumented using non-sterile technique. The thoracic cavity was exposed through an incision in the fourth right intercostal space, while ventilation was maintained at 15 breaths/min and 5 cm of positive end-expiratory pressure (PEEP) using a Harvard Apparatus model 607 respirator. A .04 inch inner diameter Tygon catheter was inserted in the descending aorta using the Herd-Barger technique [57] and connected to a Statham model P23ID transducer to enable measurement of arterial pressure. Fat and connective tissue surrounding the ascending aorta were excised without trauma to the vessel wall, and a 16 mm ultrasonic flow probe (Transonics, Inc.) was implanted around the vessel. A pair of Medtronic model 4951 epicardial electrodes was placed on the right atrial appendage, and a second pair was placed on the left ven-

tricular free wall, with care to avoid traumatizing the coronary vessels. These allowed for measurement of an atrial electrogram while either monitoring a ventricular electrogram or pacing the ventricles exogenously. To decouple atrial and ventricular electrical activity from each other, as discussed above, 10% formalin was injected through a 23-gauge needle inserted in the AVJ, using the technique described by Steiner and Kovalik [132]. After injection of .3 cc formalin, complete atrioventricular block was achieved, as determined by simultaneous observation of the atrial and ventricular electrograms. Alligator clip electrodes were also placed on the skin on either side of the chest to allow measurement of the surface ECG. All signals were amplified and displayed on a Honeywell model VR-16 multichannel monitor and recorded on a Hewlett Packard model 3968A FM tape machine to enable off-line analysis.

A Gaussian white noise frequency modulated (GWNFM) train of pulses was used as the ventricular pacing waveform in order to produce broadband hemodynamic fluctuations. The computer-implemented algorithm used to generate this pulse train was described in Chapter 5. The computer's digital-to-analog (D/A) output was fed into a voltage-to-current converter, the schematic of which was shown in Figure 5.3. The output of the latter device was then connected to the ventricular epicardial electrodes. Six-minute segments of GWNFM ventricular pacing were recorded at mean pacing rates of 1.5 Hz and 3.0 Hz (90 bpm and 180 bpm, respectively). The Gaussian white noise modulator waveform included energy between D.C. and 0.7 Hz.

Off-line analysis started with sampling of all recorded signals at

360 Hz. The times of atrial activations were then determined from the atrial electrogram and of ventricular activations from the surface ECG, using a peak detection algorithm. Instantaneous vascular resistance was computed, as described above, from the undecimated arterial pressure and flow signals, using the times of ventricular activations as the limits of successive periods of integration in equation (7.4). Instantaneous atrial and ventricular activation rates were derived using the algorithm described in Section 4.3. These rate signals, as well as the instantaneous vascular resistance signal, were computed at time intervals of 0.3556 sec, or at a presentation rate of 2.8125 Hz. Decimated versions of the arterial pressure and aortic flow signals were obtained at the same presentation rate, as well.

Power spectra of the instantaneous ventricular and atrial rate signals, the arterial pressure and flow, and the instantaneous vascular resistance were computed using the estimation techniques outlined in Section 4.4. Using the approach described in Section 4.5, transfer and coherence functions were then computed for each six-minute experimental run for the following pairs of signals:

- (1) ventricular rate to arterial pressure,
- (2) arterial pressure to atrial rate, and
- (3) arterial pressure to systemic vascular resistance.

7.3 Results of Pilot Study

A 10-second strip reproduced from the multichannel monitor, showing the atrial electrogram, surface ECG, aortic flow, and arterial blood pressure during GWNFM ventricular pacing, is displayed in Figure 7.2.

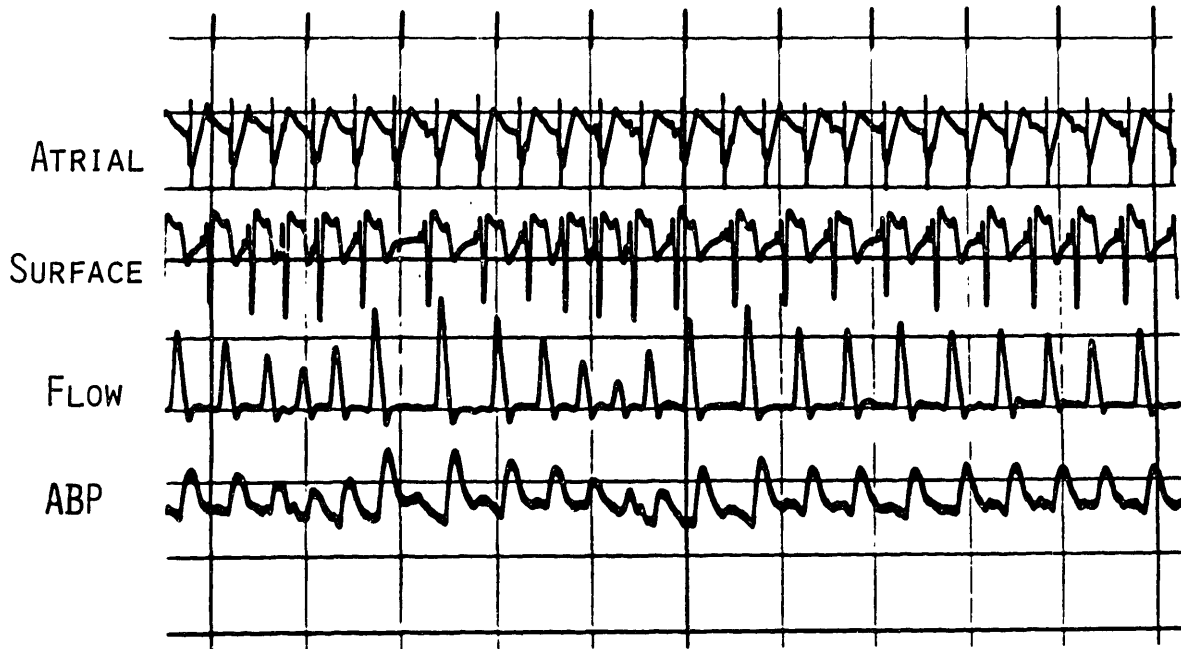


Figure 7.2. 10-second strip reproduced from multichannel recording made during GWNFM ventricular pacing. The tracings depict (from top to bottom) the atrial electrogram, the surface ECG, aortic flow, and arterial pressure.

We see in the surface ECG that each ventricular activation occurs shortly after a tiny pacing artifact, and that these activations are entirely decoupled from the atrial activity seen in the top trace. This establishes the presence of atrioventricular blockade. Furthermore, it is clear that pacing the ventricles in this fashion does indeed elicit erratic fluctuations in arterial pressure, but that the diastolic level of the pressure waveform is quite similar from one R-wave of the ECG to the next.

Figure 7.3 shows a 6-minute record of the derived ventricular and atrial rate signals, the filtered and decimated arterial pressure and flow signals, and the derived peripheral vascular resistance signal during GWNFM ventricular pacing at a mean rate of 90 bpm. Again, these time series are obtained at a presentation rate of 2.8125 Hz, so the 364-second record includes 1024 points of each signal. The effects of GWNFM pacing are evident in the instantaneous ventricular rate signal. The resulting fluctuations seen in the arterial pressure and flow traces should be interpreted carefully. Since these signals are digitally low-pass-filtered with a cutoff frequency of 1.4 Hz and then decimated to a sampling rate of 2.8125 Hz, most (but not all) of the phasic variations associated with ventricular contractions have been removed. Consequently, only the mean and lower frequency fluctuations remain in these time series. One can see that the mean arterial pressure is about 80 mm Hg, and the mean aortic flow is roughly 2 L/min. Consistent with these values, the instantaneous vascular resistance hovers around 40 mmHg min / L. Although the atrial rate shows some variability, much of the baroreflex-mediated response has been blunted by the vagolytic

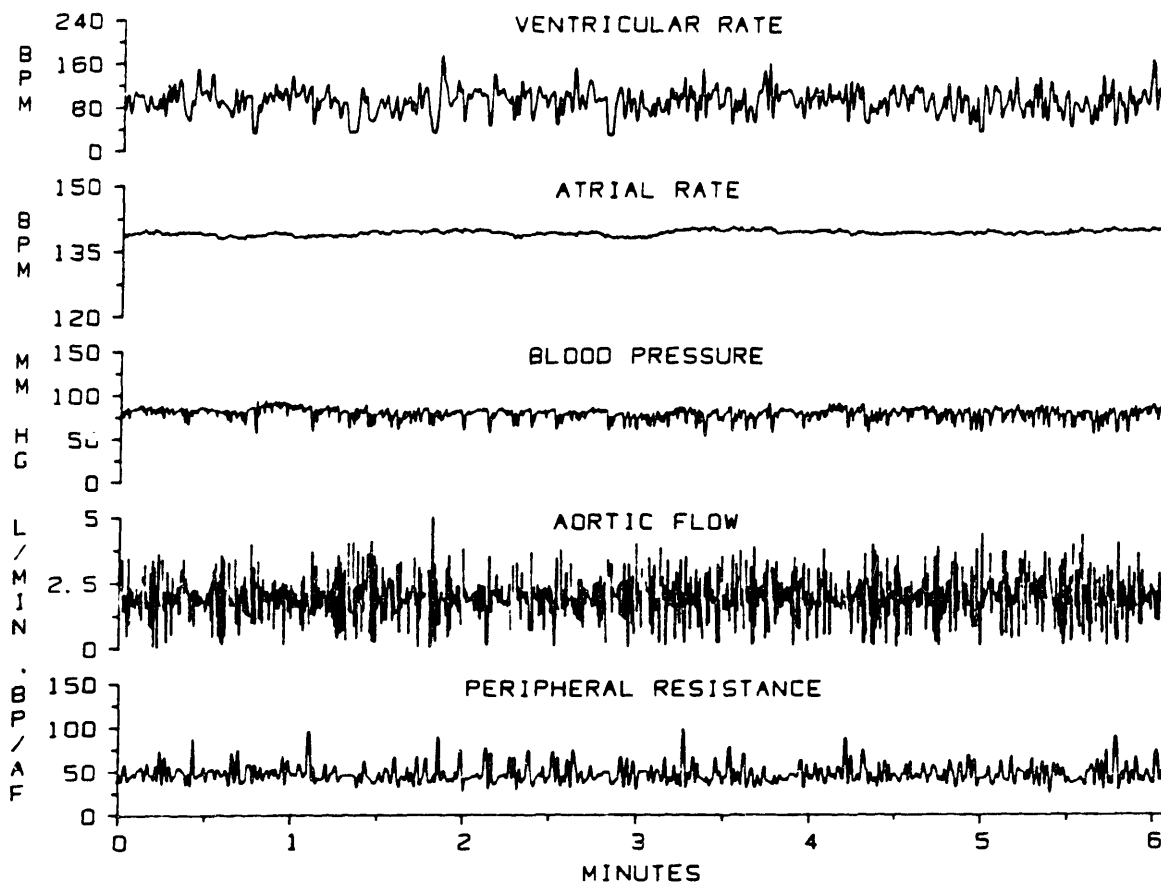


Figure 7.3. Six-minute record of instantaneous ventricular rate, atrial rate, arterial pressure, aortic flow, and systemic vascular resistance obtained during GWNFM ventricular pacing at a mean rate of 90 bpm. The sampling rate for these signals is 2.8125 Hz.

effect of the pentobarbital anesthesia. This will be discussed further below.

The corresponding power spectral density functions for these five signals are shown in Figure 7.4. The ventricular rate spectrum shows that the modulator signal used in controlling the pacing rate contains energy between D.C. and 0.7 Hz. The arterial pressure and vascular resistance spectra demonstrate the presence of energy within the same band in these signals. The aortic flow spectrum reveals the wide-band nature of fluctuations in flow associated with ventricular contractions that remain even after low-pass filtering. The spectrum of atrial rate fluctuations, on the other hand, is essentially limited to the region below 0.1 Hz.

The transfer magnitude and phase plots and the coherence function characterizing the effect of ventricular rate changes on the arterial pressure are shown in Figure 7.5. These plots were derived from the time series of Figure 7.3. We see that blood pressure fluctuations are indeed linked to those in ventricular rate, as the coherence function maintains a level greater than 0.5 for most of the band from 0 to 0.7 Hz. The transfer magnitude plot demonstrates the broad band-pass quality of the mechanical system that couples ventricular activity to arterial pressure. Interestingly, the phase falls almost linearly with increasing modulation frequency at a rate of roughly 150 degrees/Hz, consistent with a 0.42 second delay. Note that the phase approaches zero at D.C., suggesting that in the quasistatic case, arterial pressure moves in the same direction as ventricular rate.

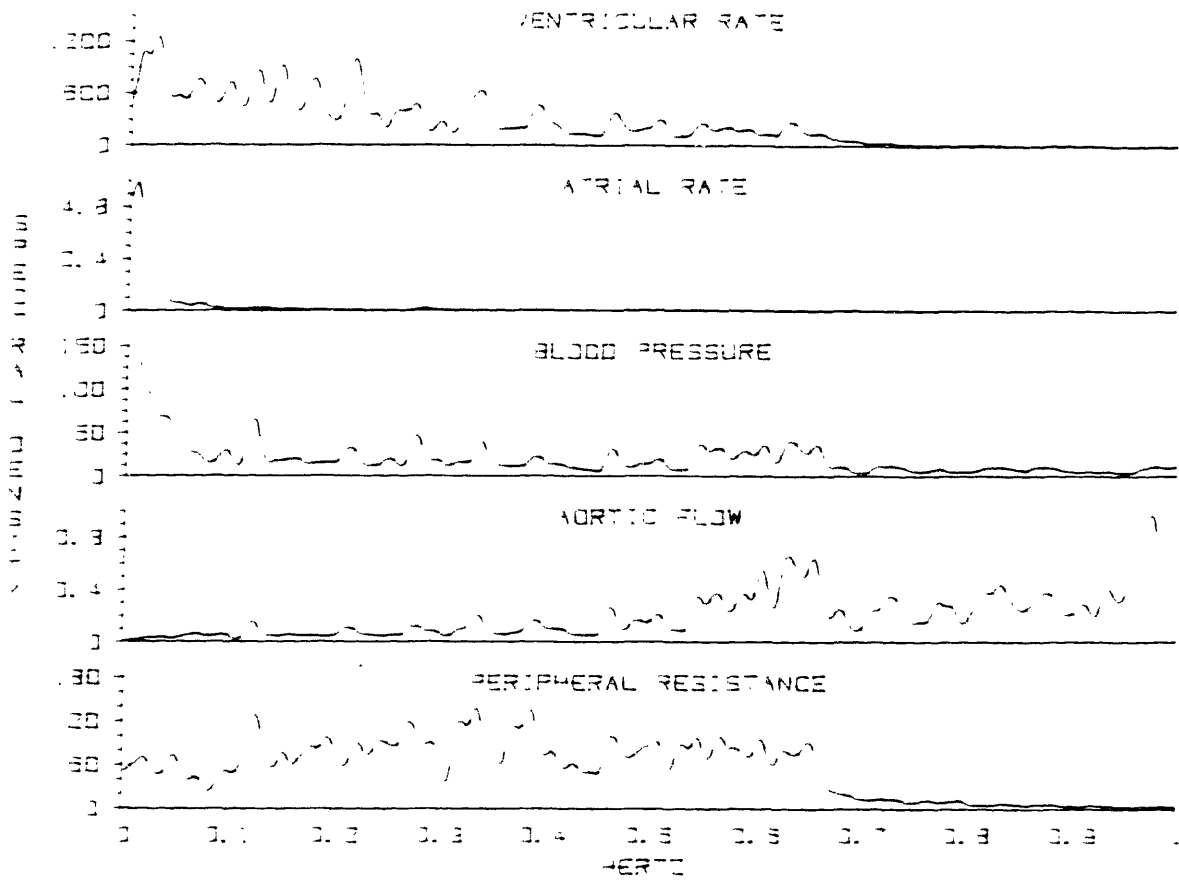


Figure 7.4. Power spectra of signals shown in Figure 7.3. Note that the modulator waveform used to control the GWNFM pacing spikes contained power between 0.0 and 0.7 Hz.

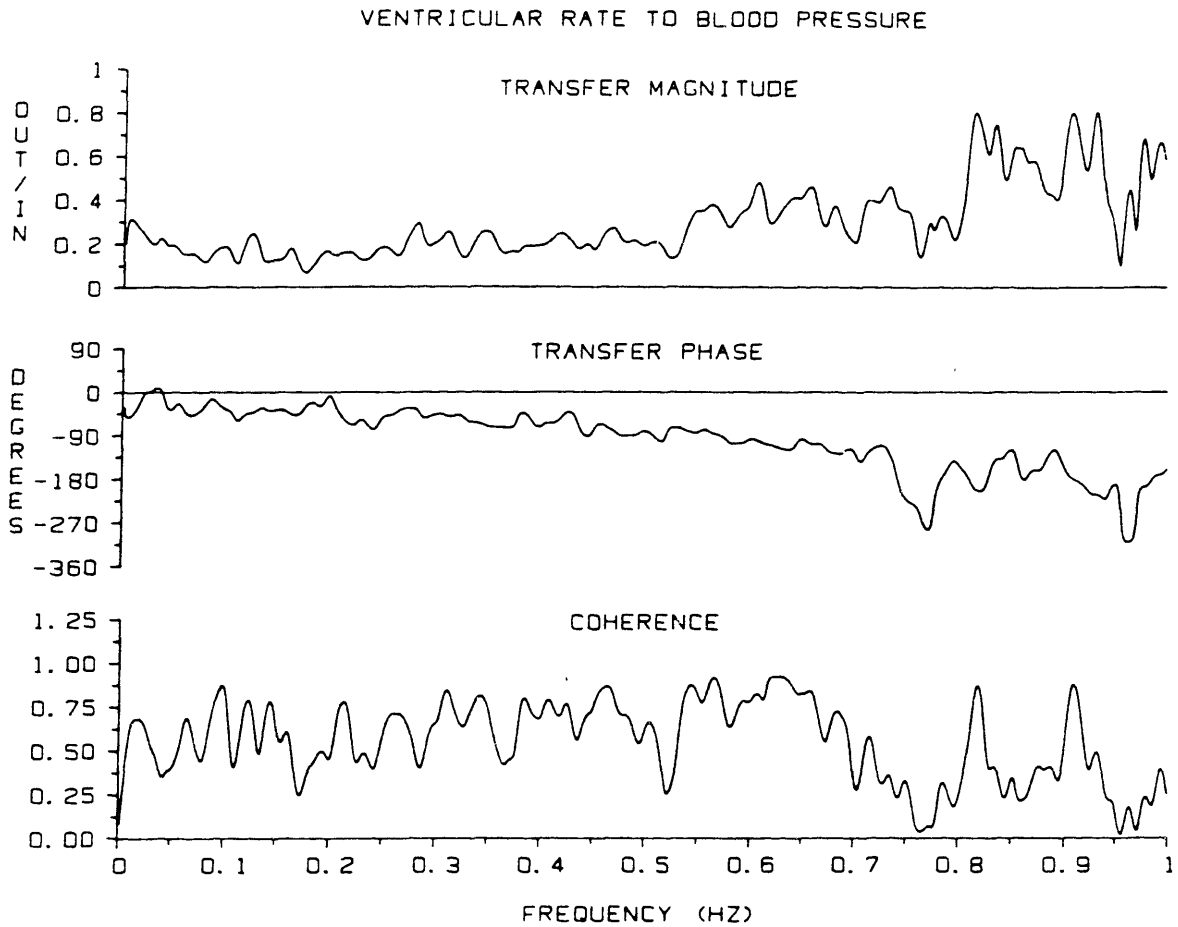


Figure 7.5. Transfer magnitude, phase, and coherence function between instantaneous ventricular rate and arterial pressure derived from signals in Figure 7.3. Note good coherence, nearly linear phase, and broad pass-band.

Transfer magnitude, transfer phase, and coherence plots for the same input and output variables as in Figure 7.5, but derived from a record where the mean pacing rate was 180 bpm, are shown in Figure 7.6. The coherence and transfer magnitude plots here are similar to those in Figure 7.5. Furthermore, the phase function shows a linear decline with frequency, as in Figure 7.5. However, as the modulation frequency nears D.C., the phase here approaches 180 degrees, in sharp contrast with the situation in Figure 7.5. Indeed, when this experimental run was performed, we noted that the arterial pressure fell as the ventricular rate rose, and vice versa. This phenomenon reflects a decline in ventricular filling due to shortening of the diastolic phase that accompanies such high heart rates.

We return now to the analysis of signals from the first 6-minute record. Transfer and coherence function plots between arterial pressure and SA nodal rate are shown in Figure 7.7. The coherence here is poor, the phase difficult to interpret, and the transfer magnitude falls almost to zero by 0.1 Hz. All of these attributes stem from the failure of the autonomic nervous system to elicit a rapid or significant change in SA nodal rate, due to the inhibitory effect of pentobarbital on the production of vagal tone. In fact, our inability to observe the normal SA nodal response to blood pressure fluctuations constitutes the greatest limitation of the anesthetized animal preparation. Alternative approaches that avoid this difficulty are considered in the Discussion section.

Finally, transfer function and coherence plots for the vascular resistance control limb of the baroreflex are shown in Figure 7.8. The

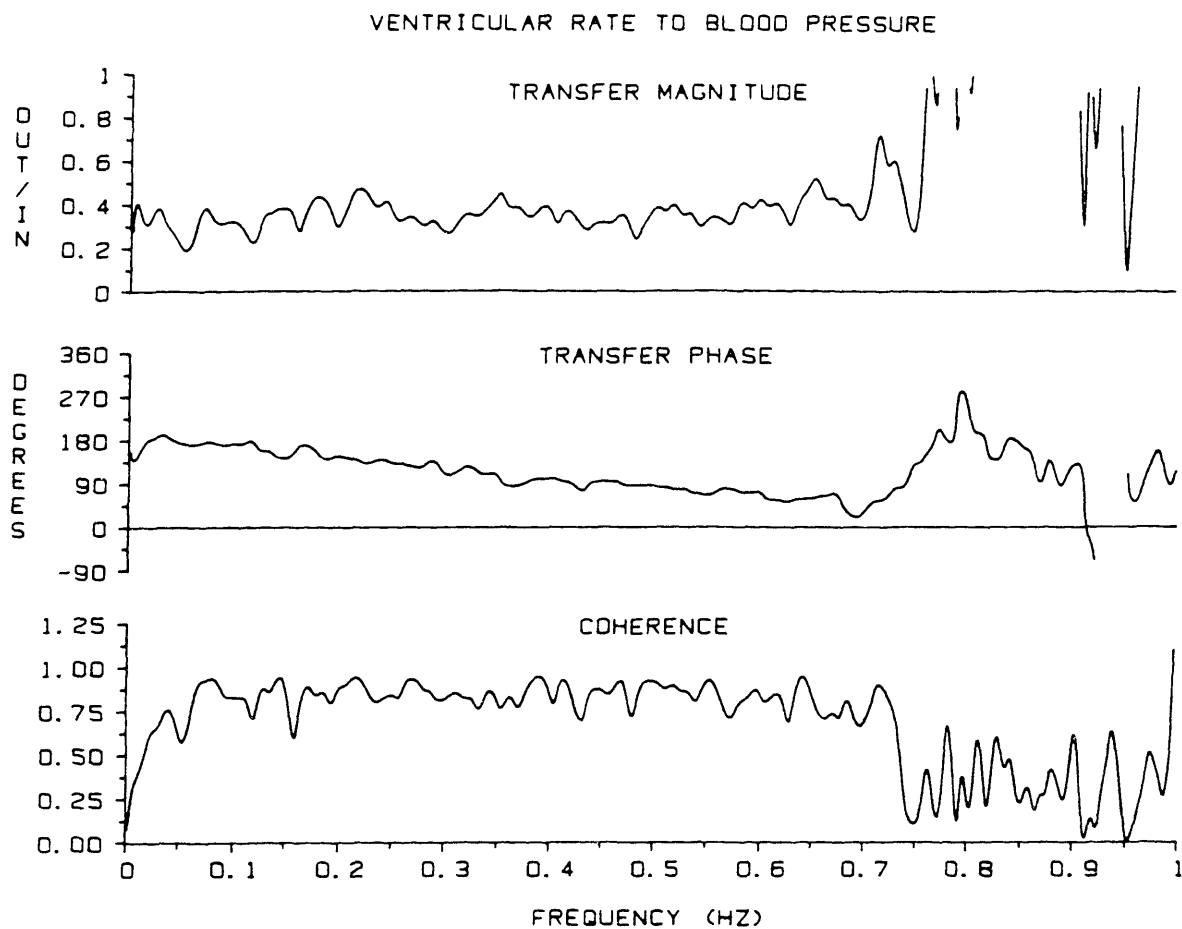


Figure 7.6. Transfer and coherence functions between ventricular rate and arterial pressure, as in Figure 7.5, but derived from a record where the mean pacing rate was 180 bpm. Note similarities with Figure 7.5, except for 180 degree difference in phase characteristic.

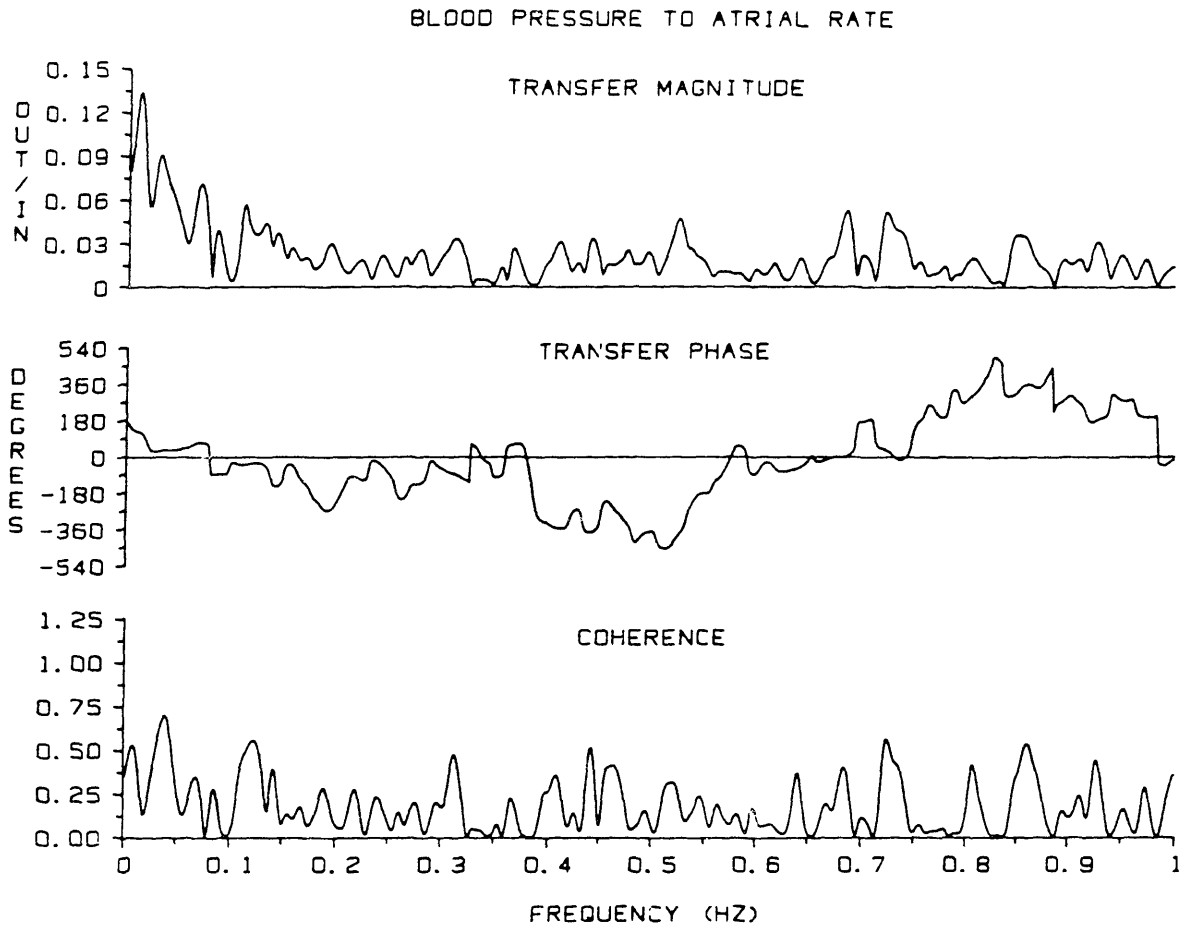


Figure 7.7. Transfer magnitude, phase, and coherence plots between arterial pressure and instantaneous atrial rate, derived from signals in Figure 7.3. Reasons for the poor coherence and difficulty in estimating the transfer function are discussed in the text.

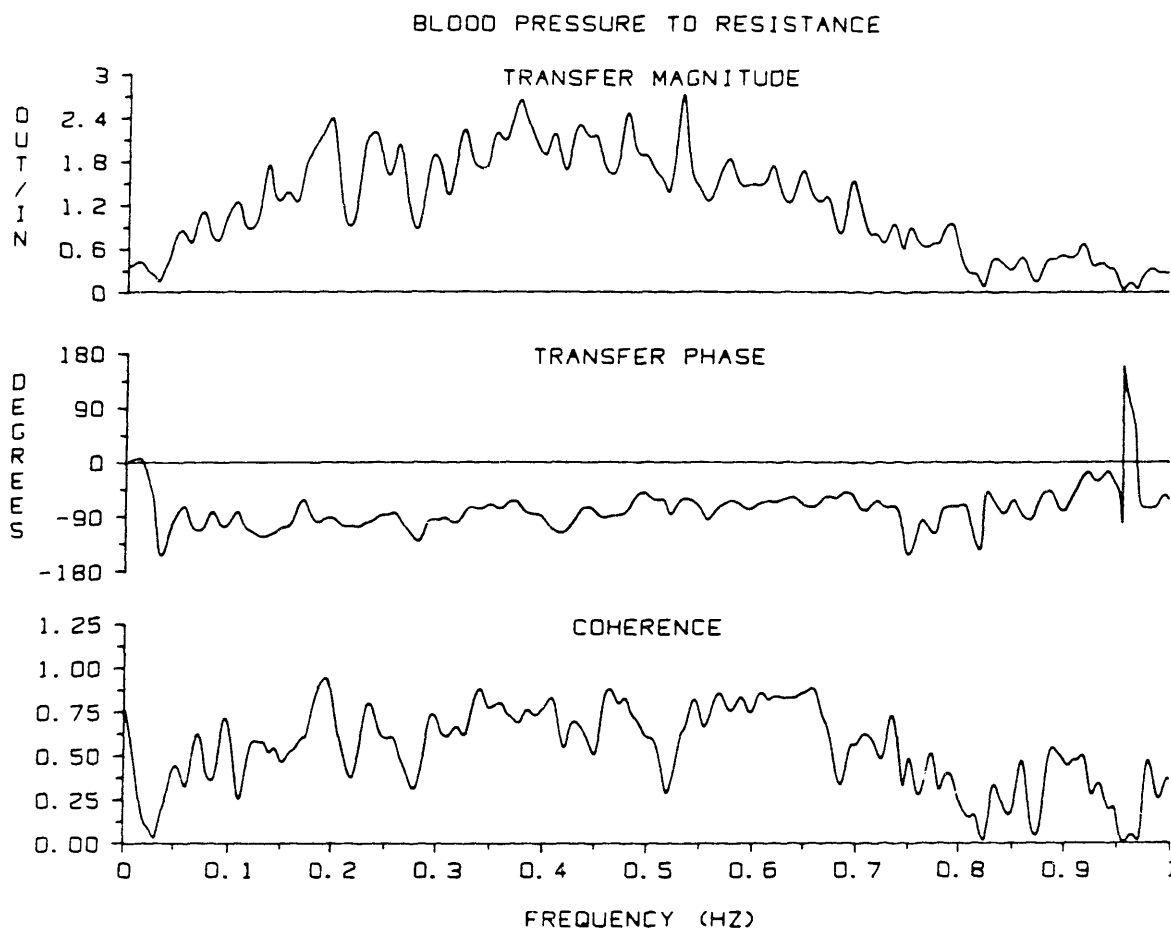


Figure 7.8. Transfer magnitude, phase, and coherence plots between the arterial pressure and derived instantaneous vascular resistance signals shown in Figure 7.3. The significance of the dome-shaped transfer magnitude plot is discussed in the text.

coherence between arterial pressure and the derived resistance signal is remarkably good in the band of significant input excitation (D.C. to 0.7 Hz), except for a narrow dip at frequencies below 0.05 Hz. While the phase function hovers around -90 degrees with little dependence on modulation frequency, the transfer magnitude appears to wax gradually between D.C. and 0.4 Hz and then taper off slowly. However, as was pointed out in the introductory section, fluctuations in the derived peripheral resistance signal at frequencies beyond roughly 0.1 Hz are probably artifactual, so that the transfer function between arterial pressure and vascular resistance can not be interpreted at higher frequencies. In fact, the coherence function must also be interpreted carefully, since the instantaneous resistance signal is derived from the arterial pressure trace. Spurious fluctuations in pressure that are unrelated to changes in the true vascular resistance may corrupt the computed resistance signal, and lead to factitious elevation of the coherence function.

Transfer and coherence plots for arterial pressure to atrial rate and for arterial pressure to vascular resistance have been omitted for the record where the mean pacing rate was 180 bpm. The coherence between blood pressure and atrial rate was no better for this record than for the one shown, so the corresponding transfer function plots reveal little. Furthermore, because of the high pacing rates in this experimental run, the ventricular activations often occurred in mid-systole. As a result, the arterial pressure was often quite different from one R-wave to the next, thereby rendering the vascular resistance signal artifactually noisy. Transfer function analysis of this record,

using instantaneous vascular resistance as the output variable, was thus unrewarding.

7.4 Discussion and Proposal for Conscious Animal Model

Although the data we present in this chapter is derived from just a single pilot study, the experimental approach demonstrates the usefulness of broad-band excitation in studying the behavior of the autonomic nervous system. The presence of significant energy in the arterial pressure waveform over the entire band of physiologically important frequencies (D.C. to 0.7 Hz) facilitated characterization of the baroreflex. Previous efforts to evaluate the transfer properties of this system by Kenet [80], Kalli et al [73,74], and Pagani et al [11,12,103] were hampered by the lack of broad-band signal content in the spontaneous hemodynamic fluctuations these investigators used as the basis of their analyses.

Our approach represents an extension of the techniques described by Taylor [133] and Ringo et al [112]. These workers introduced frequency modulated cardiac pacing as a means to broaden the spectral content of hemodynamic signals. They, however, employed atrial pacing in their experiments and were thus unable to study the effects of their interventions on the regulation of SA nodal rate. Instead, they focused entirely on the mechanical properties of the arterial tree. Similarly, Rosenbaum and Race [116] investigated the response characteristics of arterial resistance vessels using frequency-modulated pulse trains applied to muscle sympathetic nerve fibers, but ignored the influence of autonomic regulation on the vasculature. Our use of ventricular pacing

and introduction of complete AV block has enabled us to examine both the feedforward and the feedback limbs of the heart rate control system in an open-loop preparation. Furthermore, although we could not develop an analogous open-loop preparation to study the control of vascular resistance, we were able to derive the transfer properties of this branch of the baroreflex through signal processing techniques.

The transfer characteristics of the mechanical system that couples ventricular activity to arterial blood pressure (Figures 7.5 and 7.6) reveal an important attribute of the cardiovascular system. Fluctuations in ventricular rate were found to elicit similar changes in arterial pressure with almost no dependence on their frequency, with a fixed delay of roughly 420 msec, and with only the direction of the response dependent on the mean pacing rate. These features make GWNFM ventricular pacing a particularly attractive approach toward imposing broad-band fluctuations in blood pressure. By comparison to previous efforts in our laboratory to impose pressure fluctuations by variable inflation of an aortic cuff, GWNFM ventricular pacing is much simpler to implement and provides at least as good control over the arterial pressure waveform.

It is somewhat difficult to evaluate the significance of our findings regarding the autonomic regulation of the arterial vasculature. As we indicated in the Results section, only at frequencies below roughly 0.1 Hz does the transfer function between arterial pressure and the derived vascular resistance signal have any meaning. Since the coherence function in Figure 7.8 was best between 0.1 Hz and 0.7 Hz, however, we believe the instantaneous resistance signal shown in Figure 7.3 was

largely contaminated with artifacts resulting from small but significant differences in arterial pressure from one R-wave to the next. In future work, we will attempt to improve the estimation of instantaneous resistance by modifying the algorithm presented in the introductory section. Instead of defining the limits of integration in equation (7.4) to be successive R-waves of the surface ECG, we will program the computer to search for temporal locations such that the arterial pressure trace is exactly the same at the beginning and end of the integration period. This will guarantee that the third term in equation (7.3) will be zero, thereby removing the largest source of error in equation (7.4). Of course, once again, the success of this approach will depend critically on the validity of the Windkessel model in portraying the mechanical properties of the arterial tree. Alternatively, a more general solution would involve extending the period of integration to a length of time that is large compared to the mechanical time constant of the system, or equivalently applying any suitable low-pass-filter to the instantaneous pressure and flow signals that has a cutoff frequency below 0.1 Hz. This would again make the third term in equation (7.3) small, but represents an essentially "brute force" method of removing spurious high frequency components from the derived resistance signal.

In Chapter 2, the phenomenon of low frequency (0.05 to 0.1 Hz) oscillations in arterial pressure, called Mayer waves, was discussed. These oscillations are known to appear spontaneously, particularly under conditions of hypovolemia such as after a significant hemorrhage [60,95], although their etiology remains mysterious. Two competing theories that have been offered to explain the origin of Mayer waves

are (1) the presence of a resonance or instability in the resistance control system and (2) the emergence of a central neural oscillator within the system [106,109]. It would be interesting, therefore, to follow the shape of the arterial pressure to vascular resistance transfer function while withdrawing blood from the experimental animal. If a peak were to develop in the transfer magnitude plot in the 0.05 Hz to 0.1 Hz region while the coherence remained high in that frequency band, then a system resonance might indeed be implicated in the genesis of Mayer waves. If, on the other hand, Mayer waves were to appear with hemorrhage while the transfer magnitude changed little and the coherence became poor near the frequency at which the oscillations occur, then the central neural oscillator theory would become a more tenable explanation for this phenomenon.

Note that the transfer function between arterial pressure and vascular resistance is a different characterization of the system than that used by Taylor [133] and Ringo et al [112]. These investigators instead computed the impedance modulus $Z(f)$ of the arterial tree using the relation,

$$Z(f) = \frac{S_{WX}(f)}{S_{WW}(f)}, \quad (7.6)$$

where $S_{WX}(f)$ is the cross-spectrum between aortic flow and arterial pressure, and $S_{WW}(f)$ is the autospectrum of the flow signal. The impedance modulus characterizes the mechanical properties of the arterial vessels, but provides only indirect information regarding the behavior of the resistance control limb of the baroreflex. Taylor, for instance, found that the impedance modulus falls sharply for frequencies

below 0.03 Hz, which he attributed to "the action of the baroreceptor reflex." He could not, however, unravel the specific contributions of the feedforward and feedback limbs of the blood pressure control system that give rise to the exact shape of the impedance modulus function. The transfer function analysis we employ, by contrast, enables us to characterize the baroreflex feedback limb as if it were isolated from the rest of the control loop.

We were obviously somewhat disappointed with our inability to examine normal autonomic regulation of SA nodal rate, due to the inhibitory effect of pentobarbital anesthesia on vagal tone. This was particularly frustrating in light of our success in developing an animal preparation specifically designed to allow for investigation of heart rate control, were it not for the confounding influence of the anesthesia. In particular, the use of AVJ blockade not only averts retrograde conduction of the ventricular pacing spikes, but also prevents fluctuations in SA nodal rate from influencing the ventricular rate. If antegrade conduction through the AVJ were left unblocked, then the ANS could work to counteract the very fluctuations in arterial pressure that we impose exogenously. This was precisely the difficulty encountered by Scher and coworkers [122,125], who attempted to impose sinusoidal fluctuations in pressure by cyclically inflating and deflating an aortic cuff, but left the AVJ intact.

In order to study heart rate regulation using the experimental approach outlined in this chapter, but avoiding the obstacles presented by the use of anesthesia, we intend to employ a conscious animal model. Note that the surgical preparation described in the Methods section

could just as well be performed using aseptic technique with all wires and catheters exteriorized through small skin incisions. Once having recuperated from the surgery, the dog could then be used for experimentation while fully conscious, since we have found that dogs are not at all disturbed by GWNFM ventricular pacing even in the awake state. The only added wrinkle in using chronic animals for these experiments is that exogenous ventricular pacing is required at all times, since complete heart block is only marginally compatible with life. A simple fixed-rate pacing device could easily be connected to the ventricular epicardial electrodes and placed in a pocket of the animal's jacket to support the circulation between experiments.

A conscious animal model will not only enable us to study the normal mechanisms involved in baroreflex-mediated heart rate control, but will also permit us to explore the physiologic effects of various interventions in terms of their effects on the transfer functions we compute. A chronically instrumented dog can be studied over and over again, thereby making comparisons from one experiment to another more meaningful than if a different dog were used each time. For example, we plan to investigate the effects of hemorrhage on the transfer function between arterial pressure and vascular resistance, as mentioned above. The transfer function will be computed with the dog first in his baseline state, and then after various levels of hemorrhage. After the removal of each bolus of blood, GWNFM ventricular pacing will be performed at several different mean rates to allow for a more complete system characterization. These studies will then be repeated under conditions of first vagal, then β -sympathetic, and finally α -sympathetic

blockade so that we may decipher the relative contributions of each of these components in the observed response curves. Obviously, it would not be possible to conduct all of these studies on a single dog in one day, but they can easily be performed on a chronically instrumented animal over the course of several sessions. In addition, repeated experimentation on a few chronically instrumented dogs, instead of one-time usage of many acute dogs, will clearly reduce the number of animals sacrificed for this investigatory effort.

Chapter 8: Conclusion

In this thesis, I have presented an approach toward investigation of autonomic control of the cardiovascular system. The approach incorporates broad-band excitation of the system with powerful signal processing and statistical analysis techniques. In particular, robust algorithms were developed for the estimation of system transfer functions and for the determination of confidence limits of these estimates. Three different experimental preparations were described, each one calling for the development of a new strategy for the imposition of broad-band fluctuations.

An analysis of the transfer properties of the sino-atrial node was presented in Chapter 5. Broad-band input excitation here consisted of Gaussian-white-noise-frequency-modulated (GWNFM) pulse trains used to stimulate either the vagus or cardiac stellate nerve. The results presented help clarify the basic physiology that underlies sympathetic and parasympathetic influences on heart rate control. The understanding of SA nodal behavior gained here will be of great value in our efforts to interpret power spectra of spontaneous heart rate fluctuations. Furthermore, the transfer function data obtained will serve as a quantitative representation of SA nodal function in a computer model of the cardiovascular system that we are currently developing in our laboratory.

Additional work in the analysis of SA nodal behavior that we plan to pursue was outlined at the end of Chapter 5. We intend to perform follow-up studies in which independent GWNFM pulse trains will be used

to stimulate the vagus and sympathetic nerves simultaneously. This will enable us to assess whether or not the transfer functions found for single-nerve stimulation still apply when both efferent divisions of the ANS are active. The coherence functions between each of the neural rate signals and the resulting instantaneous SA nodal rate will also help to elucidate the significance of nonlinear interactions between the cardiac vagal and sympathetic neural systems. Another important aspect of neural regulation we wish to study is the extent to which normal asynchronous firing of individual neurons within the vagal or sympathetic bundles differs in its effect on the SA node from the synchronous stimulation used in our experiments. An animal preparation in which broad-band fluctuations in autonomic tone can be elicited reflexogenically, such as that described in Chapter 7, would enable us to compute transfer functions between some measure of nascent vagal or sympathetic activity and the SA nodal rate. These results could then be compared with the transfer functions found in Chapter 5.

In Chapter 6, we examined the frequency-dependent behavior of autonomic nuclei that participate in the mediation of the respiratory sinus arrhythmia (RSA). Since these studies were performed on human volunteer subjects, a noninvasive method for the introduction of broad-band system perturbations had to be devised. This was achieved by cueing subjects when to breathe with a sequence of beeps with random intervals. The results clearly demonstrated changes in the transfer function between instantaneous lung volume and heart rate associated with shifts in posture. However, our data raised as many new questions as it answered. In particular, we found consistently poor coherence between respiratory

activity and heart rate at frequencies below 0.1 Hz, and wonder if fluctuations in other hemodynamic variables, such as arterial pressure, elicit reflexogenic changes in heart rate that overwhelm the respiratory influence at these low frequencies. Furthermore, although the postural changes we employed served to shift the subject's autonomic balance, we nonetheless have yet to unravel the specific contributions of the sympathetic and vagal systems in giving rise to the observed transfer function shapes.

We are currently studying a second group of volunteer subjects in whom radial artery catheters are placed to permit measurement of arterial pressure, and pharmacologic agents are administered intravenously to allow for selective autonomic blockade. With the implementation of these features in conjunction with the random-interval breathing protocol, we intend to (1) establish the relative importance of respiratory activity versus arterial pressure fluctuations on heart rate control as a function of frequency, and (2) quantify the roles of sympathetic and parasympathetic activity in mediating the RSA. Ultimately, we plan to explore the value of the respiration-to-heart-rate transfer function as a clinical tool to assess autonomic integrity.

Finally, in Chapter 7, we presented results of a pilot study performed to demonstrate the feasibility of transfer function analysis of the baroreflex using GWNFM ventricular pacing. This pacing scheme enabled us to impose broad-band fluctuations on the instantaneous ventricular rate, and indirectly, on the arterial blood pressure. We were then able to characterize the feedforward limb of the blood pressure control system (ventricular rate to arterial pressure), as well as the

two feedback limbs (arterial pressure to SA nodal rate and to systemic vascular resistance) which are mediated by the ANS. Crucial to our analysis of SA nodal rate regulation, we blocked conduction through the atrioventricular junction to decouple atrial and ventricular activity from each other. Furthermore, our analysis of vascular resistance regulation required the development of signal processing techniques to derive an instantaneous resistance signal from the measured arterial pressure and flow traces.

Although the significance of the results obtained in the pilot study was limited by the confounding effects of anesthesia, we are excited by the prospects of performing similar experiments on conscious animals chronically instrumented using the same techniques. These studies will enable us to study with minimal invasion (after instrumentation) the effects of many important interventions on the transfer properties of both the feedforward and feedback limbs of the cardiovascular control system.

Our hope is that with the understanding of autonomic regulation afforded by the techniques presented in this thesis, we can better appreciate the subtleties of normal cardiovascular physiology and improve the vantage point from which pathologic processes are viewed. We further believe that with additional research, the concepts discussed here can lead to the development of noninvasive clinical tools that will aid in the diagnosis of cardiovascular disease in both research and primary care settings.

References

1. A.K. Ahmed, S.Y. Fakhouri, J.B. Harness, and A.J. Mearns, "Modeling of the control of heart rate by breathing using a kernel method," J. Theor. Biol., Vol. **119**, pp. 67-79 (1986).
2. H. Akaike, "A new look at the statistical model identification," IEEE Trans. Autom. Control, Vol. **AC-19**, pp. 716-723 (1974).
3. S. Akselrod, D. Gordon, J.B. Madwed, N.C. Snidman, D.C. Shannon, and R.J. Cohen, "Hemodynamic regulation: Investigation by spectral analysis," Am. J. Physiol., Vol. **249**, pp. M867-M875 (1985).
4. S. Akselrod, D. Gordon, F.A. Ubel, D.C. Shannon, A.C. Barger, and R.J. Cohen, "Power spectrum analysis of heart rate fluctuations: a quantitative probe of beat-to-beat cardiovascular control," Science, Vol. **213**, pp. 220-222 (1981).
5. J.L. Allison, K. Sagawa, and M. Kumada, "An open-loop analysis of the aortic arch barostatic reflex," Am. J. Physiol., Vol. **217**, pp. 1576-1584 (1969).
6. A. Angelone and N.A. Coulter, "Respiratory sinus arrhythmia: a frequency dependent phenomenon," J. Applied Physiol., Vol. **19**, pp. 479-482 (1964).
7. G.V. Anrep, W. Pascual, and R. Rossler, "Respiratory variations of the heart rate. II - The central mechanism of the respiratory arrhythmia and the inter-relations between the central and reflex mechanisms," Proc. Roy. Soc., Vol. **B 119**, pp. 218-232 (1936).
8. G.V. Anrep, W. Pascual, and R. Rossler, "Respiratory variations of the heart rate. I - The reflex mechanism of the respiratory arrhythmia," Proc. Roy. Soc., Vol. **B 119**, pp. 191-217 (1936).
9. F.A. Bainbridge, "The influence of venous filling upon the rate of the heart," J. Physiol., Vol. **50**, pp. 65-84 (1915).
10. F.A. Bainbridge, "The relation between respiration and the pulse-rate," J. Physiol., Vol. **54**, pp. 192-202 (1920).
11. G. Baselli, S. Cerutti, S. Civardi, D. Liberati, F. Lombardi, A. Malliani, and M. Pagani, "Spectral and cross-spectral analysis of heart rate and arterial blood pressure variability signals," Comp. Biomed. Res., Vol. **19**, pp. 520-534 (1986).
12. G. Baselli, S. Cerutti, S. Civardi, F. Lombardi, A. Malliani, M. Merri, M. Pagani, and G. Rizzo, "Heart rate variability signal processing: a quantitative approach as an aid to diagnosis in cardiovascular pathologies," Int. J. Biomed. Comp., Vol. **20**, pp. 51-70 (1987).

13. G. Baselli, S. Cerutti, S. Civardi, and G. Rizzo, "Toward a modelisation of heart rate and blood pressure interaction through parametric bivariate analysis," in Comp. in Cardiol., IEEE Computer Society Press, Silver Spring, MD (1986).
14. T. Baum, J.R. Peters, F. Butz, and D.R. Much, "A method for the placement of His bundle electrodes and production of artioventricular block in dogs," J. Applied Physiol., Vol. 38, pp. 932-933 (1975).
15. J.S. Bendat and A.G. Piersol, Engineering Applications of Correlation and Spectral Analysis, John Wiley and Sons, New York (1980).
16. R.D. Berger, S. Akselrod, D. Gordon, and R.J. Cohen, "An efficient algorithm for spectral analysis of heart rate variability," IEEE Trans. Biomed. Eng., Vol. BME-33, pp. 900-904 (1986).
17. R.D. Berger and R.J. Cohen, "Analysis of the response of the sinoatrial node to fluctuations in sympathetic and parasympathetic tone using broad band stimulation techniques," in Comp. in Cardiol., IEEE Computer Society Press, Silver Spring, MD (1986).
18. P.R. Bevington, Data Reduction and Error Analysis for the Physical Sciences, McGraw-Hill, New York, N.Y. (1969).
19. R.B. Blackman and J.W. Tukey, The Measurement of Power Spectra from the Point of View of Communications Engineering, Dover, New York, NY (1959).
20. M. Brovelli, G. Baselli, S. Cerutti, S. Guzzetti, D. Liberati, F. Lombardi, A. Malliani, M. Pagani, and P. Pizzinelli, "Computerized analysis for an experimental validation of neurophysiological models of heart rate control," in Comp. in Cardiol., IEEE Computer Society Press, Silver Spring, MD (1983).
21. D.W. Carley, The Stability of Respiratory Control in Man: Mathematical and Experimental Analyses, Ph.D. Thesis, M.I.T. (1985).
22. S. Cerutti, G. Baselli, S. Civardi, F. Lombardi, and M. Pagani, "Spectral analysis of heart rate and arterial blood pressure variability signals for physiological and clinical purposes," in Comp. in Cardiol., IEEE Computer Society Press, Silver Spring, MD (1986).
23. M.H. Chen, R.D. Berger, J.P. Saul, K. Stevenson, and R.J. Cohen, "Transfer function analysis of the autonomic response to respiratory activity during random interval breathing," in Comp. in Cardiol., IEEE Computer Society Press, Silver Spring, MD (1986).

24. G.F. Chess and F.R. Calaresu, "Frequency response model of vagal control of heart rate in the cat," Am. J. Physiol., Vol. **220**, pp. 554-557 (1971).
25. G.F. Chess, R.M.K. Tam, and F.R. Calaresu, "Influence of cardiac neural inputs on rhythmic variations of heart period in the cat," Am. J. Physiol., Vol. **228**, pp. 775-780 (1975).
26. M. Clynes, "Respiratory sinus arrhythmia: laws derived from computer simulation," J. Applied Physiol., Vol. **15**, pp. 863-874 (1960).
27. M. Clynes, "Unidirectional rate sensitivity: a biocybernetic law of reflex and humoral systems as physiologic channels of control and communication," Ann. N.Y. Acad. Sci., Vol. **92**, pp. 946-969 (1961).
28. A.J.R.M. Coenen, O. Rompelman, and R.I. Kitney, "Measurement of heart-rate variability: Part 2 - Hardware digital device for the assessment of heart-rate variability," Med. and Biol. Eng. and Comp., Vol. **15**, pp. 423-430 (1977).
29. R.J. Cohen, R.D. Berger, and T.E. Dushane, "A quantitative model of the behavior of the atrioventricular junction during atrial fibrillation," IEEE Trans. Biomed. Eng., Vol. **BME-30**, pp. 769-781 (1983).
30. J.W. Cooley and J.W. Tukey, "An algorithm for the machine calculation of complex Fourier series," Math. Computation, Vol. **19**, pp. 297-301 (1965).
31. C.T.M. Davies and J.M.M. Neilson, "Sinus arrhythmia in man at rest," J. Applied Physiol., Vol. **22**, pp. 947-955 (1967).
32. R.W. DeBoer, J.M. Karemaker, and J. Strackee, "Beat-to-beat variability of heart interval and blood pressure," Automedica, Vol. **4**, pp. 217-222 (1983).
33. R.W. DeBoer, J.M. Karemaker, and J. Strackee, "Comparing spectra of a series of point events particularly for heart rate variability data," IEEE Trans. Biomed. Eng., Vol. **BME-31**, pp. 384-387 (1984).
34. R.W. DeBoer, J.M. Karemaker, and J. Strackee, "Relationship between short-term blood-pressure fluctuations and heart-rate variability in resting subjects I: a spectral analysis approach," Med. and Biol. Eng. and Comp., Vol. **23**, (1985).
35. R.W. DeBoer, J.M. Karemaker, and J. Strackee, "Spectrum of a series of point events, generated by the integral pulse frequency modulation model," Med. and Biol. Eng. and Comp., Vol. **23**, pp. 138-142 (1985).

36. R.W. DeBoer, J.M. Karemaker, and J. Strackee, "Description of heart-rate variability data in accordance with a physiological model for the genesis of heart beats," Psychophysiology, Vol. 22, pp. 147-155 (1985).
37. G.R. DeVleeschhouwer and C. Heymans, "Baroreceptors and reflex regulation of heart rate," pp. 187-190 in Baroreceptors and Hypertension, ed. P. Kezdi, Pergamon Press, Oxford (1967).
38. J.J. DiStefano, A.R. Stubberud, and I.J. Williams, Schaum's outline series: Feedback and Control Systems, McGraw-Hill, New York (1967).
39. D.E. Donald and A.J. Edis, "Comparison of aortic and carotid baroreflexes in the dog," J. Physiol., Vol. 215, pp. 521-538 (1971).
40. J.W. Drane, L.D. Homer, and R.M. Reeves, "Mathematical description of the carotid sinus reflex," pp. 107-114 in Baroreceptors and Hypertension, ed. P. Kezdi, Pergamon Press, Oxford (1967).
41. H.W. Ead, J.H. Green, and E. Neil, "A comparison of the effects of pulsatile and non-pulsatile blood flow through the carotid sinus on the reflexogenic activity of the sinus baroreceptors in the cat," J. Physiol., Vol. 118, pp. 509-519 (1952).
42. D.L. Eckberg, "Human sinus arrhythmia as an index of vagal cardiac outflow," J. Applied Physiol., Vol. 54, pp. 961-966 (1983).
43. D.L. Eckberg, "Respiratory sinus arrhythmia: a window on central autonomic regulation in man," pp. 267-274 in The Peripheral Circulation, ed. S. Hunyor, J. Ludbrook, J. Shaw, and M. McGrath, Elsevier Science Publishers (1984).
44. D.L. Eckberg, M. Drabinsky, and E. Braunwald, "Defective cardiac parasympathetic control in patients with heart disease," New Eng. J. Med., Vol. 285, pp. 877-883 (1971).
45. D.L. Eckberg, Y.T. Kifle, and V.L. Roberts, "Phase relationship between normal human respiration and baroreflex responsiveness," J. Physiol., Vol. 304, pp. 489-502 (1980).
46. D.L. Eckberg, C. Nerhed, and B.G. Wallin, "Respiratory modulation of muscle sympathetic and vagal cardiac outflow in man," J. Physiol., Vol. 365, pp. 181-196 (1985).
47. F.M. Fouad, R.C. Tarazi, C.M. Ferrario, S. Fighaly, and C. Alicandri, "Assessment of parasympathetic control of heart rate by a noninvasive method," Am. J. Physiol., Vol. 246, pp. H838-H842 (1984).

48. G.N. Franz, "Nonlinear rate sensitivity of the carotid sinus reflex as a consequence of static and dynamic nonlinearities in baroreceptor behavior.," Ann. N.Y. Acad. Sci., Vol. **156**, pp. 811-824 (1969).
49. G.N. Franz, A.M. Scher, and C.S. Ito, "Small signal characteristics of carotid sinus baroreceptors of rabbits," J. Applied Physiol., Vol. **30**, pp. 527-535 (1971).
50. U. Freyschuss and A. Melcher, "Respiratory sinus arrhythmia in man: relation to cardiovascular pressures," Scand. J. Clin. Lab. Invest., Vol. **36**, pp. 221-229 (1976).
51. Y. Furukawa and M.N. Levy, "Temporal changes in the sympathetic-parasympathetic interactions that occur in the perfused canine atrium," Circ. Res., Vol. **55**, pp. 835-841 (1984).
52. G.Glick and E.Braunwald, "Relative roles of the sympathetic and parasympathetic nervous systems in the reflex control of heart rate," Circ. Res., Vol. **16**, pp. 363-375 (1965).
53. A.G. Goodman, L.S. Gilman, and A. Gilman, The Pharmacological Basis of Therapeutics, Macmillan Publishing Co., New York, NY (1980).
54. A.C. Guyton, T.G. Coleman, A.W. Cowley, R.D. Manning, R.A. Norman, and J.D. Ferguson, "A systems analysis approach to understanding long-range arterial blood pressure control and hypertension," Circ. Res., Vol. **35**, pp. 159-176 (1974).
55. B.T. Haymet and D.I. McCloskey, "Baroreceptor and chemoreceptor influences on heart rate during the respiratory cycle in the dog," J. Physiol., Vol. **245**, pp. 699-712 (1975).
56. J.B. Hellman and R.W. Stacy, "Variation of respiratory sinus arrhythmia with age," J. Applied Physiol., Vol. **41**, pp. 734-738 (1976).
57. J.A. Herd and A.C. Barger, "Simplified technique for chronic catheterization of blood vessels," J. Applied Physiol., Vol. **19**, pp. 791-792 (1964).
58. C. Heymans and E. Neil, Reflexogenic Areas of the Cardiovascular System, Little, Brown and Co., Boston (1958).
59. J.A. Hirsch and B. Bishop, "Respiratory sinus arrhythmia in humans: how breathing pattern modulates heart rate," Am. J. Physiol., Vol. **241**, pp. H620-H629 (1981).
60. R. Hosomi, "Unstable state of the arterial pressure control system after mild hemorrhage," Am. J. Physiol., Vol. **235**, pp. R279-R285 (1978).

61. W.J.M. Hrushesky, D. Fader, O. Schmitt, and V. Gilbertsen, "The respiratory sinus arrhythmia: a measure of cardiac age," Science, Vol. 224, pp. 1001-1004 (1984).
62. B.W. Hyndman and J.R. Gregory, "Spectral analysis of sinus arrhythmia during mental loading," Ergonomics, Vol. 18, pp. 255-270 (1975).
63. B.W. Hyndman, R.I. Kitney, and B.M. Sayers, "Spontaneous rhythms in physiological control systems," Nature, Vol. 233, pp. 339-341 (1971).
64. B.W. Hyndman and R.K. Mohn, "A pulse modulator model for pacemaker activity," Digest 10th Intern. Conf. Med. Biol. Eng., p. 223 (1973).
65. C.S. Ito, "Nonlinear effects of carotid sinus pressure changes on peripheral resistance," Ann. N.Y. Acad. Sci., Vol. 156, pp. 796-810 (1969).
66. C.S. Ito and A.M. Scher, "Regulation of arterial blood pressure by aortic baroreceptors in the unanesthetized dog," Circ. Res., Vol. 42, pp. 230-236 (1978).
67. J.E. Angell James and M.DeB. Daly, "Comparison of the reflex vasomotor responses to separate and combined stimulation of the carotid sinus and aortic arch baroreceptors by pulsatile and nonpulsatile pressures in the dog," J. Physiol., Vol. 209, pp. 257-293 (1970).
68. T.N. James, "The sinus node as a servomechanism," Circ. Res., Vol. 32, pp. 307-313 (1973).
69. T.N. James, E.S. Bear, R.J. Frink, K.S. Lang, and J.C. Tomlinson, "Selective stimulation, suppression, or blockade of the atrioventricular node and His bundle," J. Lab. Clin. Med., Vol. 76, pp. 240-256 (1970).
70. G.M. Jenkins and D.G. Watts, Spectral Analysis and its Applications, Holden-Day, Oakland, CA (1968).
71. S. Jennett and J.H. McKillop, "Observations on the incidence and mechanism of sinus arrhythmia in man at rest," J. Physiol., Vol. 213, pp. 58P-59P (1971).
72. N. Joels and M. Samueloff, "The activity of the medullary centres in diffusion respiration," J. Physiol., Vol. 133, pp. 360-372 (1956).
73. S. Kalli, R. Suoranta, and M. Jokipii, "Applying a multivariate autoregressive model to describe interactions between blood pressure and heart rate," 3rd Int. Conf. on Measurement in Clin. Med., (1986).

74. S. Kalli, R. Suoranta, M. Jokipii, and V. Turjanmaa, "Analysis of blood pressure and heart rate variability using multivariate autoregressive modelling," in Comp. in Cardiol., IEEE Computer Society Press, Silver Spring, MD (1986).
75. P.G. Katona and G.O. Barnett, "Central origin of asymmetry in the carotid sinus reflex," Ann. N.Y. Acad. Sci., Vol. **165**, pp. 779-786 (1969).
76. P.G. Katona, G.O. Barnett, and W.D. Jackson, "Computer simulation of the blood pressure control of the heart period," pp. 191-199 in Baroreceptors and Hypertension, ed. P. Kezdi, Pergamon Press, Oxford (1967).
77. P.G. Katona and F. Jih, "Respiratory sinus arrhythmia: noninvasive measure of parasympathetic cardiac control," J. Applied Physiol., Vol. **39**, pp. 801-805 (1975).
78. P.G. Katona, J.W. Poitras, G.O. Barnett, and B.S. Terry, "Cardiac vagal efferent activity and heart period in the carotid sinus reflex," Am. J. Physiol., Vol. **218**, pp. 1030-1037 (1970).
79. S.M. Kay and S.L. Marple, "Spectrum analysis - a modern perspective," Proc. IEEE, Vol. **69**, pp. 1380-1419 (1981).
80. R.O. Kenet, Closed-loop identification of hemodynamic control, Ph.D. Thesis, Yale University (1983).
81. R.O. Kenet, F.B. Tuteur, and R.J. Cohen, "Closed-loop identification of hemodynamic control systems," in Comp. in Cardiol., IEEE Computer Society Press, Silver Spring, MD (1982).
82. N.Z. Kerin, G. Louridas, J. Edelstein, and M.N. Levy, "Interactions among the critical factors affecting sinus node function: the quantitative effects of the duration and frequency of atrial pacing and of vagal and sympathetic stimulation upon overdrive suppression of the sinus node," Am. J. Physiol., Vol. **105**, pp. 215-223 (1983).
83. R.I. Kitney, "Magnitude and phase changes in heart rate variability and blood pressure during respiratory entrainment," J. Physiol., Vol. **270**, pp. 40P-41P (1977).
84. R.I. Kitney, T. Fulton, A.H. McDonald, and D.A. Linkens, "Transient interactions between blood pressure, respiration and heart rate in man," J. Biomed. Eng., Vol. **7**, pp. 217-224 (1985).
85. R.I. Kitney and O. Rompelman, The Study of Heart-rate Variability, Oxford Univ. Press, New York (1980).
86. C.F. Knapp, J.M. Evans, D.C. Randall, and J.A. Marquis, "Cardiovascular regulation in canines during low-frequency acceleration," Am. J. Physiol., Vol. **243**, pp. H998-H1009 (1982).

87. Y.W. Lee and M. Schetzen, "Measurement of the Wiener kernels of a non-linear system by cross-correlation," Int. J. Control, Vol. 2, pp. 237-254 (1965).
88. N. Levinson, "The Wiener (root mean square) error criterion in filter design and prediction," J. Math. Phys., Vol. 25, pp. 261-278 (1947).
89. W.H. Levison, G.O. Barnett, and W.D. Jackson, "Nonlinear analysis of the baroreceptor reflex system," Circ. Res., Vol. 18, pp. 673-682 (1966).
90. M.N. Levy, "Sympathetic-parasympathetic interactions in the heart," Circ. Res., Vol. 29, pp. 437-445 (1971).
91. M.N. Levy, H. DeGeest, and H. Zieske, "Effects of respiratory center activity on the heart," Circ. Res., Vol. 18, pp. 67-78 (1966).
92. M.N. Levy and H. Zieske, "Autonomic control of cardiac pacemaker activity and atrioventricular transmission," J. Applied Physiol., Vol. 27, pp. 465-470 (1969).
93. T.C. Lloyd, "Cardiopulmonary baroreflexes: integrated responses to sine- and square-wave forcing," J. Applied Physiol., Vol. 35, pp. 870-874 (1973).
94. H. Luczak and W. Laurig, "An analysis of heart rate variability," Ergonomics, Vol. 16, pp. 85-97 (1973).
95. J.B. Madwed, Dynamic Analysis of Arterial Blood Pressure and Heart Rate During Baseline Conditions and Hemorrhage in the Conscious Dog, Ph.D. Thesis, Harvard Univ. (1986).
96. P.Z. Marmarelis and K.I. Naka, "Nonlinear analysis and synthesis of receptive-field responses in the catfish retina. I. Horizontal cell to ganglion cell chain," J. Neurophysiol., Vol. 36, pp. 605-618 (1973).
97. S. Mayer, "Studien zur Physiologie des Herzens und der Blutgefasse: 5. Abhandlung: Uber spontane Blutdruckschwankungen," Sber. Akad. Wiss. Wien, 3. Abt., Vol. 74, pp. 281-307 (1876).
98. A. Melcher, "Respiratory sinus arrhythmia in man. A study in heart rate regulating mechanisms," Acta. Physiol. Scand. Supp., Vol. 435, pp. 1-31 (1976).
99. A. Melcher, "Carotid baroreflex heart rate control during the active and the assisted breathing cycle in man," Acta Physiol. Scand., Vol. 108, pp. 165-171 (1980).

100. V.B. Mountcastle, Medical Physiology, C.V. Mosby Co., St. Louis (14th edition, 1980).
101. G.A. Myers, G.J. Martin, N.M. Magid, P.S. Barnett, J.W. Schaad, J.S. Weiss, M. Lesch, and D.H. Singer, "Power spectral analysis of heart rate variability in sudden cardiac death: comparison to other methods," IEEE Trans. Biomed. Eng., Vol. **BME-33**, pp. 1149-1156 (1986).
102. A.V. Oppenheim and R.W. Schaffer, Digital Signal Processing, Prentice-Hall, Englewood Cliffs (1975).
103. M. Pagani, F. Lombardi, S. Guzzetti, O. Rimoldi, R. Furlan, P. Pizzinelli, G. Sandrone, G. Malfatto, S. Dell'Orto, E. Piccaluga, M. Turiel, G. Baselli, S. Cerutti, and A. Malliani, "Power spectral analysis of heart rate and arterial pressure variabilities as a marker of sympatho-vagal interaction in man and conscious dog," Circ. Res., Vol. **59**, pp. 178-193 (1986).
104. E. Parzen, "Some recent advances in time series modeling," IEEE Trans. Automat. Control, Vol. **AC-19**, pp. 723-730 (1974).
105. J. Penaz, "Frequency response of the cardiac chronotropic action of the vagus in the rabbit," Arch. Int. Physiol. Bioch., Vol. **70**, pp. 636-650 (1962).
106. J. Penaz, "Mayer waves: history and methodology," Automedica, Vol. **2**, pp. 135-141 (1978).
107. J. Penaz, N. Honzikova, and B. Fizer, "Spectral analysis of resting variability of some circulatory parameters in man," Physiol. Bohem., Vol. **27**, pp. 349-357 (1978).
108. B. Pomeranz, R.J.B. MacCaulay, M.A. Caudill, I. Kutz, D. Adam, D. Gordon, K.M. Kilborn, A.C. Barger, D.C. Shannon, R.J. Cohen, and H. Benson, "Assessment of autonomic function in humans by heart rate spectral analysis," Am. J. Physiol., Vol. **248**, pp. H151-H153 (1985).
109. G. Preiss and C. Polosa, "Patterns of sympathetic neuron activity associated with Mayer waves," Am. J. Physiol., Vol. **226**, pp. 724-730 (1974).
110. W.H. Press, B.P. Flannery, S.A. Teukolsky, and W.T. Vetterling, Numerical Recipes: The Art of Scientific Computing, Cambridge Univ. Press, New York (1986).
111. I.A. Reid, "The renin-angiotensin system and body function," Arch. Intern. Med., Vol. **145**, pp. 1475-1479 (1985).

112. J.A. Ringo, K.B. Campbell, N.S. Peterson, and R.A. Baker, "Frequency modulation of heart rate to increase low-frequency content of cardiovascular signals," IEEE Trans. Biomed. Eng., Vol. **BME-29**, pp. 537-541 (1982).
113. O. Rompelman, A.J.R.M. Coenen, and R.I. Kitney, "Measurement of heart-rate variability: Part 1 - Comparative study of heart-rate variability analysis methods," Med. and Biol. Eng. and Comp., Vol. **15**, pp. 233-239 (1977).
114. O. Rompelman, W.H.A. van Kampen, and E. Backer, "Heart rate variability in relation to psychological factors," Ergonomics, Vol. **23**, pp. 1101-1115 (1980).
115. O. Rompelman, J.B.I.M. Snijders, and C.J. Van Spronsen, "The measurement of heart rate variability spectra with the help of a personal computer," IEEE Trans. Biomed. Eng., Vol. **BME-29**, pp. 503-510 (1982).
116. M. Rosenbaum and D. Race, "Frequency-response characteristics of vascular resistance vessels," Am. J. Physiol., Vol. **215**, pp. 1397-1402 (1968).
117. A. Rosenblueth and F.A. Simeone, "The interrelations of vagal and accelerator effects on the cardiac rate," Am. J. Physiol., Vol. **110**, pp. 42-55 (1934).
118. K. Sagawa, "Relative roles of the rate sensitive and proportional control elements of the carotid sinus during mild hemorrhage," pp. 97-105 in Baroreceptors and Hypertension, ed. P. Kezdi, Pergamon Press, Oxford (1967).
119. A. Samaan, "Antagonistic cardiac nerves and heart rate," J. Physiol., Vol. **83**, pp. 332-340 (1935).
120. B.M. Sayers, "Analysis of heart rate variability," Ergonomics, Vol. **16**, pp. 17-32 (1973).
121. A.M. Scher, "Carotid and aortic regulation of arterial blood pressure," Circulation, Vol. **56**, pp. 521-528 (1977).
122. A.M. Scher, W.W. Ohm, K. Bumgarner, R. Boynton, and A.C. Young, "Sympathetic and parasympathetic control of heart rate in the dog, baboon and man," Fed. Proc., Vol. **31**, pp. 1219-1225 (1972).
123. A.M. Scher and A.C. Young, "Servoanalysis of carotid sinus reflex effects on peripheral resistance," Circ. Res., Vol. **12**, pp. 152-162 (1963).
124. A.M. Scher and A.C. Young, "Nonlinearity in the control of blood pressure and heart rate," Ann. N.Y. Acad. Sci., Vol. **16**, pp. 722-730 (1969).

125. A.M. Scher and A.C. Young, "Reflex control of heart rate in the unanesthetized dog," Am. J. Physiol., Vol. 218, pp. 780-789 (1970).
126. R.M. Schmidt, M. Kumada, and K. Sagawa, "Cardiovascular response to various pulsatile pressures in the carotid sinus," Am. J. Physiol., Vol. 223, pp. 1-7 (1972).
127. A. Selman, A. McDonald, R. Kitney, and D. Linkens, "The interaction between heart rate and respiration: Part I - Experimental studies in man," Automedica, Vol. 4, pp. 131-139 (1982).
128. A. Selman, A. McDonald, R. Kitney, and D. Linkens, "The interaction between heart rate and respiration: Part II - Nonlinear analysis based on computer modelling," Automedica, Vol. 4, pp. 141-153 (1982).
129. J.W. Spickler, P. Kezdi, and E. Geller, "Transfer characteristics of the carotid sinus pressure control system," pp. 31-40 in Baroreceptors and Hypertension, ed. P. Kezdi, Pergamon Press, Oxford (1967).
130. L. Stark, "The pupillary control system: its nonlinear adaptive and stochastic engineering design characteristics," Automedica, Vol. 5, pp. 655-676 (1969).
131. J. Stegemann and U. Tibes, "Sinusoidal stimulation of carotid sinus baroreceptors and peripheral blood pressure in dogs," Ann. N.Y. Acad. Sci., Vol. 16, pp. 787-795 (1969).
132. C. Steiner and T.W. Kovalik, "A simple technique for production of chronic complete heart block in dogs," J. Applied Physiol., Vol. 25, pp. 631-632 (1968).
133. M.G. Taylor, "Use of random excitation and spectral analysis in the study of frequency-dependent parameters of the cardiovascular system," Circ. Res., Vol. 18, pp. 585-595 (1966).
134. L. Traube, "Ueber periodische Thatigkeits-Aeusserungen des vasomotorischen und Hemmungs-Nervencentrums," Zbl. Med. Wiss., Vol. 56, pp. 881-885 (1865).
135. V. Volterra, Theory of Functionals and of Integral and Integro-Differential Equations, Dover, New York, NY (1930).
136. H.R. Warner and A. Cox, "A mathematical model of heart rate control by sympathetic and vagus efferent information," J. Applied Physiol., Vol. 17, pp. 349-355 (1962).
137. H.R. Warner and R.O. Russell, "Effects of combined sympathetic and vagal stimulation on heart rate in the dog," Circ. Res., Vol. 24, pp. 567-573 (1969).

138. W.R. Webb and S.E. Field, "Effect of anesthetization of AV node on ventricular fibrillation following acute coronary arterial occlusion," Am. J. Physiol., Vol. **195**, pp. 403-406 (1958).
139. N. Wiener, "Generalized harmonic analysis," Acta Mathematica, Vol. **55**, pp. 117-258 (1930).
140. N. Wiener, Nonlinear Problems in Random Theory, John Wiley and Sons, New York (1958).
141. B.F. Womack, "The analysis of respiratory sinus arrhythmia using spectral analysis and digital filtering," IEEE Trans. Biomed. Eng., Vol. **BME-18**, pp. 399-409 (1971).
142. U. Zwiener, "Physiological interpretation of autospectra, coherence and phase spectra of blood pressure, heart rate, and respiration waves in man," Automedica, Vol. **2**, pp. 161-169 (1978).

Biographical Sketch

Ronald David Berger was born on June 4, 1958 in White Plains, N.Y. Throughout his first three years as an undergraduate at M.I.T., he fully anticipated a career in semiconductor physics as an electrical engineer. Despite (not because of) his mother's suggestion that he consider a career in medicine, however, Ron found himself becoming progressively less enamored with silicon and more interested in cytoplasm, as he began his senior year.

In January, 1980, Ron began working in Richard Cohen's lab as a UROP student. His association with Prof. Cohen has continued through seven years as a graduate student in the M.I.T. Department of Electrical Engineering and as a medical student in the Harvard-M.I.T. Division of Health Sciences and Technology. Ron found that the field of biomedical engineering offered the opportunity to combine his early interest in electronics with his more recent fascination with biological systems. In fact, he will continue to straddle the academic fence between medicine and research for at least four more years. In June, 1987, Ron will begin an internship at the Brigham and Women's Hospital as the first leg of a Research Residency program in medicine. During the research segments of this program, Ron plans to further investigate cardiovascular regulation using the approach developed in his Ph.D. thesis work.

Ron met his wife, Linda Brafman, in his second year of medical school. They were married in October, 1984, and currently live in Brookline, Massachusetts.